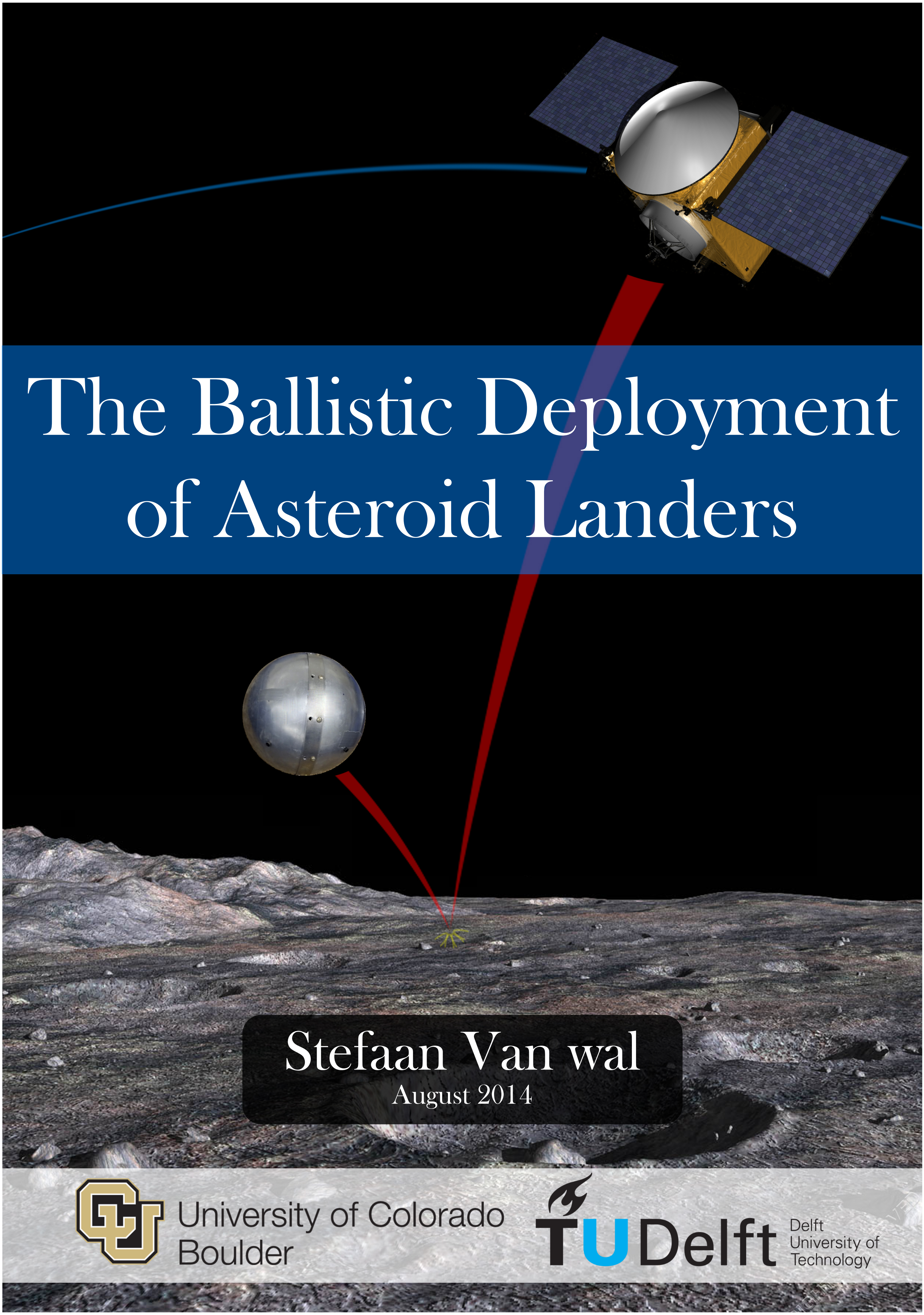

The Ballistic Deployment of Asteroid Landers

Stefaan Van wal

August 2014

University of Colorado Boulder

TU Delft Delft University of Technology

M.Sc. Thesis

THE BALLISTIC DEPLOYMENT OF ASTEROID LANDERS

by

Stefaan VAN WAL

Faculty of Aerospace Engineering
Delft University of Technology

Supervisors:
Dr. Ir. Dan Scheeres
Dr. Ir. Erwin Mooij

August 2014
Revised October 2014

University of Colorado Boulder

TU Delft

Delft University of Technology

Acknowledgements

Perhaps the most difficult part of writing this master's thesis is figuring out a way to properly thank everyone that has supported me during these eight months of hard work. First and foremost, I want to thank my two advisors Dan Scheeres and Erwin Mooij. Dan, thank you for the continued opportunity of having me work in the CSML lab. Erwin, thank you for your enthusiasm in suddenly being thrown on my project, and for working our Skype meetings into your schedule. Furthermore, I am extremely grateful to my mentor, colleague, and friend, Simon Tardivel, for his patience, advice, and friendship: merci beaucoup.

This thesis is the capstone of a much larger and longer project: my studies in aerospace engineering at the TU. I would not have made it through all those years if it hadn't been for all my friends in Delft. Our bowling nights, spotting trips, CFC dinners, and endless group assignments are some of my best memories from that time (perhaps not so much that last one) - may we have many more!

Of course, there is more to life than just studying, and I would not have achieved what I have achieved without my weekend getaways with the CU Hiking Club. The countless trips I took into the wilderness of the Rocky Mountains with you awesome people were the most ideal way possible of de-stressing after a week of frustrating debugging sessions. *Half mile more!*

Finally, and most importantly, I want to thank my friends and family at home. It's not easy to see your friend or son take off to the other side of the world, and I would never have been able to do this dream-chasing without your endless love and support. Thanks for everything.

Stefaan Van wal

Please consider the environment before printing this document.

I took the road less travelled by
and that has made all the difference.

- Robert Frost

Glossary

AIDA	Asteroid Impact & Deflection Assessment
AIM	Asteroid Impact Monitoring
BASiX	Binary Asteroid in-situ Explorer
CR3BP	Circular Restricted Three-Body Problem
DART	Double Asteroid Redirection Test
DCM	Direction Cosine Matrix
ESA	European Space Agency
GNC	Guidance, Navigation and Control
JAXA	Japan Aerospace Exploration Agency
MBO	Main-Belt Object
NEO	Near-Earth Object
RB1F	Rotating Body-1 Frame
RB2F	Rotating Body-2 Frame
RK	Runge-Kutta
SCF	Spacecraft-Centered Frame
SIF	Solar Inertial Frame
SOI	Sphere of Influence
TAG	Touch-and-Go
TIF	Target Inertial Frame
TNO	Trans-Neptunian Object
NASA	National Aeronautics and Space Administration
V&V	Verification and Validation

List of Symbols

Roman Symbols

Symbol	Unit	Definition
$\mathbf{a}$	m/s^2	Acceleration
$\mathbf{B}$	-	Quaternion matrix
C_{rr}	-	Coefficient of rolling resistance
$\mathbf{C}$	-	Direction cosine matrix
d	m	Distance
$\mathcal{E}$	-	Edge
$\mathbf{E}$	-	Edge dyad
E	J/kg	Specific energy
e	-	Coefficient of restitution
e	m	Edge length
$\hat{\mathbf{e}}$	-	Edge unit vector
e	varies	Truncation error
$\mathcal{F}$	-	Facet
$\mathbf{F}$	-	Facet dyad
$\mathbf{F}$	N	Force
f	-	Coefficient of friction
G	Nm^2/kg^2	Universal gravitational constant
g	m/s^2	Gravitational acceleration
$\mathbf{H}$	m	Contact point
h	s	Step size
$\mathbf{I}_n$	-	Identity matrix (size n x n)
I	m^{2}kg	Inertia
$\hat{I}$	m^2	Normalized inertia
$\mathbf{J}$	varies	Impulse
$\mathbf{k}$	-	Increment function factor
L	-	Lagrange point
L	-	Per-edge factor

Symbol	**Unit**	**Definition**
$\mathbf{L}$	Nm	Torque
m	kg	Mass
$\mathbf{N}$	-	Normal vector
n	-	Number of features
$\mathbf{O}$	-	Reference system origin
$\mathbf{P}$	m	Field point
P	s	Period
$\mathbf{P}$	-	Vertex
q	-	Quaternion
R_v	m	Mean volumetric radius
$\mathbf{R}$	m	Position vector
r	m	Radius
r	m	Length of vector
$\mathbf{r}$	m	Vector to a vertex
t	s	Time
U	J/kg	Gravitational potential
∇U	$\mathrm{m/s^2}$	Gravitational attraction
$\nabla\nabla U$	$\mathrm{s^{-2}}$	Gravity gradient
$\nabla^2 U$	-	Gravity field Laplacian
$\mathbf{u}_r$	-	Center-contact point unit vector
$\mathbf{V}$ or $\mathbf{v}$	m/s	Velocity
$\mathcal{V}$	-	Vertex
V	$\mathrm{m^3}$	Volume
X or x	m	Cartesian X-coordinate
$\mathbf{X}$	varies	State vector
Y or y	m	Cartesian Y-coordinate
Z or z	m	Cartesian Z-coordinate

Greek Symbols

Symbol	Unit	Definition
Δ	varies	Difference
ϵ	varies	Maximum acceptable error
η	varies	State estimate
$\dot{\theta}$	rad/s	Angular velocity
λ	rad	Latitude
μ	m^3/s^2	Gravitational parameter
μ	varies	Mean
ρ	kg/m^3	Density
σ	varies	Standard deviation
ϕ	-	Increment function
ϕ	rad	Longitude
Ω	J/kg	Amended potential
ω	-	Per-facet factor
$\boldsymbol{\omega}$	rad/s	Rotation rate

Sub- and Superscripts

Symbol	Definition
B1	Primary body
B2	Secondary body
$\mathcal{E}$	Edge
e	External
$\mathcal{F}$	Facet
f	Coulomb friction
H	Contact point
i/j/k/l	Feature identifier
j	Inertia modifier
k	Intersection point
kin	Kinetic
m	Midpoint
max	Maximum
min	Minimum
N	Normal force
n	Impact identifier
nom	Nominal
pos	Position

Symbol	**Definition**
pot	Potential
rel	Release
rr	Rolling Resistance
rot	Rotation
S/C	Spacecraft
T	Target asteroid system
T	Transpose
$\mathcal{V}$	Vertex
vel	Velocity
x/y/z	Cartesian components
x/z	Atlas identifier
0	Reference state
0/1	Before/after impact
1/2/3/4	Quaternion elements
α	Primary body
β	Secondary body
$\parallel$	Parallel
$\perp$	Perpendicular
∞	Virtual bounce

Contents

Acknowledgements **vii**

Glossary **vii**

List of Symbols **xii**

1 Introduction **1**

I Heritage 5

2 Missions to Small Bodies **7**
- 2.1 Past and Current Missions . . . 7
  - 2.1.1 NEAR-Shoemaker . . . 7
  - 2.1.2 Hayabusa . . . 8
  - 2.1.3 Rosetta . . . 9
- 2.2 Future Missions . . . 10
  - 2.2.1 Hayabusa-2 . . . 10
  - 2.2.2 OSIRIS-REx . . . 11
  - 2.2.3 AIDA . . . 11
  - 2.2.4 BASiX . . . 12

3 Thesis Goals **15**

II Methods and Software 17

4 Modelling **19**
- 4.1 Reference Frames . . . 19
  - 4.1.1 Unitary Sytems . . . 19
  - 4.1.2 Binary Systems . . . 21
- 4.2 State Variables . . . 22

4.3 Asteroid Shape and Gravity 23
4.4 Contact Motion 28
  4.4.1 Normal Force 29
  4.4.2 Coulomb Friction 30
  4.4.3 Rolling Resistance 31
  4.4.4 Regularization 33
4.5 Collisions 34
4.6 Rock Interaction 35
4.7 Equations of Motion 37
  4.7.1 Unitary Systems 37
  4.7.2 Binary System 39

5 Geometry **43**
5.1 Normal Construction 43
5.2 Distance Computations 46
  5.2.1 Distance to a Facet 46
  5.2.2 Distance to an Edge 46
  5.2.3 Distance to a Vertex 47
5.3 Atlas 48

6 Propagator **53**
6.1 Integrator 53
  6.1.1 Time-Step Variability 54
  6.1.2 Constraint Application 56
6.2 Event Capability 57
6.3 Algorithm Structure 59

III Verification and Validation **63**

7 Gravity **65**
7.1 Polyhedron Model 65
7.2 Linearization 66
7.3 Model Resolution 69
7.4 Propagation Mode 74

8 Contact Motion **79**
8.1 World Set-Up 79
8.2 Collisions 80
  8.2.1 Analytical Results 80
  8.2.2 Numerical Simulations 83

8.3 Rolling 87
8.3.1 Analytical Results 87
8.3.2 Numerical Simulations 89
8.3.3 Extended Flat-World Motion 91
8.4 Motion on Relief Worlds 93
8.4.1 Table World 93
8.4.2 Gutter World 103
8.4.3 Pit World 104
8.4.4 Spike World 105

IV Simulation and Results **109**

9 Unitary Systems **111**
9.1 Mission Scenario 111
9.2 Results for Nominal Deployment 115
9.3 Effect of Rocks 117
9.4 Effect of Interaction Coefficients 121
9.5 Effect of Deployment Parameters 122

10 Binary Systems **131**
10.1 Mission Scenario 131
10.2 Deployment to Beta 134
10.2.1 Deployment from L_1 134
10.2.2 Deployment from L_2 136
10.3 Deployment to Alpha 138

V Conclusions and Recommendations **141**

11 Conclusions **143**

12 Recommendations for Future Work **147**

Bibliography **149**

Chapter 1

Introduction

Near the end of the eighteenth century, the Italian astronomer Giuseppe Piazzi was searching the night skies midway the orbits of Mars and Jupiter, the location where the Titius-Bode law of planetary distances had predicted a planet would exist. On January 1, 1801, he had a stroke of luck and indeed observed an object in this region. Piazzi named the object *Ceres*, after the Roman goddess of agriculture, but was surprised by its small diameter of roughly 1,000 km; considerably smaller than the other planets known at the time. Ceres was therefore classified as the first *minor planet* and in the following years three similar-sized objects were discovered in the same region of our Solar System, and given the names *Pallas, Juno* and *Vesta*. These four bodies would remain the only known minor planets during the first half of the nineteenth century, until a large number of discoveries of much smaller objects in similar orbits was made and astronomers realized an entire 'belt' of such objects existed [1].

It was at this point that the German astronomer William Herschel, famous for his discovery of the planet Neptune, proposed naming these objects *asteroids* after the Greek word *άστεροειδής* ("*asteroides*"), meaning *star-like*, instead of using the term *minor planet*. The number of asteroid discoveries has sky-rocketed ever since with most observations nowadays being carried out by automated systems, a process which has resulted in over 200,000 categorized asteroids with large observed variations in composition, mass, and size, as shown in Figure 1.1. These bodies are classified in a number of different categories depending on their respective locations in the Solar system. The large number of asteroids contained in the previously mentioned belt between the orbits of Mars and Jupiter are known as Main-Belt Objects (MBOs). Many more inhabit zones beyond the orbit of Neptune and are hence named Trans-Neptunian Objects (TNOs). Two classes with far fewer members are the Trojans, located at Jupiter's L_4 and L_5 Lagrange points and the Centaurs, which populate the area between the orbits of Jupiter and Neptune. A fifth and final class constitutes the Near-Earth Objects (NEOs), which closely approach the orbit of the Earth and represent interesting targets for space missions due to their relative ease of accessibility [2]. The asteroid distribution of the inner Solar system is shown in Figure 1.2.

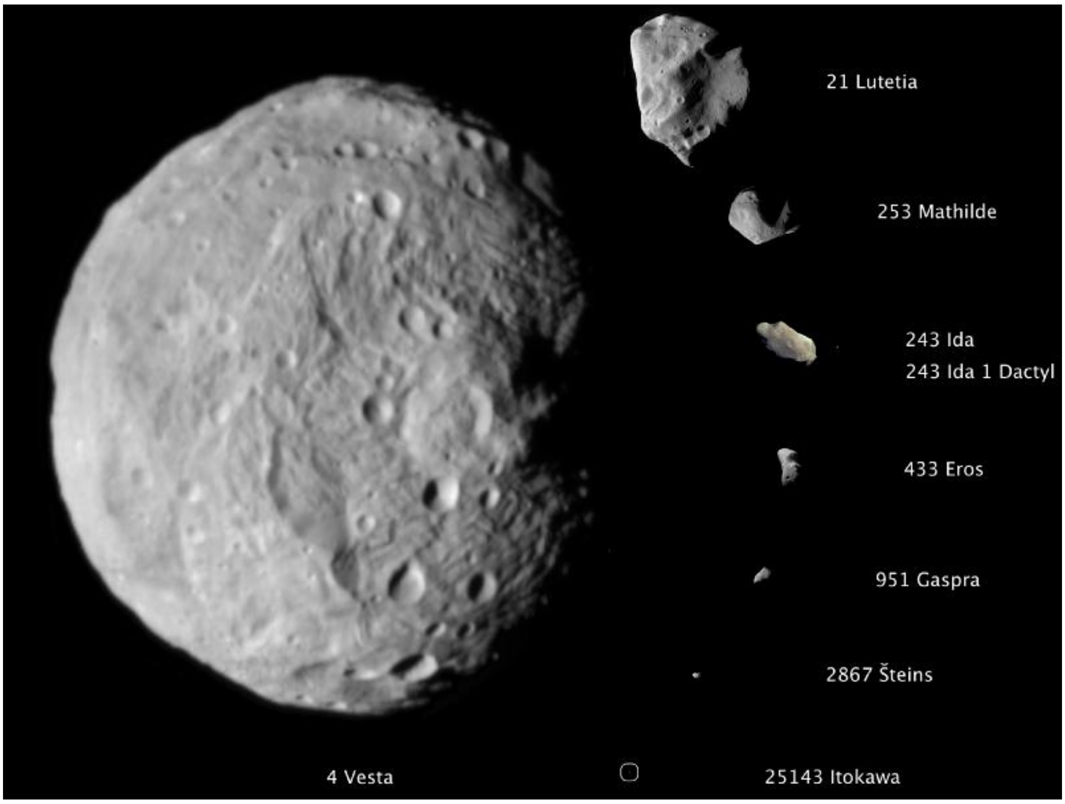

Figure 1.1: Relative sizes of asteroids imaged at high resolution [3].

These asteroids have become a core interest of the scientific and aerospace community ever since the *NEAR-Shoemaker* mission, which explored asteroid 433 Eros in 2001 [4]. This interest was furthered by the *Hayabusa* sample return mission that rendezvoused with asteroid 25143 Itokawa and returned small regolith samples to Earth in 2010 [5]. The results from these missions have fundamentally changed our understanding of the origins and characteristics of asteroid bodies. Despite these insights, many scientific questions still exist regarding the strength, cohesion and seismic properties of asteroids, which can only be answered through extensive analyses of asteroid (sub-)surfaces. Such analyses would revolutionize our understanding of aggregate interaction in micro-gravity environments and the formation of the early Solar system [6]. The acquisition of this information has been identified by NASA as Key Strategic Knowledge Gaps and is regarded as crucial to all future exploration of asteroid bodies [7]. Furthermore, measurements of these characteristics are paramount to the development of planetary defense strategies, which are required to guarantee the long-term survival of human civilization [8]. Finally, asteroidal bodies contain vast supplies of rare metals and water, and therefore represent possible sources of revenue and in-space refuelling options [7]. Although NASA's *OSIRIS-REx* [9] and JAXA's *Hayabusa-2* [10] spacecraft are set to continue exploring asteroids, both of these are 'mere' sample return missions that do not perform the previously mentioned (sub-)surface measurements. This is why scientists at the Jet Propulsion Laboratory, the California Institute of Technology and the University of Colorado at Boulder are proposing the *Binary Asteroid in-situ Explorer* (BASiX) mission. This mission aims to investigate the binary asteroid system 1996 FG$_3$ using an orbiter spacecraft which deploys several instrumentation packages to the asteroid surfaces. These packages are designed as passive spherical pods that, among other hardware, contain explosive charges which will allow for an evaluation of the seismic properties of the asteroid bodies [6].

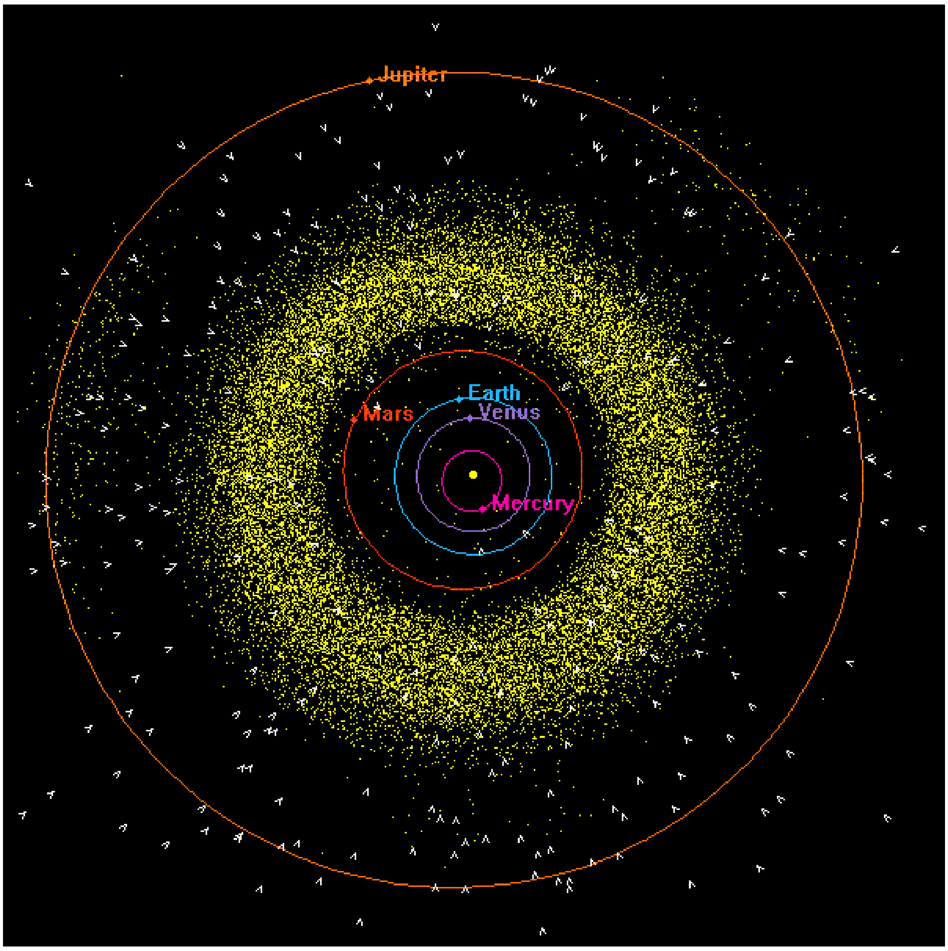

Figure 1.2: Position of all numbered asteroids in the inner Solar system on January 1, 2014 [11].

Previous studies regarding the ballistic deployment of such passive lander pods to a binary asteroid system have established release strategies and identified factors relevant to the motion of the pods [12–16]. These studies have taken into account both the orbital motion of lander/rover packages and the contact interactions with the asteroid surface. They have shown that the characteristics of deployment are significantly affected by a number of interaction parameters, as well as the navigation and control accuracies of the mothership. Our research aims to verify these strategies and quantify the degree to which the aforementioned parameters influence deployment. This is done through the development of a simulator package capable of accurately simulating the complex interactions between a lander pod and the complex gravitational and surface environments present at both unitary and binary asteroid systems. By selecting a realistic set of spacecraft and deployment parameters with associated uncertainties, we will be able to simulate a high number of lander pod trajectories and analyze their settling characteristics. This in turn will generate information about the sensitivity of successful lander deployment to the release conditions and interaction parameters. The final results of our work will aid mission designers in the planning of an asteroid lander mission and will provide an answer to the research question "*can we investigate the surface, sub-surface, and internal environment of asteroids?*".

This thesis report is structured as follows: in Chapter 2 we briefly review past, present and future missions to asteroids that are relevant to our research. This allows us to establish the goals of the thesis in Chapter 3. Next, Chapter 4 presents the techniques used to model asteroid environments, with Chapter 5 discussing some of the geometry involved in the shape modelling of asteroids. Chapter 6 provides an overview of the propagation technique used and the general structure of our simulation algorithms. Significant attention is given to the verification and validation of the applied gravity modelling in Chapter 7, and of contact interactions in Chapter 8. The results produced with the finished simulation software are given in Chapter 9 for unitary asteroid systems and in Chapter 10 for binary systems. Finally, Chapter 11 presents the conclusions of our research and Chapter 12 discusses some recommendations for future work.

Part I

Heritage

Chapter 2

Missions to Small Bodies

THE PAST DECADES have seen a number of different missions to asteroids and comets that have resulted in our current understanding of the properties of these small bodies. In addition, several agencies across the globe are planning future missions aimed at studying such bodies in much further detail. The current chapter presents a brief overview of the characteristics of past and current missions in Section 2.1 and of future missions in Section 2.2. The resulting state-of-the-art will help justify the goals of the current research in the subsequent chapter.

2.1 Past and Current Missions

We now present a brief overview of missions that have flown in the past or are active at the time of writing.

2.1.1 NEAR-Shoemaker

The *NEAR-Shoemaker* spacecraft, launched by NASA in 1996, was the first to perform an extended proximity study of an asteroid. The spacecraft spent a full year orbiting asteroid 433 Eros, while collecting information on the body's mass, structure, geology, composition, and gravity using a wide range of scientific instruments [17]. The main result of the mission was a high-resolution shape model of Eros along with a global mapping of the surface rock and crater distribution. The 15-kilometer-wide asteroid was determined to have a nearly-homogeneous mass of $(6.690 \pm 0.003) \times 10^{15}$ kg and a bulk density of 2.67 ± 0.03 g/cm^3 [18]. After completing all of its science goals, the spacecraft successfully descended and touched down on the surface of Eros in a controlled manner [4]. High-resolution images captured during final descent provided detailed information about local topography and formation processes, see Figure 2.1 [19].

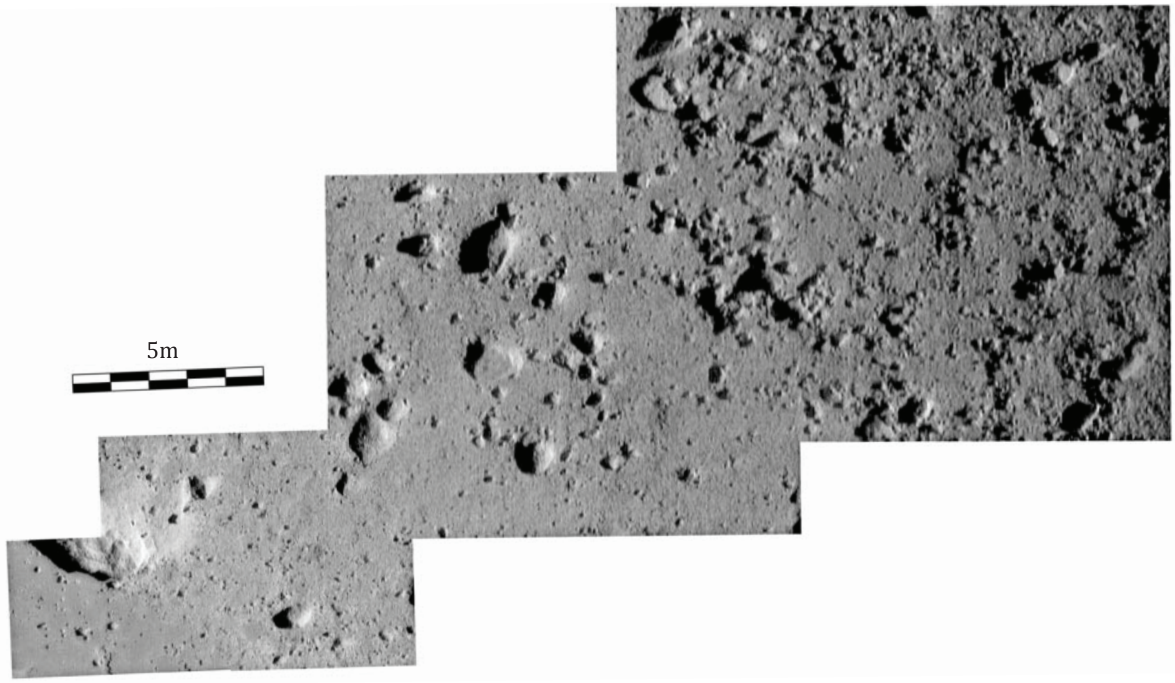

Figure 2.1: Last four images of NEAR-Shoemaker's decent sequenc towards Eros [4].

2.1.2 Hayabusa

The *Hayabusa* (previously *MUSES-C*) spacecraft was launched in 2003 by JAXA with the main goal of performing sample return on the 500-meter-wide asteroid 25143 Itokawa. Upon its arrival at Itokawa in 2007, the spacecraft performed extensive mapping of the global shape and surface of the asteroid and provided new theories on the formation of the body. Hayabusa measured Itokawa's mass as $(3.51 \pm 0.01) \times 10^{10}$ kg and its density as 1.9 ± 0.1 g/cm^3 [20].

The imagery resulting from the mission remains the most detailed available of any asteroid to date. Following this mapping, the spacecraft performed a descent and Touch-and-Go (TAG) on Itokawa's surface, during which it collected surface samples using its sampling horn. This horn, shown in Figure 2.2, extends from the main spacecraft bus and is sensitive to excessive velocities with respect to the asteroid surface. It was therefore paramount that the spacecraft touched the surfaced with a controlled and minimal velocity. Due to the communication delay, the spacecraft could not be controlled from ground and required extensive on-board autonomy to indeed control and guide Hayabusa downwards of an altitude of 500 m. To provide the spacecraft with independent navigation capabilities, it was fitted with several *target markers* [21].

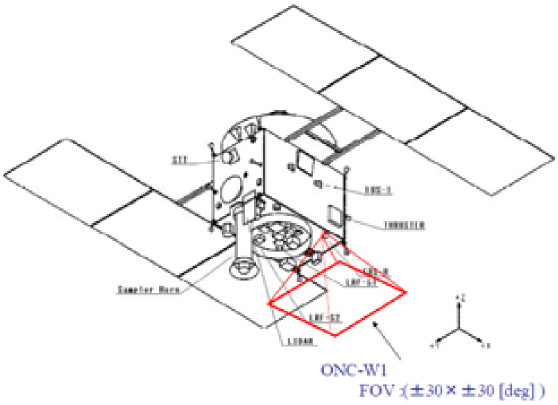

Figure 2.2: The Hayabusa spacecraft [22].

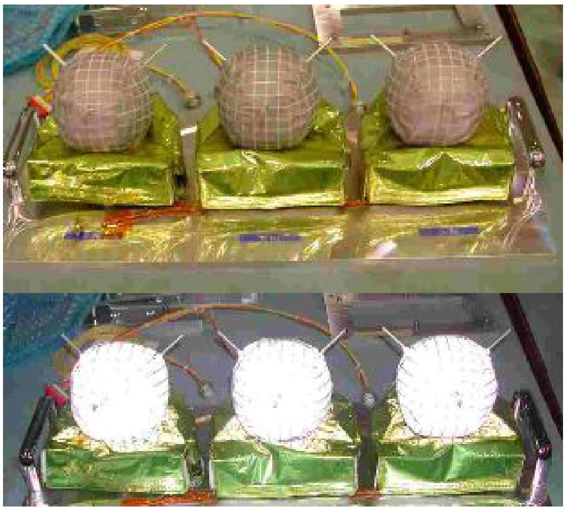

Figure 2.3: Hayabusa target markers [22].

The spherical target markers were released by the spacecraft from an altitude of ±40 m with a relative velocity of ±10 cm/s and used for accurate navigation once they settled on the surface. Constructed as hard spherical shells filled with small balls, this marker design yielded the lowest possible coefficient of restitution through internal energy dissipation, resulting in a minimal settling time [23]. This was desired as the spacecraft had to maintain a hovering condition while waiting for the target markers to settle, which requires continuous (and costly) fuel expenditure. It is finally noted that the markers were covered with a highly reflective material which increased their visibility when the spacecraft imagers used flash lamps. This effect can be seen in Figure 2.3, where the target makers are shown with and without the camera flash switched on.

Unfortunately, one of the target markers failed to reach Itokawa's surface, and a malfunctioning caused the spacecraft to soft-impact on Itokawa's surface. Despite these landing problems, Hayabusa eventually managed to capture a tiny surface sample and successfully return it to Earth [22]. It is finally noted that the spacecraft also carried and deployed the independent small *MINERVA* rover, which never reached the surface due to an error in the deployment phasing [24].

2.1.3 Rosetta

The *Rosetta* spacecraft was launched in early 2003 by ESA and arrived at comet *67P/Churyumov-Gerasimenko* in early August of 2014 [25]. In its mapping of the nucleus, Rosetta has produced the first-ever high-resolution images of a comet, revealing its highly irregular shape, as shown in Figure 2.4. The spacecraft will continue to obtain measurements of the comet's coma as it approaches the Sun and outgassing effects gradually become more noticeable. Furthermore, on 14 November 2014, Rosetta will deploy its *Philae* lander to the surface of 67P/CG from an altitude of 22.5 km. The particular release conditions will be selected in a way such that the unpowered lander package arrives at the surface with minimum velocity relative to the asteroid. Upon touching the surface, Philae will deploy several harpoons to anchor itself to the surface. After this landing, the 100-kg lander will perform a variety of scientific measurements of the comet (sub-)surface constituents [26, 27].

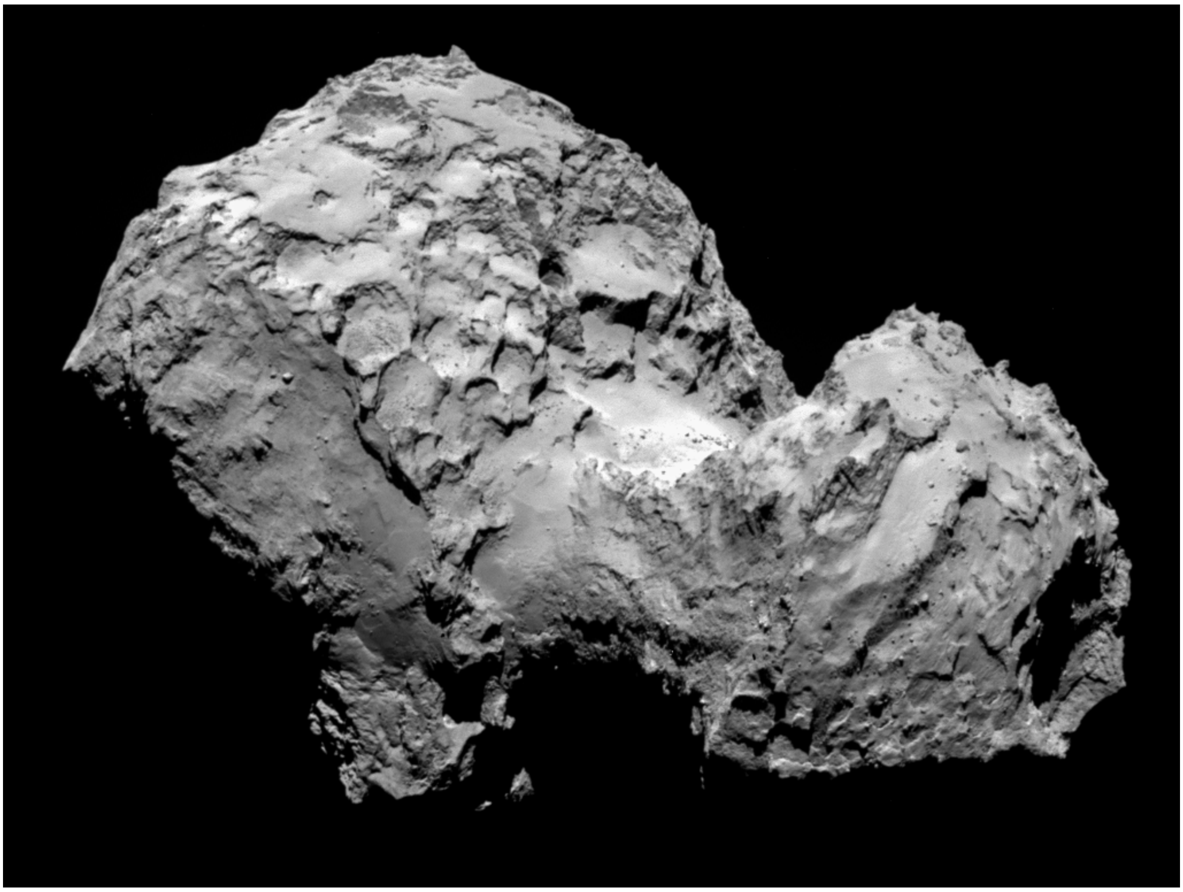

Figure 2.4: Comet 67P/Churyumov-Gerasimenko [27].

2.2 Future Missions

A number of missions planned or proposed for the future are discussed in the present section.

2.2.1 Hayabusa-2

The *Hayabusa-2* sample return mission is the follow-up of the successful Japan Aerospace Exploration Agency (JAXA) Hayabusa mission. It is set for launch in 2014 and will arrive at its target, the 1-kilometer-wide carbonaceous asteroid 1999 JU_3, in 2018. The scientific goals of Hayabusa-2 are highly similar to those of the original Hayabusa mission. Next to performing 'regular' sampling of the surface, the spacecraft will deploy an explosive impactor to the surface and sample the resulting crater. The descent and TAG is again guided through the use of target markers that are released from an altitude of $\sim$ 100 m [28]. Furthermore, the spacecraft will deploy from that same altitude the rectangular *MASCOT* lander [29] and three rectangular *MINERVA* hopping rovers [30], all of which are technology demonstration craft.

2.2.2 OSIRIS-REx

The *OSIRIS-REx* mission has been selected by NASA as part of its New Frontiers Program and will travel to the carbonaceous asteroid 1999 RQ_{36} to perform imaging and sample return. The mission is planned to launch in 2016 and will spend roughly half a year in orbit about its target, after which the spacecraft will perform a descent and TAG with sample collection [9]. As the spacecraft does not release any landers or target markers as navigation aids, it requires a highly accurate on-board Guidance, Navigation and Control (GNC) system. The uncertainties in position and velocity of this system are detailed in [31] and provide an excellent baseline design for GNC specifications to be used in the current research. The uncertainties are shown in Table 2.1 for different values of the asteroid gravitational parameter $\mu = GM$.

2.2.3 AIDA

The Asteroid Impact & Deflection Assessment (AIDA) joint mission is currently being proposed by both ESA and NASA and would target binary asteroid 65803 Didymos to demonstrate the first ever planetary defense technique[1], as well as characterize the characteristics of the system. The proposal consists of two spacecraft that are designed and operated independently of one another. The American Double Asteroid Redirection Test (DART) spacecraft is a kinetic impactor that aims to demonstrate deflection of Didymos' 150-meter-wide secondary body. Subsequent measurements of the orbit of the secondary will help establish an understanding of the dynamics of asteroid deflection; knowledge that is indispensable in

---

[1] Even though Didymos is not an Earth-crossing asteroid.

Table 2.1: OSIRIS-REx 3σ Navigation Uncertainty [31].

	Position Uncertainty [m]			Velocity Uncertainty [mm/s]		
	Radial	In-Track	Cross-Track	Radial	In-Track	Cross-Track
Low μ	1.040	2.750	0.718	0.133	0.060	0.049
Nominal μ	0.529	3.132	0.633	0.173	0.035	0.077
High μ	0.686	4.039	1.195	0.326	0.058	0.040

designing actual planetary defense missions. Additionally, the European Asteroid Impact Monitoring (AIM) orbiter will characterize the dynamical properties of the binary system, as well as provide detailed observations of DART's impact and the resulting crater, possibly using a lander/rover package. If selected, the mission is set to launch in 2019 and reach Didymos by 2022 [24, 32].

2.2.4 BASiX

The discovery-class Binary Asteroid in-situ Explorer (BASiX) mission is currently being proposed to NASA and aims to actively probe the geophysics of a binary asteroid system in a controlled and repeatable manner. Furthermore, it will make the first ever quantitative measurements of the strength, seismic properties, and mass morphology of an asteroid system. The target of the mission is the 1996 FG_3 binary system, which is well characterized in terms of size, spin , and orbit [6]. The two main scientific goals, which this mission has set to accomplish, are:

- To understand the unique geomorphology, dynamics, and evolution of a binary near-Earth asteroid; and
- To determine the strength, seismic, and space weathering properties of the surface and sub-surface of a near-Earth asteroid.

The mission aims to achieve these goals through the deployment of instrumentation packages to the surface(s) of the asteroid system. Rather than using complex and expensive controlled landers, BASiX will deploy a number of low-cost, low-risk, passive, spherical lander pods that descend to 1996 FG_3 on a ballistic trajectory, after which they bounce, roll, and eventually settle on the asteroid surface [6]. By carrying several of these pods and receiving their measurements, the BASiX mothership will be capable of estimating the previously mentioned fundamental properties at different locations along the asteroid surface. The lander pods were designed by *Ball Aerospace*, an aerospace company based in Colorado, USA. The pod hardware consists of low-cost imagers, accelerometers to detect impacts and seismic events, and a charge of high energy explosive to perform cratering and seismic experiments. All subsystems are contained within the spherical, orientation-independent structure. The baseline pod design and initial prototype are shown in Figure 2.5. The complete pod package is estimated to have a mass of less than 15 kg and a diameter of ±25 cm [33].

The detonation of a pod's explosive charge will generate seismic waves, which can be detected by the instruments of the other pods. By comparing the measured velocities of these waves between all pods, one can obtain information about the internal composition of the asteroid [2]. In addition, the orbiting mothership spacecraft will be able to observe the explosion and resulting crater with high-resolution imagery. It is desirable for the pods to be deployed to particular areas on the surface of an asteroid, to maximize the scientific return from the seismic measurements. This underscores the need for pod deployment to be aimed at specifically selected locations on the asteroid and justifies the study of lander deployment that is the subject of this research. The design of the BASiX mission and spacecraft together with its target binary system 1996 FG_3 provide excellent inputs to construct realistic mission scenarios for our research. The subsequent results may aid the BASiX mission designers in selecting release conditions for the pods and increase the chances of mission success.

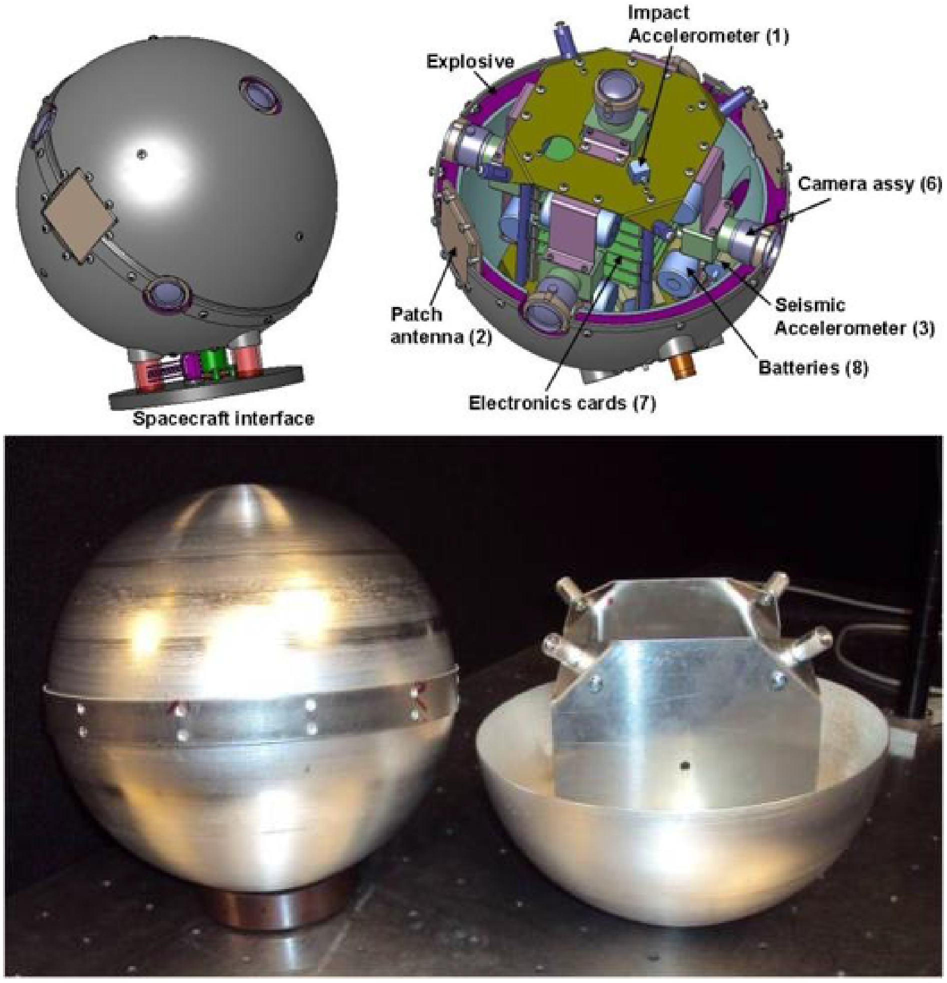
Impact
Accelerometer (1)
Explosive
Camera assy (6)
Patch
antenna (2)
Seismic
Accelerometer (3)
Batteries (8)
Electronics cards (7)
Spacecraft interface

Figure 2.5: (top) Baseline design and (bottom) initial prototype of the BASiX lander pods [33].

Chapter 3

Thesis Goals

Asteroids are primitive bodies which contain massive amounts of information about the early formation of our Solar system, may teach us invaluable lessons about planetary defense, and contain significant economic potential. Past missions to these bodies have provided us with basic insight of these factors, mostly through orbit-based observations. However, far more scientific return is contained within the asteroid surface, sub-surface, and interior structure; all of which remain mostly untouched to date. We can identify a clear scientific gap and therefore set the main, high-level research question to be answered by our research as:

Can we investigate the surface, sub-surface, and internal environment of asteroids?

Although parts of this investigation can be performed using again aforementioned orbit-based observations, far greater scientific return can be achieved through the application of surface-based lander/rover packages. We remark that all missions mentioned in the previous chapter already apply some form of landing on asteroids, either controlled or passive. In some cases the entire spacecraft touches down on the body, while in others one or more packages are deployed and used for navigational purposes and/or to independently carry out surface operations. The landing strategies employed by these missions vary widely and at times fail to deliver their payload to the target body surface, as seen, for example, in the case of Hayabusa's failed target marker and rover deployment. Due to this perceived difficulty in landing on a small body, mission designers are often reluctant to include landers in their approach to complete an asteroid mission's primary objectives. In doing so, they miss out on the enormous potential for scientific return that is contained by small body surfaces.

Fortunately, low-risk strategies for landing on both unitary and binary asteroid systems have been developed in recent works [12–14, 34]. These strategies guarantee, to a certain extent, the successful ballistic delivery of (spherical) landers to the surface of a target asteroid, following a release from the neighbourhood of equilibrium points of the target system's amended potential field. Although the general strategy has proven to be successful, characteristics of the resulting trajectories such as topographical spread and deployment time are sensitive to a number of interactions parameters, as well as the selected release conditions. To investigate the respective effect of these factors, we will develop a software package to accurately simulate lander trajectories and perform a sensitivity analysis. In doing so, we will be able to identify requirements for the mothership spacecraft GNC necessary to guarantee successful lander deployment. We therefore define the main research goal of this M.Sc. thesis, and break it down into three, smaller sub-goals to structure the research effort, as:

Numerically investigate the characteristics of strategies to
ballistically deploy landers to the surfaces of asteroids.

1. Develop a robust software package that can simulate trajectories of passive, spherical asteroid landers.
2. Apply this software package to perform a sensitivity analysis of both interaction and deployment parameters on the resulting lander trajectories.
3. Use the results of this sensitivity analysis to provide recommendations on the lander release conditions and related mothership GNC requirements.

The larger part of this research will be spent completing the first item, with significant amounts of time dedicated to the verification and validation of the developed software package. Only after the software has been designed and validated, can we proceed with producing the simulations required to complete sub-goals two and three.

Part II

Methods and Software

Chapter 4

Modelling

The motion of a lander in the environment of an asteroid system is a direct result of the forces and torques acting between that lander and its target. To be able to generate simulations of such motion, it is therefore necessary that we accurately model this environment, as is the focus of the present chapter. First, we present a number of reference frames in Section 4.1 that are applied in Section 4.2 to define the relevant state variables. Next, Section 4.3 discusses modelling of asteroid shapes and the associated gravity fields. The forces and torques active during contact motion of a lander on the asteroid surface are discussed in Section 4.4, and during collisions in Section 4.5. The applied stochastic rock model is presented in Section 4.6, and Section 4.7, finally, synthesizes this force model into the equations of motion used to propagate lander motion in our simulation software.

4.1 Reference Frames

Any description of the motion of a spacecraft or lander operating in the neighbourhood of an asteroid requires the definition of a reference frame with respect to which this motion is expressed. A large number of reference frames exists, with each frame having specific advantages relating to the simplicity of expressing particular forces or motions. The current section provides an overview of the reference frames that are applied in our simulations of asteroid landers, for respectively unitary and binary systems, and briefly discusses their applications.

4.1.1 Unitary Sytems

A total of four distinct reference frames are applied in the simulation of landers operating in a *unitary* asteroid system; they are listed below. The relative position, motion, and rotation between the four frames is illustrated in Figure 4.1.

1. The Solar Inertial Frame (SIF) is a pseudo-inertial reference frame with its origin at the center of mass of the Sun and axis directions fixed with respect to a number of extragalactic sources. This reference frame will be applied to express the motion of the asteroid body around the Sun.

2. The Target Inertial Frame (TIF) is a pseudo-inertial reference frame with its origin at the center of mass of the (unitary) asteroid body and the same axis directions as the SIF. This frame moves relative to the SIF, following the Keplerian orbit of the asteroid. The TIF is applied, in certain cases, to express the motion of the lander relative to the asteroid.

3. The Rotating Body-1 Frame (RB1F) is a rotating, non-inertial reference frame with its origin at the center of mass of the (unitary) asteroid body and axes fixed with respect to that asteroid body. The RB1F therefore has the same origin as the TIF, but rotates around the TIF with the same rotation rate as the asteroid. The RB1F is also applied, in certain cases, to express the motion of the lander relative to the asteroid. It is finally also used to express the rotation state of the (unitary) asteroid body.

4. The Spacecraft-Centered Frame (SCF) is a reference frame with its origin at the center of mass of the lander and axis directions fixed wtih respect to the lander. The SCF is applied to express the rotation state of the lander.

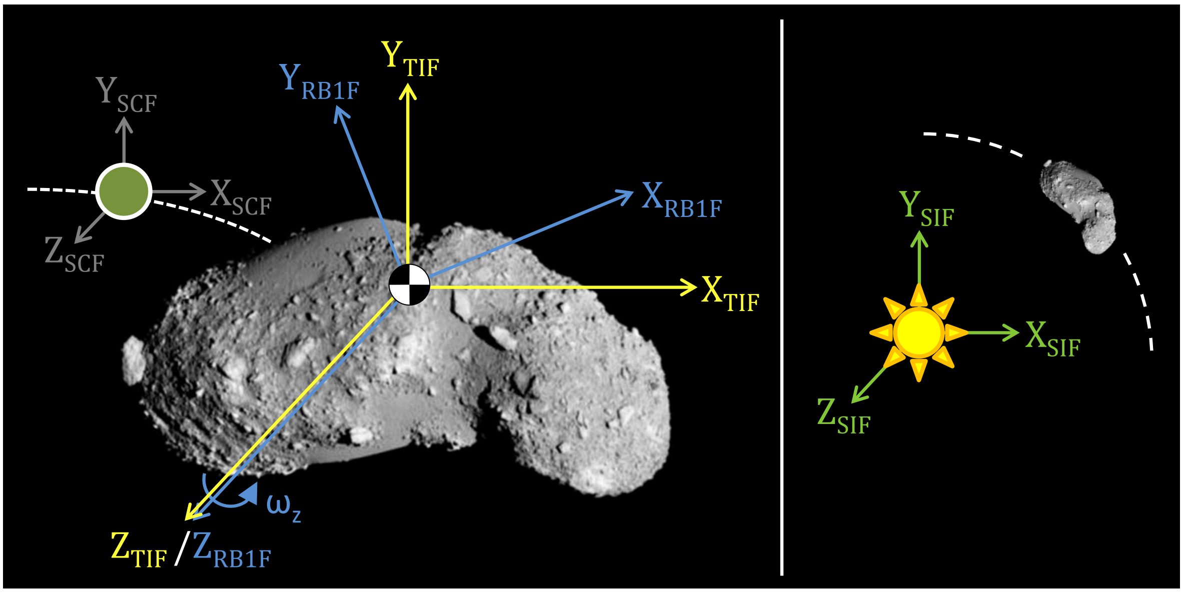

Figure 4.1: Overview of applied reference frames in unitary asteroid systems. Photo source: JAXA.

4.1.2 Binary Systems

Analogously, a total of five reference frames are applied in simulations of a lander operating in a *binary* asteroid system, as listed below. The relative motion and rotation between the five frames is illustrated in Figure 4.2.

1. The SIF is defined in the same manner as was done for unitary asteroid systems.
2. The TIF is a pseudo-inertial reference frame with its origin at the *mutual* center of mass of the two asteroid bodies in the binary system and the same axis directions as the SIF. This frame moves relative to the SIF, following the Keplerian orbit of the binary system. The TIF is applied, in certain cases, to express the motion of the lander with respect to the asteroid. It is furthermore applied to express the motion of both primary and secondary asteroid bodies as a result of their mutual gravitational attraction.
3. The RB1F is defined in the same manner as was done for unitary asteroid systems. The RB1F therefore follows the movement of the primary around the TIF and has the same rotation rate as the primary. This frame is applied to express, in certain cases, the motion of the lander with respect to the primary body. Finally, it is used to express the rotation state of the latter.
4. The Rotating Body-2 Frame (RB2F) is defined in the same way as the RB1F, but instead fixed to the *secondary* body. This frame is applied to express, in certain cases, the motion of the lander with respect to the secondary body. Finally, it is used to express the rotation state of the latter.
5. The SCF is defined in the same manner as was done for unitary asteroid systems.

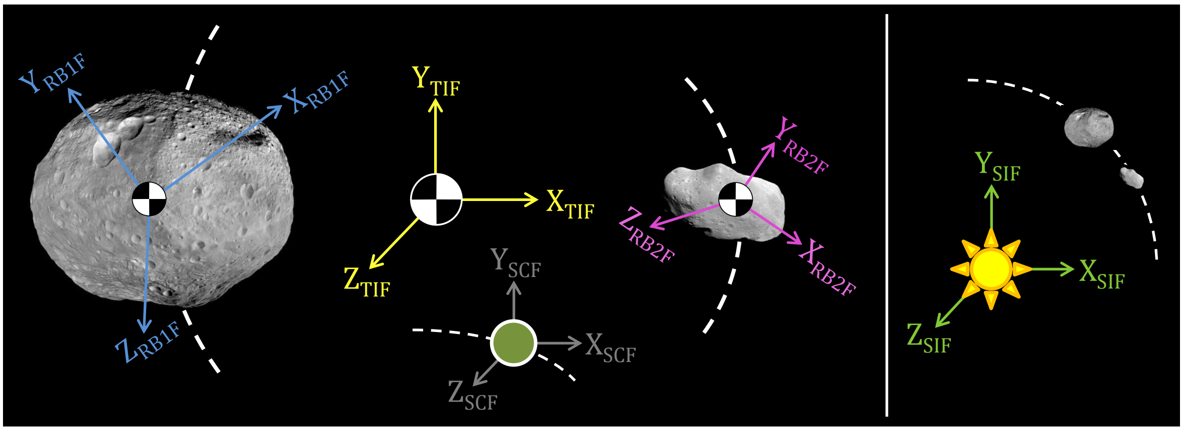

Figure 4.2: Overview of applied reference frames in binary asteroid systems. Photo source: NASA.

4.2 State Variables

The reference frames defined above are applied to express the equations of motion of the considered asteroid-lander simulations. The number of state variables propagated in these simulations and their respective frames of expression are a function of the selected propagation mode, as will be detailed here. In any case, we require knowledge of the position ($X/Y/Z$) and velocity ($V_x/V_y/V_z$) of the lander as we desire to perform a study of this motion. Additionally, we know that contact interactions with between the lander and the asteroid surface will also affect, and be affected by, the attitude of the lander. As a result, we also include the quaternion[1] attitude ($q_1/q_2/q_3/q_4$) and rotation rates ($\omega_x/\omega_y/\omega_z$) of the lander.

The motion of a lander in an asteroid system is a result of accelerations from the asteroid(s) and perturbations from the Sun[2]. We therefore also require knowledge of the position and orientation of the asteroid system relative to the Sun, and relative to itself in the case of a binary system. For a unitary system, we therefore include the position, velocity, and orientation of the asteroid relative to the Sun, and the rotation rates of the asteroid. For binary systems, this is expanded to the position, velocty, orientation, and rotation of the two asteroid bodies relative to their mutual center of mass, as well as the position and velocity of this center of mass relative to the Sun. By including all of these state variables, we can account for any orientation of the lander and the asteroid system relative to one another and the Sun. An overview of these state variables is shown in Table 4.1; we observe that there are a total of 26 variables propagated for a unitary system, and a total of 45 variables for a binary system.

We have now selected the state variables for our simulations, but must still attribute reference frames with respect to which these variables are expressed. These particular frames are a function of the selected mode of propagation of a given simulation. As shown in Table 4.1, we have defined two propagation modesfor unitary systems (identifier *Uni*) and three for binary systems (identifier *Bin*). When propagating in mode *Uni 0* or *Bin 0*, we ignore contact interactions and propagate the position, velocity, and orientation of the lander spacecraft *S/C* in the TIF. Modes *Uni 1* and *Bin 1* propagate the lander in the RB1F, and include contact interactions with the primary body. Finally, mode *Bin 2* propagates the lander in the RB2F and includes contact with the secondary body. As unitary systems consist of only a single body, no *Uni 2* mode exists. It can be seen that the motion and attitude of the lander is always propagated in the frame of the body with which contact interactions are included, since these interactions are given in the body-fixed frame of the surface target, see also Section 4.4.

---

[1] While other methods for expressing an object's orientation are available, we choose the use quaternions since they are free of singularities.

[2] Where perturbations from other Solar system bodies are ignored.

Regardless of the selected propagation mode, the motion and attitude of a unitary asteroid *B1* is expressed in the SIF. For binary systems, the motion and attitude of the two bodies *B1* and *B2* are expressed in the TIF, with the motion of the center of mass of the system T expressed in the SIF. Finally, the rotation rates of any object are always expressed relative to that system itself, independent of propagation mode.

Now that we have defined the relevant state variables along with their respective propagation frames, it is possible to present a description of the applied modelling of forces and torques present in an asteroid system, starting with shape and gravity modelling of asteroid bodies.

4.3 Asteroid Shape and Gravity

A number of different techniques for modelling the gravitational field of an asteroid are available. Two frequently-used models are *ellipsoidal* and the *spherical harmonics* models. Although these models are very practical when simulating the motion of orbiting spacecraft, they cannot be used within the circumscribing radius of a body due to convergence problems, and as a result are unusable in the propagation of lander motion [35]. We therefore model gravitational fields using the *constant-density polyhedron model*, which converges even on the surface of an irregular body.

All asteroids in this research are therefore modelled using *polyhedra*. A polyhedron is defined as a three-dimensional body consisting of a number of points known as *vertices*, which together form a set of interconnected triangular *facets*. Polyhedral models for different asteroids are available online as a set of vertex coordinates together with a listing of the three points each facet consists of. These two lists also allow for the construction of a third list of the *edges* contained by that polyhedron. Furthermore, one outward-pointing normal is defined for every vertex, edge and facet, with respective notations $\mathbf{N}_\mathcal{V}$, $\mathbf{N}_\mathcal{E}$ and $\mathbf{N}_\mathcal{F}$. The numerical method applied to obtain these outward-pointing normals will be discussed in detail in Section 5.1. Finally, if we denote the number of facets, edges and vertices as respectively $n_\mathcal{F}$, $n_\mathcal{E}$ and $n_\mathcal{V}$, we may apply the Descartes-Euler polyhedral formula, which states that [36]:

$$n_\mathcal{V} + n_\mathcal{F} - n_\mathcal{E} = 2 \tag{4.1}$$

This formula can be used during the creation of the polyhedron edges to verify whether the correct number of edges has been created. The geometry of an arbitrary polyhedron is shown in Figure 4.3; the polyhedral model of binary asteroid system 1999 KW$_4$ is shown in Figure 4.4. Please note that the primary and secondary body are not shown at correct relative size and distance. The coloring of the asteroid facets is indicative of their local amended geopotential; red indicates high potential, blue indicates low potential. Using the outward-pointing facet normals, the dyad $\mathbf{E}_{\mathcal{E}_{ij}}$ of the edge connecting two facets $\mathcal{F}_{ijk}$ and $\mathcal{F}_{ijl}$ is given

Table 4.1: Overview of state variables used in simulations.

		Bin 0	Bin 1	Bin 2	Uni 0	Uni 1
S/C	X	TIF	RB1F	RB2F	TIF	RB1F
	Y	TIF	RB1F	RB2F	TIF	RB1F
	Z	TIF	RB1F	RB2F	TIF	RB1F
	V_x	TIF	RB1F	RB2F	TIF	RB1F
	V_y	TIF	RB1F	RB2F	TIF	RB1F
	V_z	TIF	RB1F	RB2F	TIF	RB1F
	q_1	TIF	RB1F	RB2F	TIF	RB1F
	q_2	TIF	RB1F	RB2F	TIF	RB1F
	q_3	TIF	RB1F	RB2F	TIF	RB1F
	q_4	TIF	RB1F	RB2F	TIF	RB1F
	ω_x	SCF	SCF	SCF	SCF	SCF
	ω_y	SCF	SCF	SCF	SCF	SCF
	ω_z	SCF	SCF	SCF	SCF	SCF
B1	X	TIF	TIF	TIF	SIF	SIF
	Y	TIF	TIF	TIF	SIF	SIF
	Z	TIF	TIF	TIF	SIF	SIF
	V_x	TIF	TIF	TIF	SIF	SIF
	V_y	TIF	TIF	TIF	SIF	SIF
	V_z	TIF	TIF	TIF	SIF	SIF
	q_1	TIF	TIF	TIF	SIF	SIF
	q_2	TIF	TIF	TIF	SIF	SIF
	q_3	TIF	TIF	TIF	SIF	SIF
	q_4	TIF	TIF	TIF	SIF	SIF
	ω_x	RB1F	RB1F	RB1F	RB1F	RB1F
	ω_y	RB1F	RB1F	RB1F	RB1F	RB1F
	ω_z	RB1F	RB1F	RB1F	RB1F	RB1F
B2	X	TIF	TIF	TIF		
	Y	TIF	TIF	TIF		
	Z	TIF	TIF	TIF		
	V_x	TIF	TIF	TIF		
	V_y	TIF	TIF	TIF		
	V_z	TIF	TIF	TIF		
	q_1	TIF	TIF	TIF		
	q_2	TIF	TIF	TIF		
	q_3	TIF	TIF	TIF		
	q_4	TIF	TIF	TIF		
	ω_x	RB2F	RB2F	RB2F		
	ω_y	RB2F	RB2F	RB2F		
	ω_z	RB2F	RB2F	RB2F		
T	X	SIF	SIF	SIF		
	Y	SIF	SIF	SIF		
	Z	SIF	SIF	SIF		
	V_x	SIF	SIF	SIF		
	V_y	SIF	SIF	SIF		
	V_z	SIF	SIF	SIF		

by [35]:

$$\mathbf{E}_{\mathcal{E}_{ij}} = \mathbf{N}_{\mathcal{F}_{ijk}}\mathbf{N}_{\mathcal{E}_{ij}} + \mathbf{N}_{\mathcal{F}_{ijl}}\mathbf{N}_{\mathcal{E}_{ji}} \tag{4.2}$$

In this equation, $\mathbf{N}_{\mathcal{E}_{ij}}$ is the edge normal perpendicular to both the adjacent facet $\mathcal{F}_{ijk}$ and the edge $\mathcal{E}_{ij}$, pointing away from the center of that facet. Analogously, the dyad of a facet $\mathcal{F}_{ijk}$ is given by [35]:

$$\mathbf{F}_{\mathcal{F}_{ijk}} = \mathbf{N}_{\mathcal{F}_{ijk}}\mathbf{N}_{\mathcal{F}_{ijk}} \tag{4.3}$$

All dyads are pre-computed prior to propagation as they are invariant in time; this decreases the computation effort required in simulating lander motion. By applying again the same geometry, it is possible to define the *per-edge factor* $L_{\mathcal{E}_{ij}}$ of an arbitrary edge connecting vertices $\mathbf{P}_i$ and $\mathbf{P}_j$, using [35]:

$$L_{\mathcal{E}_{ij}} = \ln\left(\frac{r_i + r_j + e_{ij}}{r_i + r_j - e_{ij}}\right) \tag{4.4}$$

In this equation, $r_i = \|\mathbf{r}_i\|$ and $r_j = \|\mathbf{r}_j\|$ are the lengths of the vectors from these two vertices to the field-point $\mathbf{P}$ at which the potential is being evaluated, and $e_{ij} = \|\mathbf{r}_j - \mathbf{r}_i\|$ is the length of said edge, the latter of which is also pre-computed. The *per-face factor* $\omega_{\mathcal{F}_{ijk}}$ of an arbitrary face connecting vertices $\mathbf{P}_i$, $\mathbf{P}_j$ and $\mathbf{P}_k$ is defined through:

$$\omega_{\mathcal{F}_{ijk}} = 2\arctan\left[\frac{\mathbf{r}_i\cdot\,(\mathbf{r}_j\times\mathbf{r}_k)}{r_ir_jr_k + r_i(\mathbf{r}_j\cdot\mathbf{r}_k) + r_j(\mathbf{r}_k\cdot\mathbf{r}_i) + r_k(\mathbf{r}_i\cdot\mathbf{r}_j)}\right] \tag{4.5}$$

We note that the per-face factor $\omega_{\mathcal{F}_{ijk}}$ also expresses the signed solid angle covered by the face under consideration [35]. Using the given expressions, the gravitational potential, gravitational attraction and gravity-gradient matrix may be expressed in the asteroid-fixed frame through, respectively [35]:

$$U = \frac{1}{2}G\rho\sum_{\forall\mathcal{E}_{ij}}\mathbf{r}_{\mathcal{E}_{ij}}\cdot\mathbf{E}_{\mathcal{E}_{ij}}\cdot\mathbf{r}_{\mathcal{E}_{ij}}\cdot L_{\mathcal{E}_{ij}} - \frac{1}{2}G\rho\sum_{\forall\mathcal{F}_{ijk}}\mathbf{r}_{\mathcal{F}_{ijk}}\cdot\mathbf{F}_{\mathcal{F}_{ijk}}\cdot\mathbf{r}_{\mathcal{F}_{ijk}}\cdot\omega_{\mathcal{F}_{ijk}} \tag{4.6}$$

$$\nabla U = -G\rho\sum_{\forall\mathcal{E}_{ij}}\mathbf{E}_{\mathcal{E}_{ij}}\cdot\mathbf{r}_{\mathcal{E}_{ij}}\cdot L_{\mathcal{E}_{ij}} + G\rho\sum_{\forall\mathcal{F}_{ijk}}\mathbf{F}_{\mathcal{F}_{ijk}}\cdot\mathbf{r}_{\mathcal{F}_{ijk}}\cdot\omega_{\mathcal{F}_{ijk}} \tag{4.7}$$

$$\nabla\nabla U = G\rho\sum_{\forall\mathcal{E}_{ij}}\mathbf{E}_{\mathcal{E}_{ij}}\cdot L_{\mathcal{E}_{ij}} - G\rho\sum_{\forall\mathcal{F}_{ijk}}\mathbf{F}_{\mathcal{F}_{ijk}}\cdot\omega_{\mathcal{F}_{ijk}} \tag{4.8}$$

In these equations, $\mathbf{r}_{\mathcal{E}_{ij}}$ and $\mathbf{r}_{\mathcal{F}_{ijk}}$ are the vectors from the field point $\mathbf{P}$ to respectively any vertex of edge $\mathcal{E}_{ij}$ and facet $\mathcal{F}_{ijk}$. We note that the Laplacian[3] of the gravity field can be computed using [35]:

---

[3] The Laplacian operator $\nabla^2 U$ expresses the divergence of a function in Cartesian space.

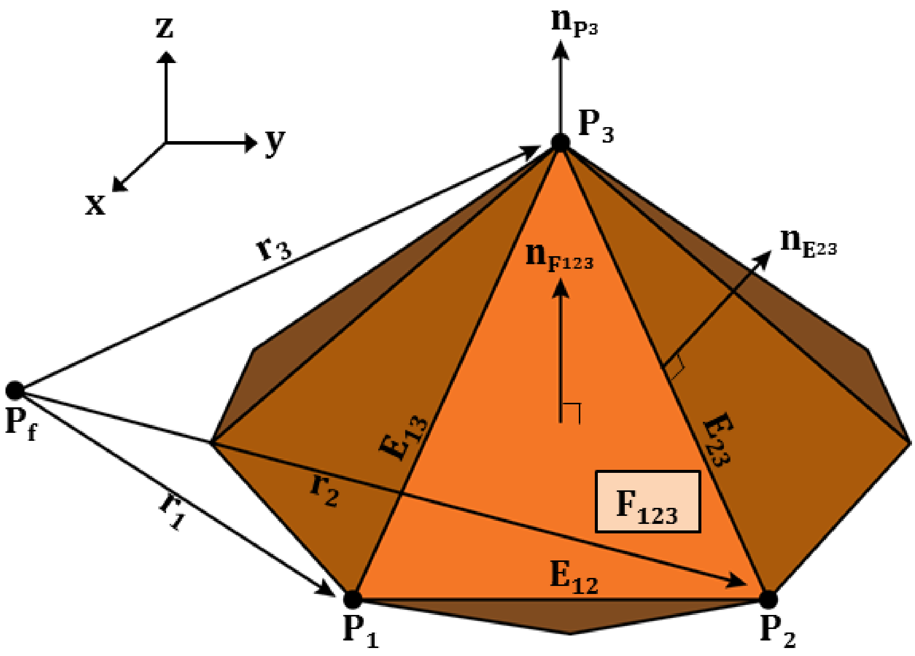

Figure 4.3: Example of polyhedron geometry.

$$\nabla^2 U = -G\rho \sum_{\forall \mathcal{F}_{ijk}} \omega_{\mathcal{F}_{ijk}} \tag{4.9}$$

One may observe that this factor is included in the above polyhedron attraction Equations 4.6 through 4.8. It is mentioned in [35] that this Laplacian operator may be used to determine whether a given field point is located inside or outside of the attracting body, by applying the following criterion:

$$\nabla^2 U = \begin{cases} 0 & \text{if } \mathbf{P} \text{ interior} \\ -4\pi G\rho & \text{if } \mathbf{P} \text{ exterior} \end{cases} \tag{4.10}$$

Unfortunately, this criterion is only applicable if we are indeed checking for collisions between a single field point and the asteroid surface. Even if we were to strongly simplify the model of a lander, it would still consist of a large number of points. As the computation of the Laplacian requires summation over all facets of the asteroid model, and high-resolution polyhedra consist of over a hundred thousand facets, applying this criterion would be very computationally intensive. Instead, we will resort to a geometric detection of collisions between the lander and an asteroid; this method is detailed will be Section 5.2.

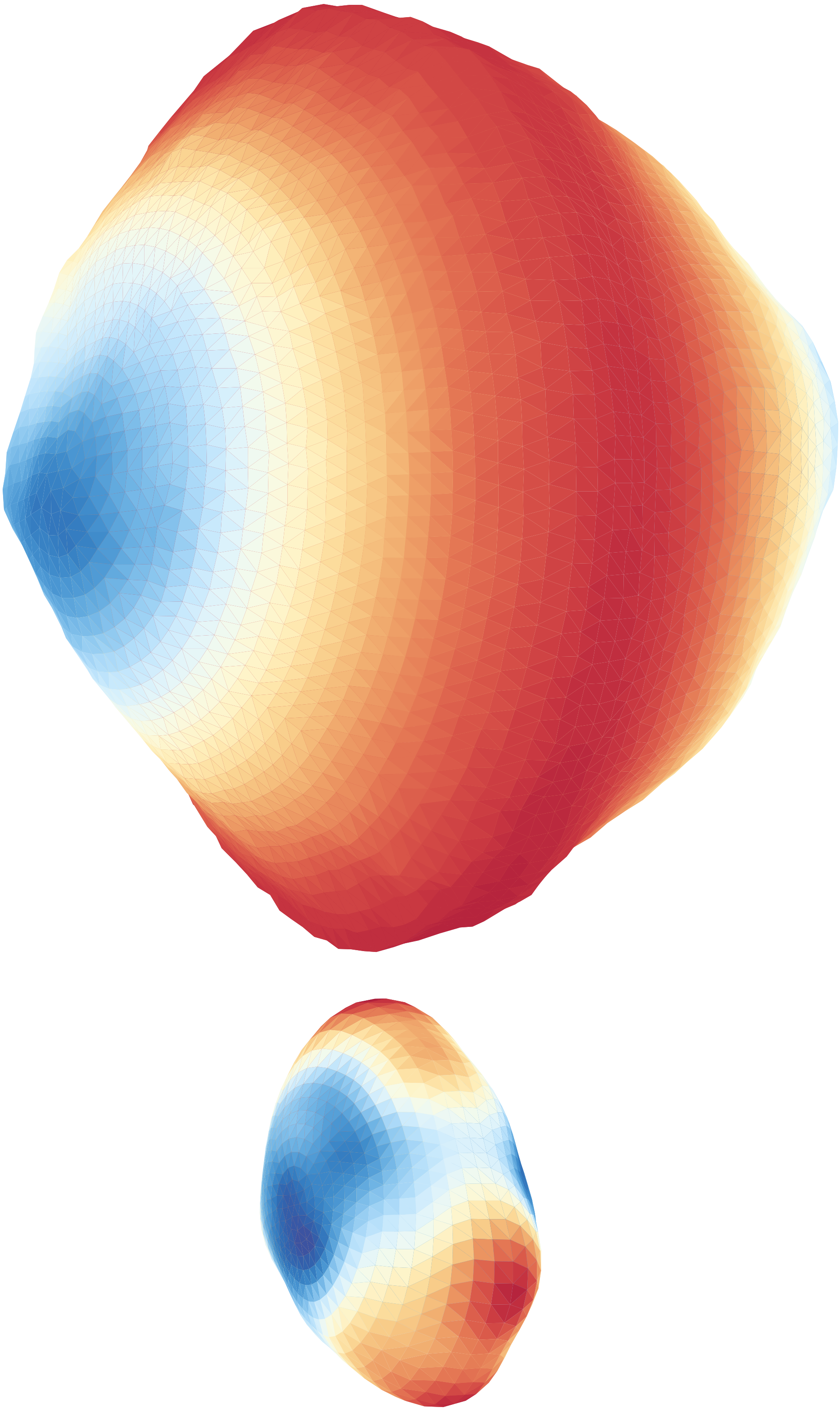

Figure 4.4: Polyhedron model of binary asteroid system 1999 KW$_4$ (size and distance not to scale).

Gravity Linearization

We observe from Equation 4.7 that a computation of the gravitational attraction ∇U at some field point $\mathbf{P}$ in the neighbourhood of an asteroid requires summation over all facets and edges of that asteroid's polyhedron model. As even low-resolution asteroid polyhedra consist of several hundreds of facets, such a summation is computationally intensive. As our research requires the simulation of a large number of lander trajectories, it is paramount that the simulations are carried out rapidly. Moreover, the time steps applied by our numerical integrator during propagation of contact motion are small, such that the gravitational acceleration experienced by a lander is unlikely to vary considerably between consecutive integration steps. We therefore apply linearization to the polyhedral gravity model presented above [4]. Indeed, Equation 4.8 provides an expression for the gravity-gradient matrix, which expresses the local variation in gravitational attraction. Assuming that we have previously computed the gravitational potential U_0, the gravitational attraction ∇U_0, and the gravity-gradient matrix $\nabla\nabla U_0$ at some reference state $\mathbf{X}_0$, the gravitational potential and attraction at a nearby state $\mathbf{X}$ can be estimated, again in the asteroid-fixed frame, as respectively:

$$U = U_0 + (\mathbf{X} - \mathbf{X}_0)\nabla U_0 + (\mathbf{X} - \mathbf{X}_0)\nabla\nabla U_0(\mathbf{X} - \mathbf{X}_0) \tag{4.11}$$

$$\nabla U = \nabla U_0 + (\mathbf{X} - \mathbf{X}_0)\nabla\nabla U_0 \tag{4.12}$$

We note that Equations 4.11 and 4.12 provide approximations that are valid only in the neighbourhood of the reference state $\mathbf{X}_0$. Linearization therefore requires the user to define some limit $\Delta\mathbf{X}_{max} = (\mathbf{X} - \mathbf{X}_0)_{max}$ that specifies the maximum distance from the reference state $\mathbf{X}_0$ within which linearization may be applied by the simulator. If $\mathbf{X}$ lies outside of this range, the velocity $\mathbf{V}$ is used to predict a new reference state $\mathbf{X}_1$ at which the gravitational field is evaluated and used in subsequent integration steps, until $\Delta\mathbf{X}_{max}$ is once again crossed, as illustrated in Figure 4.5. This process is continually repeated by keeping track of the most recent 'full' polyhedron evaluation, and results in faster propagation of the equations of motion, particularly during contact motion where small time steps are applied.

4.4 Contact Motion

Upon reaching the surface of its target asteroid, a lander will be subjected to a number of contact forces and torques in addition to the force of gravity. In this section, the three interactions that result in these forces and torques are presented. When taken together, these elements capture the complex contact between a lander and the surface of an asteroid. We note that all expressions in the present section are given with respect to the asteroid-fixed

---

[4] While we could use other, faster models to represent the asteroid gravity field, the reader is reminded that these models do not converge inside of a body's circumscribing radius.

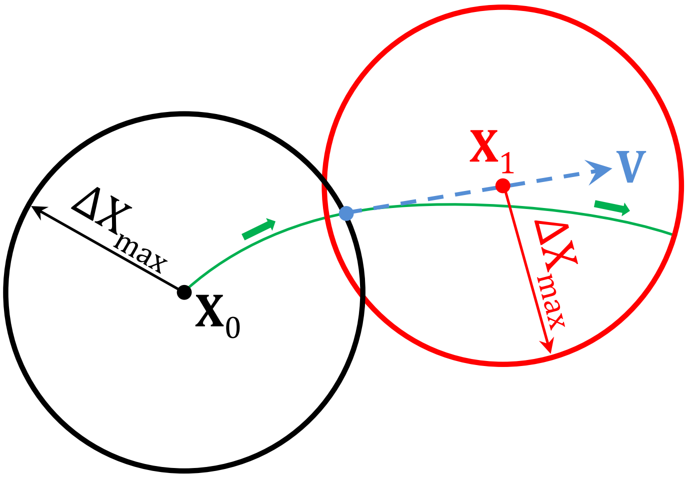

Figure 4.5: Gravity linearization. The direction of motion is indicated by arrows.

reference frame (either RB1F or RB2F). Furthermore, we repeat that our lander models are spherical.

4.4.1 Normal Force

In the propagation of lander contact motion, the *normal force* enforces the condition of non-penetration, which ensures that the lander pod does not cross through the asteroid surface. It acts, as its name already suggests, in the direction normal to the local surface plane. In the case of the polyhedral asteroid model used in our simulations, this direction is, in fact, given by the outward-pointing normal of the facet(s) the pod is in contact with. The magnitude of the normal force $\mathbf{F}_N$ may be expressed as [16]:

$$\mathbf{F}_N = -(\mathbf{F}_e \cdot \mathbf{u}_r)\mathbf{u}_r \tag{4.13}$$

In this equation, $\mathbf{F}_e$ is the external force[5] acting on the lander and $\mathbf{u}_r$ is the unit vector from the center of the lander pod to the surface contact point $\mathbf{H}$. However, this equation is valid only when the pod is in contact with a flat surface, such as the interior of a facet. As such, Equation 4.13 is *not* valid when the pod reaches an edge or vertex of that facet, as in those cases the vector $\mathbf{u}_r$ is not constant. To account for these cases, it is necessary to include the time derivative of $\mathbf{u}_r$, which directly relates to the angular velocity of the center of the pod with respect to the facet as [16]:

$$\dot{\theta} = \left| \frac{d\mathbf{u}_r}{dt} \right| \tag{4.14}$$

---

[5] In our simulations, the external acceleration consists of gravitational and virtual accelerations; this is discussed in more detail in Section 4.7.

The value of the angular velocity $\dot{\theta}$ may be computed as [16]:

$$\dot{\theta} = \left|\frac{d\mathbf{u}_r}{dt}\right| = \begin{cases} 0 & \text{on face.} \\ \frac{|\mathbf{V} - (\mathbf{V}\cdot\hat{\mathbf{e}})\hat{\mathbf{e}}|}{r} & \text{on edge.} \\ \frac{|\mathbf{V}|}{r} & \text{on vertex.} \end{cases} \tag{4.15}$$

In these equations, $\hat{\mathbf{e}}$ is the unit vector of the edge under consideration, aligned from one vertex to the other, and $\mathbf{V}$ is the velocity of the center of the pod with respect to the facet under consideration. Using Equation 4.15, the normal force as given by Equation 4.13 may be generalized to any contact situation as [16]:

$$\mathbf{F}_N = \left(m\dot{\theta}^2 R - \mathbf{F}_e \cdot \mathbf{u}_r\right)\mathbf{u}_r \tag{4.16}$$

The geometry and force application of the flat and edge cases are shown in Figure 4.6. As explained by Equation 4.15, the term $m\dot{\theta}^2 R$ in Equation 4.16 is non-zero only when the pod rolls off the edge or vertex of a facet. Indeed, this will decrease the magnitude of the normal force and allow gravity to exert a net acceleration on the pod with respect to the plane of the facet; the pod will move downward, analogous to the way a ball starts moving down as it is rolling off the edge of a table.

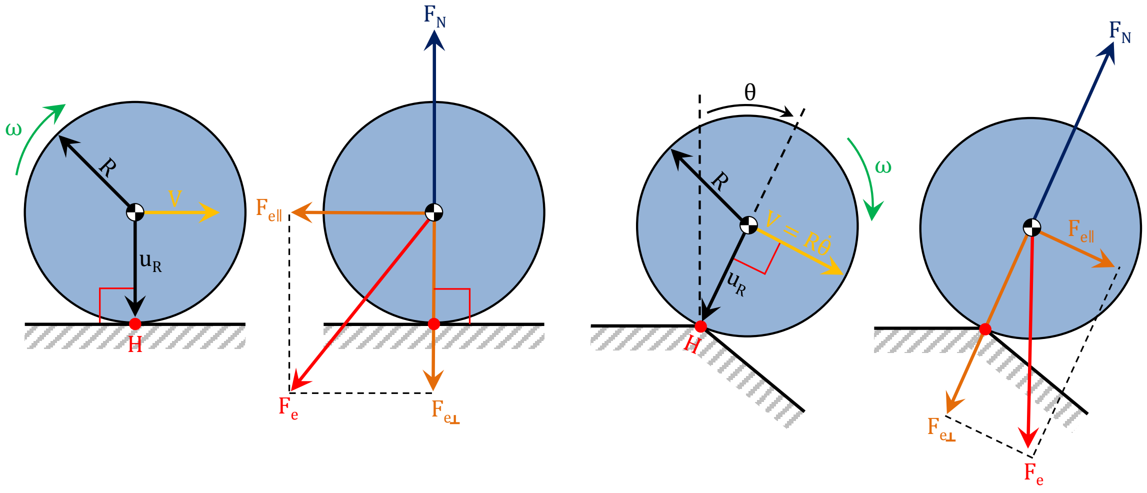

(a) Flat case. **(b)** Edge case.

Figure 4.6: Illustration of geometry and force application.

4.4.2 Coulomb Friction

The Coulomb friction force $\mathbf{F}_f$ is the force resisting the relative motion of two objects in sliding contact and is the result of micro-imperfections. Its magnitude may be expressed for our spherical landers as [16]:

$$\mathbf{F}_f = \begin{cases} 0 & \text{for } \mathbf{v}_H = 0 \text{ and } \mathbf{a}_H = 0 \\ -\min\left(|m\mathbf{a}_H|, |f\mathbf{F}_N|\right)\frac{\mathbf{a}_H}{|\mathbf{a}_H|} & \text{for } \mathbf{v}_H = 0 \text{ and } \mathbf{a}_H \neq 0 \\ -|f\mathbf{F}_N|\frac{\mathbf{v}_H}{|\mathbf{v}_H|} & \text{for } \mathbf{v}_H \neq 0 \end{cases} \tag{4.17}$$

In this equation, $\mathbf{v}_H$ and $\mathbf{a}_H$ are respectively the velocity and acceleration of the contact point **H**. Note that the friction force is zero when the pod is completely stationary; the other two equations model static and dynamic friction. Furthermore, the expression for $\mathbf{a}_H \neq 0$ in Equation 4.17 enforces a check such that the acceleration produced by friction on a lander pod with zero velocity never exceeds the external acceleration; in other words, friction may never accelerate the pod into motion from a resting condition.

The coefficient of friction $f \geq 0$ is a measure of the magnitude of friction between the pod and the asteroid surface and is dependent on the characteristics of the mutual contact. The particular values of f applied in our simulations will be discussed further on. Although the friction force effectively decelerates the pod as it moves across the surface of the asteroid, its main contribution results from the related friction torque. Since $\mathbf{F}_f$ does not act at the center of mass of the pod, but rather at the contact point **H**, it generates an associated torque $\mathbf{L}_f$ [16]:

$$\mathbf{L}_f = r\mathbf{u}_r \times \mathbf{F}_f \tag{4.18}$$

Through this torque, the friction force acts to bring the contact-point velocity (if any) to zero. For a spherical pod, this does not imply the total velocity of the pod is zero, as $\mathbf{v}_H = 0$ when the rotation of the sphere matches its velocity and no slip occurs[6]. It is precisely this torque that causes a ball, sliding across a surface, into a rolling motion where its velocity and rotation are matched. The geometry involved in the computation of the Coulomb friction force and torque are shown in Figure 4.7. We note that this figure illustrates the simplified two-dimensional case; our equations are capable of handling the full, three-dimensional case where the pod rotation and velocity may act in any arbitrary direction.

4.4.3 Rolling Resistance

The Coulomb friction force discussed above acts only when the contact point velocity $\mathbf{v}_H$ is non-zero. This means that a lander pod will not experience any deceleration when its velocity $\mathbf{v}_H$ and rotation $\boldsymbol{\omega}$ are matched according to $\mathbf{v}_H = \boldsymbol{\omega} r$; the pod will continue rolling indefinitely as there is no mechanism for further energy dissipation. Our intuition immediately disagrees with this, as a rolling ball will eventually come to a full stop. Indeed, such a mechanism exists and is enforced by *rolling resistance*, which generates, on a rolling object, a torque $\mathbf{L}_{rr}$ with magnitude [16]:

---

[6] This is the case whenever $V = \omega R$.

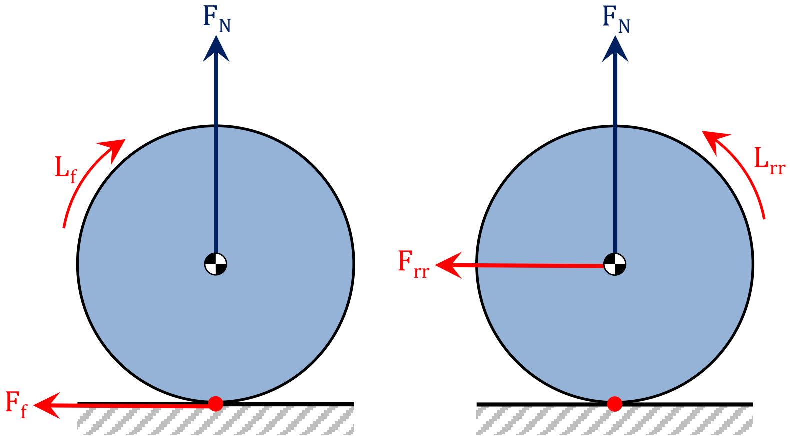

Figure 4.7: Geometry and application of (left) Coulomb friction and (right) rolling resistance.

$$\mathbf{L}_{rr} = \begin{cases} 0 & \text{for } \boldsymbol{\omega} = 0 \text{ and } \dot{\boldsymbol{\omega}} = 0 \\ -\min\left(\left|\bar{I}\dot{\boldsymbol{\omega}}\right|, \left|rC_{rr}\mathbf{F}_N\right|\right)\frac{\bar{I}\dot{\boldsymbol{\omega}}}{\left|\bar{I}\dot{\boldsymbol{\omega}}\right|} & \text{for } \boldsymbol{\omega} = 0 \text{ and } \dot{\boldsymbol{\omega}} \neq 0 \\ -\left|rC_{rr}\mathbf{F}_N\right|\frac{\boldsymbol{\omega}}{|\boldsymbol{\omega}|} & \text{for } \boldsymbol{\omega} \neq 0 \end{cases} \tag{4.19}$$

Note the similarity between the above equation and the expressions for the Coulomb friction force, Equation 4.17. Indeed, where the magnitude of the friction force was governed by the coefficient of friction f, that of the rolling resistance torque is governed by the coefficient of rolling resistance C_{rr}. Furthermore, the rolling resistance torque, too, displays both a static and a dynamic behaviour relating to whether or not the pod is stationary. The particular C_{rr} value that will be chosen for our simulations is discussed further on. In addition to this torque, rolling resistance also exerts a force on the center of mass of the rolling object, as expressed by [16]:

$$\mathbf{F}_{rr} = \begin{cases} 0 & \text{for } \mathbf{v} = 0 \text{ and } \dot{\mathbf{v}} = 0 \\ -\min\left(\left|m\dot{\mathbf{v}}\right|, \frac{mr}{\bar{I}}\left(\mathbf{u}_r \times \mathbf{L}_{rr}\right)\cdot\frac{\dot{\mathbf{v}}}{|\dot{\mathbf{v}}|}\right)\frac{\dot{\mathbf{v}}}{|\dot{\mathbf{v}}|} & \text{for } \mathbf{v} = 0 \text{ and } \dot{\mathbf{v}} \neq 0 \\ -\frac{mr}{\bar{I}}\left(\left(\mathbf{u}_r \times \mathbf{L}_{rr}\right)\cdot\frac{\mathbf{v}}{|\mathbf{v}|}\right)\frac{\mathbf{v}}{|\mathbf{v}|} & \text{for } \mathbf{v} \neq 0 \end{cases} \tag{4.20}$$

This force serves to maintain the pod's existing balance between velocity and rotation. Indeed, if the pod is rolling without slip, this synchronization will be preserved after application of the rolling resistance force and torque. Without the inclusion of the force $\mathbf{F}_{rr}$, there would exist a coupling between the Coulomb friction and the rolling resistance. By modelling the force as done here, one avoid this coupling and may study the effects of the two contact effects independently. The geometry involved in the computation of the rolling resistance force and torque are shown in Figure 4.7, where again the simplified, two-dimensional case is shown. This concludes our discussion of the three interactions present between a lander and the asteroid surface. Each of these interactions produces a distinctly different effect on the contact motion of a lander: the normal force enforces the condition of non-penetration that prevents the lander from moving through the asteroid surface. The Coulomb friction force and related torque force the pod's velocity and rotation into a no-slip synchronization. Finally, the rolling resistance torque and related force serve to reduce the velocity of the pod whilst maintaining its slip state.

4.4.4 Regularization

We must make one final remark regarding the Coulomb friction and rolling resistance force and torques. Following their previous definitions, these are discontinuous at $\mathbf{v}_H = 0$ and $\boldsymbol{\omega} = 0$, respectively. This is problematic for a numerical integrator as it will create velocity oscillations that can increase the system's energy, or fail to detect a lander pod is coming to a full stop. One solution technique, which is used in many contact dynamics codes, is the *regularization* of these forces and torques, which is the process of making their expressions continuous at zero. The regularized Coulomb friction force is given by [34]:

$$\mathbf{F}_f = \begin{cases} f\,|\mathbf{F}_N|\,\frac{\mathbf{v}_H}{|\mathbf{v}_{min}|} & \text{for} \quad |\mathbf{v}_H| < |\mathbf{v}_{min}| \\ f\,|\mathbf{F}_N| & \text{for} \quad |\mathbf{v}_H| \geq |\mathbf{v}_{min}| \end{cases} \tag{4.21}$$

An illustration of this function's behavior is shown in Figure 4.8. It can be seen that the initial expression behaves as a dirac function at $\mathbf{v}_H = 0$, whereas the regularized expression is continuous at first order. If now the value of $\mathbf{v}_{min}$ is set close to zero, the effect on the sphere's motion will be negligible over the span of an entire simulation, yet at the same time the numerical instability is resolved [34]. A similar approach is applied to regularize the rolling resistance; both will be applied in our simulations.

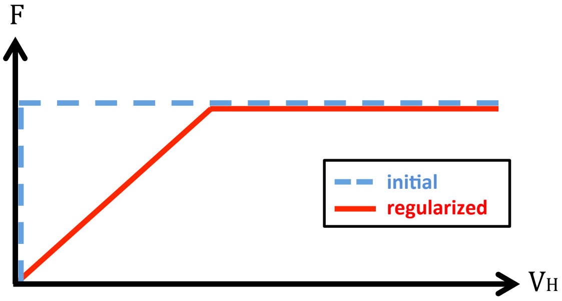

Figure 4.8: Illustration of regularization.

4.5 Collisions

The two previous sections have discussed the modelling approaches applied in representing gravitational and contact interactions. In addition to these two modes of continuous motion, the current section focuses on the intermediate case of collisions/impacts with the asteroid surface, which effectively link two separate orbital arcs.

Collisions are handled through the instantaneous transfer of impulses, which change the velocity and rotation of the lander pod over an infinitesimally small amount of time. The main impulse acts on the pod's normal velocity relative to the surface it is colliding with. The magnitude of this impulse is determined by the coefficient of restitution e, which relates the inbound normal velocity $V_{0\perp}$ to the outbound normal velocity $V_{1\perp}$ through [37]:

$$e = \frac{V_{1\perp}}{V_{0\perp}} \tag{4.22}$$

The magnitude of the coefficient of restitution expresses the elasticity of the collision and has values in the range $0 \leq e \leq 1$. The case $e = 0$ corresponds to a collision which dissipates all normal velocity, while $e = 1$ represents a perfectly elastic collision [38]. The value of e that will be used in the simulations of this research will be discussed further on. The normal velocity impulse resulting from a collision may be computed using [34]:

$$\mathbf{J}_{F_n} = \mathbf{V}_{1\perp} - \mathbf{V}_{0\perp} = -m(1+e)\mathbf{V}_{0\perp} \tag{4.23}$$

Analogously, the force and torque impulses generated by the Coulomb friction force during the instantaneous collision are given by respectively [34]:

$$\mathbf{J}_{F_f} = \begin{cases} 0 & \text{for } \mathbf{V}_{H\parallel} = 0 \\ -\min\left(\frac{\left|m\mathbf{V}_{H\parallel}\right|}{\left|\mathbf{u}_r \times \left(I_{3,3} + \frac{mr^2}{\bar{I}}\right)\left(\mathbf{u}_r \times \frac{\mathbf{V}_{H\parallel}}{|\mathbf{V}_{H\parallel}|}\right)\right|}, \left|\mathbf{J}_{F_N}\right|\right)\frac{\mathbf{V}_{H\parallel}}{|\mathbf{V}_{H\parallel}|} & \text{for } \mathbf{V}_{H\parallel} \neq 0 \end{cases} \tag{4.24}$$

$$\mathbf{J}_{L_f} = r\mathbf{u}_r \times \mathbf{J}_{F_f} \tag{4.25}$$

Finally, also rolling resistance produces a torque and force impulse during a collision; these are given by respectively 4.26 and 4.27 [16]:

$$\mathbf{J}_{L_{rr}} = \begin{cases} 0 & \text{for } \boldsymbol{\omega} = 0 \\ -\min\left(|\bar{I}\boldsymbol{\omega}|, |rC_{rr}\mathbf{J}_{F_N}|\right)\frac{\bar{I}\boldsymbol{\omega}}{|\bar{I}\boldsymbol{\omega}|} & \text{for } \boldsymbol{\omega} \neq 0 \end{cases} \tag{4.26}$$

$$\mathbf{J}_{F_{rr}} = \begin{cases} 0 & \text{for } \boldsymbol{V}_{\parallel} = 0 \\ -\min\left(|m\mathbf{V}_{\parallel}|, \frac{mr}{\bar{I}}\left((\mathbf{u}_r \times \mathbf{J}_{L_{rr}}) \cdot \frac{\mathbf{V}_{\parallel}}{|\mathbf{V}_{\parallel}|}\right)\right)\frac{\mathbf{V}_{\parallel}}{|\mathbf{V}_{\parallel}|} & \text{for } \boldsymbol{V}_{\parallel} \neq 0 \end{cases} \tag{4.27}$$

We stress that the impulse equations shown do not depend on the derivatives of the velocity or rotation. This is to be expected, as impulses act over an infinitesimally small interval of time.

Infinite Collision Modelling

If the coefficient of restitution $e \neq 0$, then the outbound normal velocity after a bounce will only asymptotically approach, but never actually reach zero, following Equation 4.22. Implementing a collision this way would result in an infinite number of bounces occurring in a finite time, as shown in Figure 4.9. Although there will be a set time at which a bouncing pod transitions from free-flying to rolling contact, the integrator will never reach this as the time step will be forced to zero. This issue is analogous to Zeno's paradox of Achilles and the tortoise. One possible solution to this problem is to define a certain $V_{\perp\text{min}}$ close to, but larger than zero. When the pod's normal velocity becomes lower than this limit, it is set to zero and contact motion is started. However, when it is assumed that e is independent of the normal velocity, it is possible to solve for the effect of the infinity of bounces.

Applying Equation 4.22, we can express the normal velocity after the n-th bounce as $V_{n\perp} = e^n V_{0\perp}$. Using this expression, it is possible to substitute the infinite number of bounces with a single, virtual bounce which reaches the same final point and time as the infinite series of bounces. This requires modifying the incoming normal velocity to $V_{0\perp}$ to the virtual incoming velocity $V_{\infty\perp}$ [34]:

$$V_{\infty\perp} = \frac{e}{1-e} V_{0\perp} \tag{4.28}$$

Whenever a collision has been handled and the pod's normal velocity is found to be smaller than $V_{\perp\text{min}}$, the remaining infinite series of bounces with negligible $V_{\perp}$ is replaced by single bounce with $V_{\infty\perp}$, with contact motion starting at the end of this bounce. This principle is illustrated for clarity in Figure 4.9. If $V_{\perp\text{min}}$ is kept small enough[7], the effect of this strategy on the pod trajectory is negligible [34]. This approach will therefore be applied in the handling of collisions during the simulations of this research.

4.6 Rock Interaction

By including both collisions with the asteroid shape model and rolling resistance, our software is capable of capturing interactions between the lander and asteroid surface features that are either very large or very small. Indeed, the polyhedron model contains hills and craters, while rolling resistance effectively models the surface's granular structure. To achieve a complete representation, it finally is necessary to also include features of intermediate sizes, between

---

[7] On the order of a few mm/s.

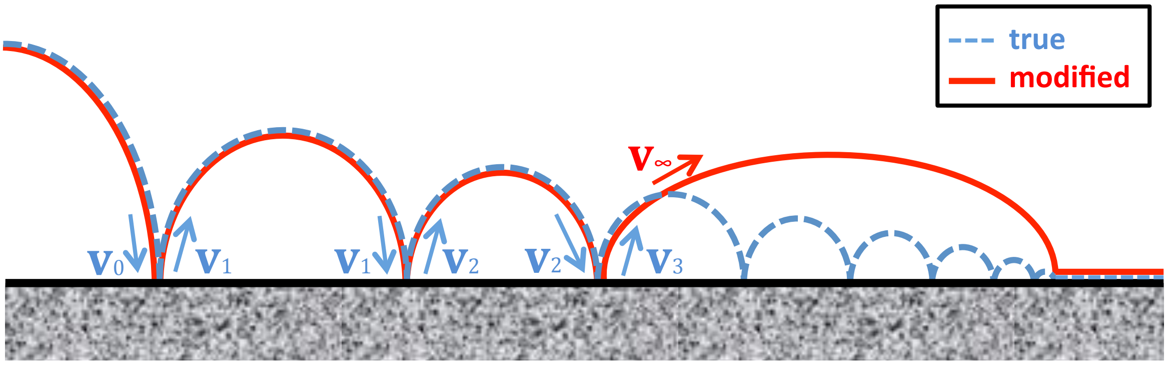

Figure 4.9: Illustration of infinite and virtual bounces.

roughly a few meters and a few centimeters. We denote these features as *rocks*.

A fully realistic modelling of the interactions between a lander and asteroid rocks would populate the polyhedron shape with rocks of different sizes at the proper densities that have been observed by spacecraft in the past (mostly Hayabusa [39]). However, doing so is algorithmically complicated and requires a thorough understanding of procedural topography generation. Instead, we have chosen to implement a much simpler stochastic model of the rock distributions, as taken from [16]. This model distinguishes between *impact* collisions and *rolling* collisions. The former are taken into account during impacts of the lander on the asteroid surface, as discussed in Section 4.5, and imposes a statistical variation on the normal surface direction used during computation of the impact. In this way, it is possible to represent how rocks on the asteroid surface effectively 'destroy' the planarity of the polyhedron facets. Secondly, rolling collisions are implemented from the same model using the mean free path of the lander. When the lander starts contact motion on the asteroid surface, the software determines the distance to be covered to the next rolling collision. Once the lander has covered this distance, the software uses the stochastic model to compute the impact point of the rock on the surface on the lander pod. The collision is then carried out; the pod may be flung into the air because of this collision.

The applied stochastic model is based on the rock distribution observed on the surface of asteroid 25143 Itokawa by the Hayabusa spacecraft [39] and captures the particular effect these rocks have on the collisions with the surface. In that study, the authors measured the mean horizontal dimension of all rocks and boulders on Itokawa's surface, and converted these results into a cumulative boulder size per unit surface area distribution. This distribution may be represented through a power law, for which case the power index is equal to 3.1 ± 0.1 for the entire surface of Itokawa, for boulder sizes between 5 m and 20 m in diameter. This power-law distribution is also shown in Figure 4.10. With both these types of collisions included, our asteroid model captures all interactions between the surface and the lander, and we may proceed to construct the final equations of motion that are propagated by the simulation software.

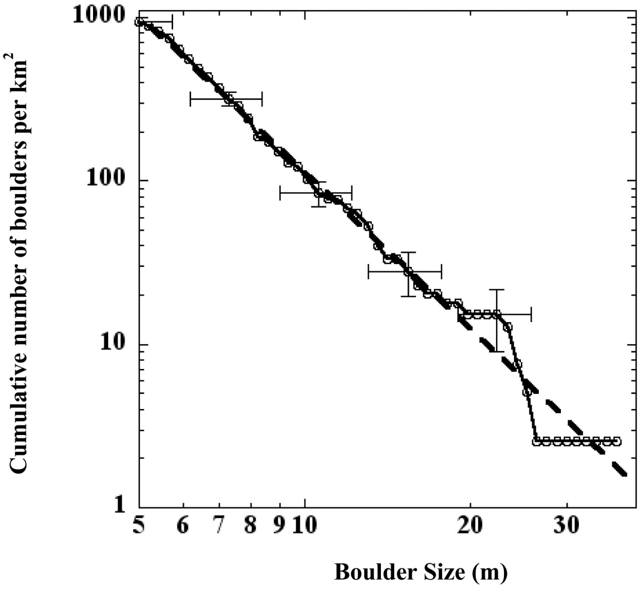

Figure 4.10: Cumulative boulder size distribution per unit area on the entire surface of Itokawa [39].

4.7 Equations of Motion

By combining the forces and torques listed in the previous sections, we are able to fully simulate the motion of a lander in the asteroid neighborhood, by propagating the respective equations of motion. We now present these equations of motion for simulations in both unitary and binary asteroid systems, and for all modes of propagation that were shown earlier in Table 4.1.

4.7.1 Unitary Systems

We distinguish between propagation of the target unitary asteroid (state variables 14:26) and of the lander spacecraft (state variables 1:13).

Target

As mentioned in Table 4.1, the position and velocity of the target unitary asteroid body is *always* propagated in the SIF. These values are of importance when additional perturbations such as solar-radiation pressure or third-body attraction need to be included. However, the magnitude of these forces is negligible for the duration of lander deployment. As such, propagating the asteroid's position and velocity would be a computational waste and is therefore not performed, meaning that $\mathbf{R}_{\text{B1,SIF}} = \mathbf{V}_{\text{B1,SIF}} = \mathbf{0}$. It is noted that place-holders for this position and velocity have been added to the state, as the inclusion of the aforementioned forces is not unforeseeable in the future of this research. We do propagate the orientation of the unitary asteroid body, as it rotates with respect to the TIF. This rotation is expressed through quaternions, which are propagated using:

$$\dot{\mathbf{q}} = \frac{1}{2}\mathbf{B}\begin{bmatrix} 0 \\ \boldsymbol{\omega} \end{bmatrix} = \frac{1}{2}\begin{bmatrix} q_1 & -q_2 & -q_3 & -q_4 \\ q_2 & q_1 & -q_4 & q_3 \\ q_3 & q_4 & q_1 & -q_2 \\ q_4 & -q_3 & q_2 & q_1 \end{bmatrix}\begin{bmatrix} 0 \\ \omega_x \\ \omega_y \\ \omega_z \end{bmatrix} = \frac{1}{2}\begin{bmatrix} -q_2 & -q_3 & -q_4 \\ q_1 & -q_4 & q_3 \\ q_4 & q_1 & -q_2 \\ -q_3 & q_2 & q_1 \end{bmatrix}\begin{bmatrix} \omega_x \\ \omega_y \\ \omega_z \end{bmatrix} \tag{4.29}$$

Finally, we assume that the target asteroid body is in uniform rotation; or $\dot{\boldsymbol{\omega}}_{\text{B1,RB1F}} = \mathbf{0}$.

Spacecraft (Flying)

The situation is slightly more complicated for the spacecraft/lander, we can see from Table 4.1 that its state is propagated in either TIF or RB1F, depending on the selected mode of propagation. When the spacecraft state is propagated using mode *Uni 0* in the TIF, its position and velocity are propagated using:

$$\dot{\mathbf{R}}_{\text{SC,TIF}} = \mathbf{V}_{\text{SC,TIF}} \tag{4.30}$$

$$\dot{\mathbf{V}}_{\text{SC,TIF}} = \mathbf{C}_{\text{B1,TIF}} \cdot \left[\frac{\delta U\left(\mathbf{C}^T_{\text{B1,TIF}} \cdot \mathbf{R}_{\text{SC,TIF}}\right)}{\delta \mathbf{R}_{\text{SC,TIF}}}\right] \tag{4.31}$$

In the latter equation, $\mathbf{C}_{\text{B1,TIF}}$ is the Direction Cosine Matrix (DCM) expressing the orientation of body B1 relative to the TIF, which can be computed from its quaternions using:

$$\mathbf{C}[\mathbf{q}] = \begin{bmatrix} q_1^2 + q_2^2 - q_3^2 - q_4^2 & 2(q_2q_3 + q_1q_4) & 2(q_2q_4 - q_1q_3) \\ 2(q_2q_3 - q_1q_4) & q_1^2 - q_2^2 + q_3^2 - q_4^2 & 2(q_3q_4 + q_1q_2) \\ 2(q_2q_4 + q_1q_3) & 2(q_3q_4 - q_1q_2) & q_1^2 - q_2^2 - q_3^2 + q_4^2 \end{bmatrix} \tag{4.32}$$

The part of Equation 4.31 between brackets expresses the gravitational acceleration of the spacecraft due to the presence of the asteroid body B1, evaluated using the constant density polyhedron at position $\mathbf{C}^T_{\text{B1,TIF}} \cdot \mathbf{R}_{\text{SC,TIF}}$, which is the spacecraft position in the RB1F. The orientation $\mathbf{q}_{\text{SC,TIF}}$ of the spacecraft is propagated using Equation 4.29; the rotation $\boldsymbol{\omega}_{\text{SC,SCF}}$ is invariable in the TIF when the spacecraft is not in contact with the asteroid surface (this case will be discussed further on).

When instead using mode *Uni 1*, the spacecraft state is propagated in the RB1F[8]. As this is a rotating and therefore non-inertial reference frame, we must include the proper virtual accelerations in our equations of motion. The spacecraft position and velocity are then propagated using:

$$\dot{\mathbf{R}}_{\text{SC,RB1F}} = \mathbf{V}_{\text{SC,RB1F}} \tag{4.33}$$

$$\dot{\mathbf{V}}_{\text{SC,RB1F}} = \left[\frac{\delta U\left(\mathbf{R}_{\text{SC,RB1F}}\right)}{\delta \mathbf{R}_{\text{SC,RB1F}}}\right] - \boldsymbol{\omega}^2_{\text{B1,RB1F}} \times \mathbf{R}_{\text{SC,RB1F}} - 2\boldsymbol{\omega}_{\text{B1,RB1F}} \times \mathbf{V}_{\text{SC,RB1F}} \tag{4.34}$$

In the latter equation, $\boldsymbol{\omega}^2_{\text{B1,RB1F}} \times \mathbf{R}_{\text{SC,RB1F}}$ is the centrifugal acceleration and $2\boldsymbol{\omega}_{\text{B1,RB1F}} \times \mathbf{V}_{\text{SC,RB1F}}$ is the Coriolis acceleration resulting from our use of the rotating RB1F. It is noted that this equation does not include the DCM that was used when propagating in *Uni 0*. This makes sense; since the motion of the spacecraft is propagated in the RB1F, we no longer need to carry out the transformation from TIF to RB1F. The orientation of the spacecraft is again propagated using Equation 4.29.

Spacecraft (Contact)

The equations of motion given above are valid under the assumption that no interaction with the asteroid surface occurs. When the spacecraft/lander does indeed perform contact motion on the asteroid (possible only in *Uni 1*), we must include the surface forces and torques discussed in Section 4.4. The spacecraft velocity will be propagated as:

$$\dot{\mathbf{V}}_{\text{SC,RB1F}} = \mathbf{a}_{e,\text{RB1F}} + \frac{1}{m}\left(\mathbf{N}_{\text{RB1F}} + \mathbf{F}_{f,\text{RB1F}} + \mathbf{F}_{rr,\text{RB1F}}\right) \tag{4.35}$$

Additionally, the rotation of the spacecraft is propagated using:

$$\dot{\boldsymbol{\omega}}_{\text{SC,SCF}} = \frac{1}{I_{\text{SCF}}}\left(\mathbf{L}_{f,\text{SCF}} + \mathbf{L}_{rr,\text{SCF}}\right) \tag{4.36}$$

In these equations, $\mathbf{N}$ is the normal force, and the subscripts f and rr refer to respectively friction and rolling resistance, following their definitions from Section 4.4. Furthermore, $\mathbf{a}_e$ is the external acceleration produced by gravity. As an overview, Table 4.2 lists the respective equations used to propagate the state for the mentioned propagation modes in the unitary case.

4.7.2 Binary System

We separate between propagation of the two asteroid bodies of the target binary system (state variables 14:45) and of the lander spacecraft (state variables 1:13).

---

[8] While we could also propagate the spacecraft state in the TIF, and perform the proper coordinate transforms into the RB1F, we have chosen for consistency to propagate the state in the frames that we are interested in.

Table 4.2: Overview of equations of motion for unitary systems.

		Uni 0	Uni 1	
			Orbiting	Contact
S/C	$\dot{\mathbf{R}}$	Eq. 4.30	Eq. 4.33	Eq. 4.33
	$\dot{\mathbf{V}}$	Eq. 4.31	Eq. 4.34	Eq. 4.35
	$\dot{\mathbf{q}}$	Eq. 4.29	Eq. 4.29	Eq. 4.29
	$\dot{\boldsymbol{\omega}}$	$\mathbf{0}$	$\mathbf{0}$	Eq. 4.36
B1	$\dot{\mathbf{R}}$	$\mathbf{0}$	$\mathbf{0}$	$\mathbf{0}$
	$\dot{\mathbf{V}}$	$\mathbf{0}$	$\mathbf{0}$	$\mathbf{0}$
	$\dot{\mathbf{q}}$	Eq. 4.29	Eq. 4.29	Eq. 4.29
	$\dot{\boldsymbol{\omega}}$	$\mathbf{0}$	$\mathbf{0}$	$\mathbf{0}$

Target

Following the same reasoning made in the above, the motion of the target binary asteroid system as a whole about the Sun is not taken into account at this point, therefore $\dot{\mathbf{R}}_{\mathrm{T}} = \dot{\mathbf{V}}_{\mathrm{T}} = \mathbf{0}$. We do however propagate the motion of the two asteroid bodies relative to their mutual center of mass. As shown in Table 4.1, this propagation is carried out in the TIF, regardless of the selected propagation mode. We assume this motion may be modelled using point-mass attraction, leading to the following equations of motion:

$$\begin{cases} \dot{\mathbf{R}}_{\mathrm{B1}} = \mathbf{V}_{\mathrm{B1}} \\ \dot{\mathbf{R}}_{\mathrm{B2}} = \mathbf{V}_{\mathrm{B2}} \end{cases} \tag{4.37}$$

$$\begin{cases} \dot{\mathbf{V}}_{\mathrm{B1}} = -\frac{\mu_{\mathrm{B2}}}{R_{12}^3}\mathbf{R}_{12} \\ \dot{\mathbf{V}}_{\mathrm{B2}} = -\frac{\mu_{\mathrm{B1}}}{R_{21}^3}\mathbf{R}_{21} \end{cases} \tag{4.38}$$

In these equations, $\mu_i = GM_i$ is the gravitational parameter of body i and $\mathbf{R}_{ij}$ is the position vector from body i to body j. The orientation of both bodies is propagated using again Equation 4.29. Finally, we assume that their rotation is torque-free, and therefore that $\dot{\boldsymbol{\omega}}_{\mathrm{B1}} = \dot{\boldsymbol{\omega}}_{\mathrm{B2}} = \mathbf{0}$.

Spacecraft (Orbiting)

The equations of motions for a spacecraft/lander in the binary case differ depending on the selected mode of propagation, as was also the case for unitary systems. When selecting *Bin 0*, the motion of the spacecraft is propagated in the TIF as:

$$\dot{\mathbf{R}}_{\mathrm{SC,TIF}} = \dot{\mathbf{V}}_{\mathrm{SC,TIF}} \tag{4.39}$$

$$\dot{\mathbf{V}}_{\mathrm{SC,TIF}} = \mathbf{C}_{\mathrm{TIF,B1}} \cdot \left[\frac{\delta U\left(\mathbf{R}_{\mathrm{SC,RB1F}}\right)}{\mathbf{R}_{\mathrm{SC,RB1F}}}\right] + \mathbf{C}_{\mathrm{TIF,B2}} \cdot \left[\frac{\delta U\left(\mathbf{R}_{\mathrm{SC,RB2F}}\right)}{\mathbf{R}_{\mathrm{SC,RB2F}}}\right] \tag{4.40}$$

In the latter equation, $\mathbf{C}_{\mathrm{TIF,Bi}}$ are the transformation matrices expressing the transformation from the asteroid body-frames to the inertial frame, as given by Equation 4.32. Furthermore, the terms between brackets express the gravitational attraction of the two asteroid bodies, computed using their respective polyhedron model in the respective body-fixed frames RB1F and RB2F,as:

$$\begin{cases} \mathbf{R}_{\mathrm{SC,RB1F}} = \mathbf{C}_{\mathrm{B1,TIF}} \cdot \left(\mathbf{R}_{\mathrm{SC,TIF}} - \mathbf{R}_{\mathrm{B1,TIF}}\right) \\ \mathbf{R}_{\mathrm{SC,RB2F}} = \mathbf{C}_{\mathrm{B2,TIF}} \cdot \left(\mathbf{R}_{\mathrm{SC,TIF}} - \mathbf{R}_{\mathrm{B2,TIF}}\right) \end{cases} \tag{4.41}$$

The spacecraft orientation is again propagated using Equation 4.29, and its rotation is constant such that $\dot{\boldsymbol{\omega}}_{\mathrm{SC,SCF}} = \mathbf{0}$.

When using mode *Bin 1* and propagating the spacecraft in the RB1F, we must again include the proper virtual accelerations. In this case, the spacecraft motion is propagated as:

$$\dot{\mathbf{R}}_{\mathrm{SC,RB1F}} = \dot{\mathbf{V}}_{\mathrm{SC,RB1F}} \tag{4.42}$$

$$\begin{aligned} \dot{\mathbf{V}}_{\mathrm{SC,RB1F}} = \frac{\delta U(\mathbf{R}_{\mathrm{SC,RB1F}})}{\delta \mathbf{R}_{\mathrm{SC,RB1F}}} + \mathbf{C}_{\mathrm{B1,TIF}} \cdot \left(\mathbf{C}_{\mathrm{TIF,B2}} \cdot \frac{\delta U(\mathbf{R}_{\mathrm{SC,RB2F}})}{\delta \mathbf{R}_{SC,RB2F}}\right) \\ - \boldsymbol{\omega}^2_{\mathrm{B1,RB1F}} \times \mathbf{R}_{\mathrm{SC,RB1F}} - 2\boldsymbol{\omega}_{\mathrm{B1,RB1F}} \times \mathbf{V}_{\mathrm{SC,RB1F}} \end{aligned} \tag{4.43}$$

In this equation, the position $\mathbf{R}_{\mathrm{SC,RB2F}}$ is given by:

$$\mathbf{R}_{\mathrm{SC,RB2F}} = \mathbf{C}_{\mathrm{B2,TIF}} \cdot \left[\mathbf{C}_{\mathrm{TIF,B1}} \cdot \mathbf{R}_{\mathrm{SC,RB1F}} + \mathbf{R}_{\mathrm{B1,TIF}} - \mathbf{R}_{\mathrm{B2,TIF}}\right] \tag{4.44}$$

The orientation of the spacecraft is again propagated using Equation 4.29; its rotation requires the inclusion of additional terms due to the reference frame selection and is propagated as:

$$\dot{\boldsymbol{\omega}}_{\mathrm{SC,SCF}} = -\left(\mathbf{C}_{\mathrm{SC,TIF}} \cdot \boldsymbol{\omega}_{\mathrm{B1,SIF}}\right) \times \boldsymbol{\omega}_{\mathrm{SC,SCF}} \tag{4.45}$$

Finally, when propagating in mode *Bin 2*, the equations change to:

$$\dot{\mathbf{R}}_{\mathrm{SC,RB2F}} = \dot{\mathbf{V}}_{\mathrm{SC,RB2F}} \tag{4.46}$$

$$\begin{aligned} \dot{\mathbf{V}}_{\mathrm{SC,RB2F}} = \frac{\delta U(\mathbf{R}_{\mathrm{SC,RB2F}})}{\delta \mathbf{R}_{\mathrm{SC,RB2F}}} + \mathbf{C}_{\mathrm{B2,TIF}} \cdot \left(\mathbf{C}_{\mathrm{TIF,B1}} \cdot \frac{\delta U(\mathbf{R}_{\mathrm{SC,RB1F}})}{\delta \mathbf{R}_{SC,RB1F}}\right) \\ - \boldsymbol{\omega}^2_{\mathrm{B2,RB2F}} \times \mathbf{R}_{\mathrm{SC,RB2F}} - 2\boldsymbol{\omega}_{\mathrm{B2,RB2F}} \times \mathbf{V}_{\mathrm{SC,RB2F}} \end{aligned} \tag{4.47}$$

$$\dot{\boldsymbol{\omega}}_{\mathrm{SC,SCF}} = -\left(\mathbf{C}_{\mathrm{SC,TIF}} \cdot \boldsymbol{\omega}_{\mathrm{B2,SIF}}\right) \times \boldsymbol{\omega}_{\mathrm{SC,SCF}} \tag{4.48}$$

In these equations, the position $\mathbf{R}_{\mathrm{SC,RB1F}}$ is given by:

$$\mathbf{R}_{\mathrm{SC,RB1F}} = \mathbf{C}_{\mathrm{B1,TIF}} \cdot \left[\mathbf{C}_{\mathrm{TIF,B2}} \cdot \mathbf{R}_{\mathrm{SC,RB2F}} + \mathbf{R}_{\mathrm{B2,TIF}} - \mathbf{R}_{\mathrm{B1,TIF}}\right] \tag{4.49}$$

Spacecraft (Contact)

Finally, when the spacecraft/lander performs contact motion on either of the asteroid bodies (possible only in modes *Bin 1* and *Bin 2*), we must again include the surface forces and torques, as given by Equations 4.35 and 4.36. In this case, the external acceleration $\mathbf{a}_E$ is given by either Equation 4.43 or 4.47. As a final overview, Table 4.3 lists the respective equations used to propagate the state for the mentioned propagation modes in the binary case.

Table 4.3: Overview of equations of motion for binary systems.

		Bin 0	Bin 1		Bin 2	
			Orbiting	Contact	Orbiting	Contact
S/C	$\dot{\mathbf{R}}$	Eq. 4.39	Eq. 4.42	Eq. 4.42	Eq. 4.46	Eq. 4.46
	$\dot{\mathbf{V}}$	Eq. 4.40	Eq. 4.43	Eq. 4.35	Eq. 4.47	Eq. 4.35
	$\dot{\mathbf{q}}$	Eq. 4.29	Eq. 4.29	Eq. 4.29	Eq. 4.29	Eq. 4.29
	$\dot{\boldsymbol{\omega}}$	$\mathbf{0}$	Eq. 4.45	Eq. 4.36	Eq. 4.48	Eq. 4.36
B1	$\dot{\mathbf{R}}$	Eq. 4.37	Eq. 4.37	Eq. 4.37	Eq. 4.37	Eq. 4.37
	$\dot{\mathbf{V}}$	Eq. 4.38	Eq. 4.38	Eq. 4.38	Eq. 4.38	Eq. 4.38
	$\dot{\mathbf{q}}$	Eq. 4.29	Eq. 4.29	Eq. 4.29	Eq. 4.29	Eq. 4.29
	$\dot{\boldsymbol{\omega}}$	$\mathbf{0}$	$\mathbf{0}$	$\mathbf{0}$	$\mathbf{0}$	$\mathbf{0}$
B2	$\dot{\mathbf{R}}$	Eq. 4.37	Eq. 4.37	Eq. 4.37	Eq. 4.37	Eq. 4.37
	$\dot{\mathbf{V}}$	Eq. 4.38	Eq. 4.38	Eq. 4.38	Eq. 4.38	Eq. 4.38
	$\dot{\mathbf{q}}$	Eq. 4.29	Eq. 4.29	Eq. 4.29	Eq. 4.29	Eq. 4.29
	$\dot{\boldsymbol{\omega}}$	$\mathbf{0}$	$\mathbf{0}$	$\mathbf{0}$	$\mathbf{0}$	$\mathbf{0}$
T	$\dot{\mathbf{R}}$	$\mathbf{0}$	$\mathbf{0}$	$\mathbf{0}$	$\mathbf{0}$	$\mathbf{0}$
	$\dot{\mathbf{V}}$	$\mathbf{0}$	$\mathbf{0}$	$\mathbf{0}$	$\mathbf{0}$	$\mathbf{0}$

Chapter 5

Geometry

The polyhedron model used for the shape and gravity modelling of asteroids in our software is capable of capturing complex shapes, yet remains in essence a geometrically simple model consisting only of a collection of tetrahedra. This enables us to apply a number of geometrical principles that assist in constructing and structuring the polyhedron model to our specific needs. These are the focus of the current chapter. We first discuss our method for computing outward-pointing normals in Section 5.1, followed by the theory used to perform distance computation relative to an arbitrary polyhedron in Section 5.2. Finally, we present a technique for generating an asteroid atlas, which breaks down a large polyhedron into smaller, more tractable local worlds in Section 5.3.

5.1 Normal Construction

As mentioned in Section 4.3, one outward-pointing normal can be defined for each facet, edge and vertex; these normals are used in the detection of collisions between a lander and the polyhedral asteroid model. The basic computation of the normal to a plane is simple: given two non-parallel unit vectors $\hat{\mathbf{u}}$ and $\hat{\mathbf{v}}$ that lie in some plane, the normal vector to that plane can be computed by taking the cross product of these unit vectors, as [40]:

$$\mathbf{N} = \hat{\mathbf{u}} \times \hat{\mathbf{v}} \tag{5.1}$$

For the case of a triangular facet consisting of points $\mathbf{P}_1$, $\mathbf{P}_2$ and $\mathbf{P}_3$, we simply use two of the unit edge vectors of that facet as $\hat{\mathbf{u}}$ and $\hat{\mathbf{v}}$, see Figure 5.1, and compute the facet normal by applying Equation 5.1. However, collision detection requires the normals of the asteroid model to be locally pointing *outwards* relative to the asteroid surface. Unfortunately, the direction of a normal computed by Equation 5.1 is dependent on the orientation of $\mathbf{u}$ and $\mathbf{v}$ and not known *a-priori* [40].

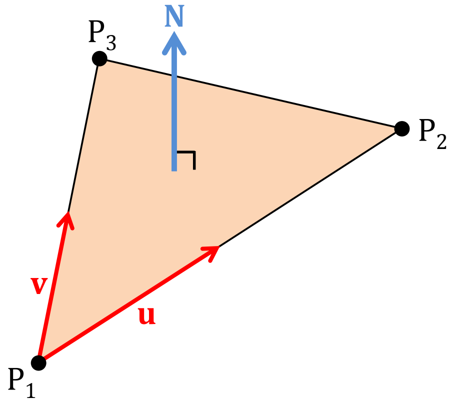

Figure 5.1: Geometry of a facet and its normal.

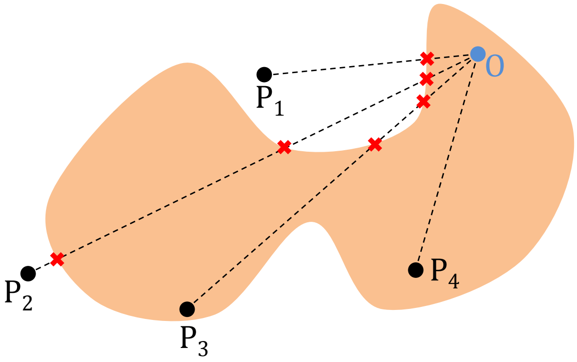

Figure 5.2: Crossing-number algorithm.

The direction of a given normal can be determined by making use of the *crossing-number algorithm* [36]. The working principle of this algorithm is as follows: given that some point $\mathbf{O}$ is known to be located inside a closed volume, it is possible to determine whether a second point $\mathbf{P}$ lies inside or outside that same volume, by counting the number of crossings between the ray $\mathbf{OP}$ and the boundary of that volume. If the number of crossings is *odd*, point $\mathbf{P}$ lies *outside* the volume; if it is *even*[1], $\mathbf{P}$ lies *inside* the volume [36]. This principle is illustrated in Figure 5.2, where point $\mathbf{O}$ is indeed located inside the arbitrary volume. The rays that connect points $\mathbf{P}_1$ through $\mathbf{P}_4$ with point $\mathbf{O}$ are traced, and their intersections with the volume boundary marked with red crosses. Rays $\mathbf{OP}_1$ and $\mathbf{OP}_2$ cross the boundary an odd number of times, points $\mathbf{P}_1$ and $\mathbf{P}_2$ are therefore located *outside* the volume. On the other hand, rays $\mathbf{OP}_3$ and $\mathbf{OP}_4$ cross the boundary an even number of times, points $\mathbf{P}_3$ and $\mathbf{P}_4$ are therefore located *inside* the volume.

If point $\mathbf{P}$ is the midpoint of some facet $\mathcal{F}$, we can therefore determine the correct direction of the normal of that facet by counting the intersections between the ray $\mathbf{OP}$ and all other facets $\mathcal{Q}$ of the asteroid model. In this, it is assumed that point $\mathbf{O} = [0, 0, 0]$ is the origin of the axis system with respect to which the asteroid polyhedron model is defined, and that this point lies *inside* the asteroid. The intersection between a ray $\mathbf{OP}$ and a facet $\mathcal{Q}$ can be computed using basic geometry, as detailed in the following and illustrated using Figure 5.3. In this figure, point $\mathbf{P}$ is the center of facet $\mathcal{P}$. The intersection $\mathbf{P}_k$ of ray $\mathbf{OP}$ with the *plane* of facet $\mathcal{Q}$ can be computed as [40]:

$$\mathbf{P}_k = t\mathbf{P} \quad \text{with} \quad t = \frac{\mathbf{Q}_n \cdot \mathbf{N}_Q}{\mathbf{P} \cdot \mathbf{N}_Q} \tag{5.2}$$

In this equation, $\mathbf{N}_Q$ is the normal[2] of facet $\mathcal{Q}$, and $\mathbf{Q}_n$ is any of the three vertices of facet $\mathcal{Q}$.

---

[1] The reader is reminded that zero is an even number.

[2] The direction of $\mathbf{N}_Q$ does not matter for this computation.

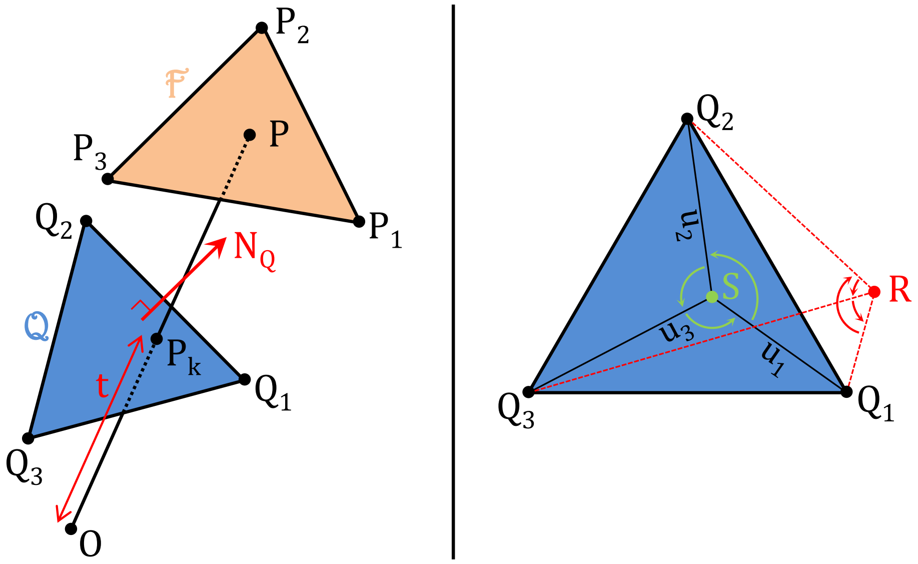

Figure 5.3: Geometry of ray-facet intersection.

If $0 < t < 1$, the intersection $\mathbf{P}_k$ lies between points $\mathbf{O}$ and $\mathbf{P}$ and is therefore a candidate for possible intersection between ray $\mathbf{OP}$ and facet $\mathcal{Q}$. To verify that point $\mathbf{P}_k$ indeed lies within facet $\mathcal{Q}$, and not outside as is the case for point $\mathbf{R}$, we must perform an additional test. If $\mathbf{u}_i$ are the vectors connecting the vertices of facet $\mathcal{Q}$ with the intersection point $\mathbf{P}_k$, we compute three cross-products $\mathbf{v}_i$:

$$\begin{cases} \mathbf{v}_1 = \mathbf{u}_3 \times \mathbf{u}_1 \\ \mathbf{v}_2 = \mathbf{u}_1 \times \mathbf{u}_2 \\ \mathbf{v}_3 = \mathbf{u}_2 \times \mathbf{u}_3 \end{cases} \tag{5.3}$$

If point $\mathbf{P}_k$ does indeed lie *inside* facet $\mathcal{Q}$, the angles subtended by consecutive rotations over $\mathbf{u}_i$ will cover a total angle of 360°, as can be seen on the right side of Figure 5.3 for point $\mathbf{S}$. Considering on the other hand point $\mathbf{R}$, these angles add to a total of 0°. Point $\mathbf{R}$ therefore lies *outside* of facet $\mathcal{Q}$. This rule can be expressed geometrically through the computation of the dot products:

$$\begin{cases} a_1 = \mathbf{v}_1 \cdot \mathbf{v}_2 \\ a_2 = \mathbf{v}_2 \cdot \mathbf{v}_3 \end{cases} \tag{5.4}$$

If both a_1 and a_2 are positive, the rotations over successive $\mathbf{u}_i$ are performed in the same direction. Therefore, any point $\mathbf{P}_k$ for which both $a_1 > 0$ and $a_2 > 0$ lies inside facet $\mathcal{Q}$. Using this rule, it is possible to compute the number of facets which the ray $\mathbf{OP}$ intersects. By then applying the crossing-number rule, we can determine which side of each facet lies on the outside of the asteroid polyhedron model, and the respective outward-pointing normal directions.

As each edge is contained by two facets, we can compute the outward-pointing normal of an edge by taking the average of the normals of the two facets of which that edge is part. Analogously, the normal of a vertex is computed through the average of the normals of the edges that vertex is contained by.

5.2 Distance Computations

Once the outward-pointing normals have been computed using the strategy outlined above, it is possible to determine which point $\mathbf{H}$ along the asteroid surface is closest to some field-point $\mathbf{P}$. As this $\mathbf{H}$ may be located on either a facet, edge or vertex feature of the polyhedron model, it is necessary that we check the distance from $\mathbf{P}$ to all of the features in the considered world[3]. This section presents the geometry that is used in determining the distance between a given point and one of three surface features.

5.2.1 Distance to a Facet

Given a facet $\mathcal{F}$ consisting of vertices $\mathbf{P}_1$, $\mathbf{P}_2$ and $\mathbf{P}_3$ with an outward-pointing normal $\mathbf{N}$, the projection of a point $\mathbf{P}$ on the plane of facet $\mathcal{F}$ can be computed as:

$$\mathbf{H} = \mathbf{P} - d\mathbf{N} \text{ with } d = (\mathbf{P} - \mathbf{P}_1) \cdot \mathbf{N} \tag{5.5}$$

Given that the facet normal $\mathbf{N}$ is defined as outward-pointing, the computed distance d from $\mathbf{P}$ to $\mathbf{H}$ is the *signed* distance; if d is positive, point $\mathbf{P}$ is located *outside* the asteroid model. However, this distance computation is only valid if point $\mathbf{P}$ is located *above* facet $\mathcal{F}$. This statement is equivalent to requiring the projection $\mathbf{H}$ to be located inside facet $\mathcal{F}$. We can evaluate this criterion using the approach outlined in the previous section, by computing the cross products of Equation 5.3, where $\mathbf{u}_i$ are the vectors connecting the vertices $\mathbf{P}_i$ with the projection point $\mathbf{H}$. If the dot products a_1 and a_2 as given by Equation 5.4 are both positive, it is concluded that point $\mathbf{P}$ is indeed located *above* facet $\mathcal{F}$; the computed distance d is valid. If either or both of the dot products are negative, $\mathbf{P}$ is not located above $\mathcal{F}$; the distance is then set to $d = \text{NaN}$. The geometry of this point-to-facet distance is illustrated in Figure 5.4.

5.2.2 Distance to an Edge

To compute the distance of a point $\mathbf{P}$ to a given edge $\mathcal{E}$ consisting of vertices $\mathbf{P}_1$ and $\mathbf{P}_2$, we first determine the projection $\mathbf{H}$ of $\mathbf{P}$ onto $\mathcal{E}$ as:

---

[3] This can either be the entire asteroid model, or a local world as created by the atlas routine (see 5.3).

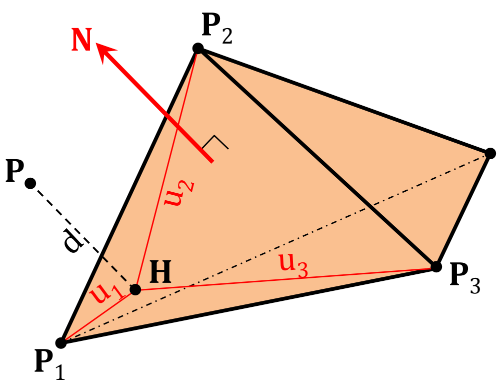

Figure 5.4: Point-to-facet distance geometry.

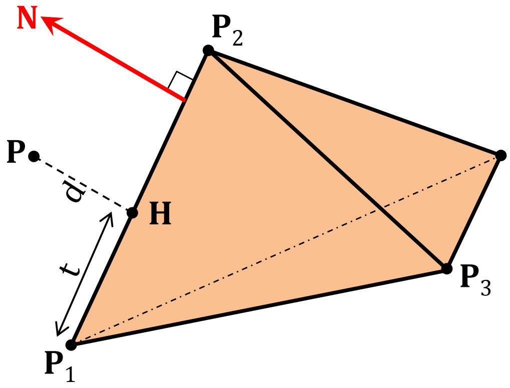

Figure 5.5: Point-to-edge distance geometry.

$$\mathbf{H} = t\mathbf{P}_1\mathbf{P}_2 + \mathbf{P}_1 \ \text{ with } \ t = \frac{\mathbf{P}_1\mathbf{P}_2 \cdot \mathbf{P}_1\mathbf{P}}{\mathbf{P}_1\mathbf{P}_2 \cdot \mathbf{P}_1\mathbf{P}_2} \tag{5.6}$$

If $0 < t < 1$, then $\mathbf{H}$ is located between points $\mathbf{P}_1$ and $\mathbf{P}_2$, and the distance of $\mathbf{P}$ to edge $\mathcal{E}$ can be computed as:

$$d = \sqrt{\mathbf{PH} \cdot \mathbf{PH}} \tag{5.7}$$

If, however, t lies outside of its accepted range, the distance is set to $d = \mathrm{NaN}$. We finally note that the distance d computed using Equation 5.7 is an *unsigned* distance, and we must check the position of point $\mathbf{P}$ with respect to the outward-pointing normal $\mathbf{N}$ of edge $\mathcal{E}$. Point $\mathbf{P}$ is located outside the asteroid model if and only if:

$$\mathbf{PH} \cdot \mathbf{N} < 0 \tag{5.8}$$

In words, this criterion states that the direction of the vector connecting $\mathbf{P}$ with its projection $\mathbf{H}$ onto the edge $\mathcal{E}$ must point in a direction opposite to that of the edge normal $\mathbf{N}$. The geometry of this point-to-edge distance is illustrated in Figure 5.5.

5.2.3 Distance to a Vertex

Finally, the distance between a point $\mathbf{P}$ and a vertex $\mathbf{P}_1$ can be computed as:

$$d = \sqrt{\mathbf{PP}_1 \cdot \mathbf{PP}_1} \tag{5.9}$$

Analogous to the point-to-edge distance, the distance expressed by Equation 5.9 is unsigned. Given the outward-pointing vertex normal $\mathbf{N}$, point $\mathbf{P}$ is located outside the asteroid model if and only if:

$$\mathbf{PP}_1 \cdot \mathbf{N} < 0 \tag{5.10}$$

The geometry of this point-to-vertex distance is illustrated in Figure 5.6. Using the given equations, it is possible to compute for any given point $\mathbf{P}$, the signed distance d to the closest point $\mathbf{H}$ along the asteroid surface. This finally allows for an effective method of detecting intersections between a lander and that surface, by checking when $(d - R)$ changes signs, where R is the radius of the lander pod.

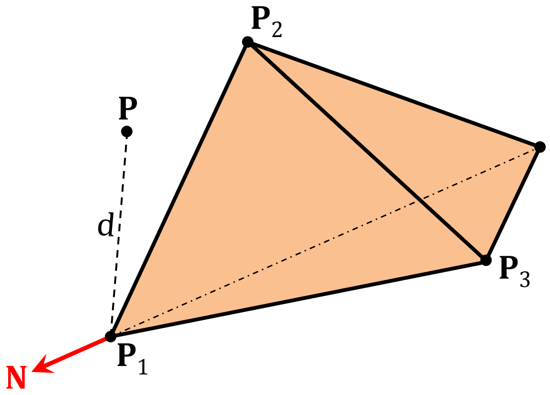

Figure 5.6: Point-to-vertex distance geometry.

5.3 Atlas

The impact detection method discussed in the above is highly effective and capable of handling collisions of a lander pod on a polyhedral asteroid model. However, if applied to the full asteroid model, we run into computation-time issues as high-resolution asteroid polyhedra frequently consist of over a hundred thousand surface features. Computing the distance to each of these features at every time step is extremely computationally intensive. Fortunately, a work-around to this issue can be constructed by applying additional geometry. It is easy to see that one need only check for collisions between the lander and the nearest features of the asteroid polyhedron, rather than the full model.

This principle is applied in the construction of an *atlas*, which consists of a number of much smaller *local* worlds that each cover a particular sector of the *global* world. During propagation of the lander's motion, the collision detection checks for collisions only with the features of this *local* world, thereby significantly reducing the time needed to perform a collision check. The construction of this asteroid atlas and the strategy for selecting the correct local world is discussed in the present section.

The construction of atlases is based on the application of spherical coordinates, in analogue to the latitude-longitude system applied on Earth to provide coordinates for a given point on the surface. The global asteroid model is subdivided into a number of local world 'cells' that each cover a user-specified range of latitudes and longitudes; nine such cells are shown in Figure 5.7. All facets of which at least one vertex is contained by some local world cell are included in that cell's respective local world, with an applied additional user-specified margin. This margin is shown as a dotted rectangle for the center world in Figure 5.7 and accounts for the size of the lander to prevent failure of collision detection in certain cases. The facets that are part of the center local world are colored for illustrative purposes in Figure 5.7.

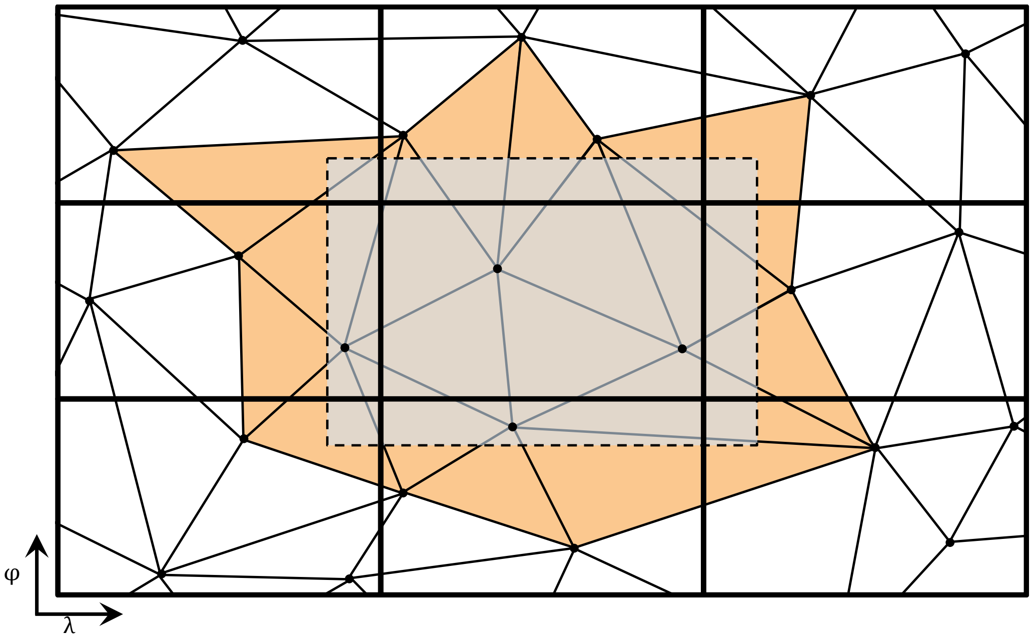

Figure 5.7: Atlas geometry.

Unfortunately, the application of the 'classical' latitude and longitude[4] for local world construction has some problems. All local worlds near the equator cover more or less the same area, but those near the poles are strongly distorted. This effect is perhaps clearest when reviewing Figure 5.8a and comparing the relative sizes of the squares near the equator to those close to the poles. We are therefore unable to use this classical atlas-division method near the poles. Fortunately, a relatively easy solution to this issue is provided through the construction of a secondary atlas that uses not latitude-longitude coordinates defined with respect to the equatorial plane, but rather with respect to the plane defined by the prime meridian. By combining the original *Z-atlas* and this secondary *X-atlas*, and having both span from latitude -45° to latitude 45° with an additional margin, we are able to cover the entire asteroidal sphere with a grid of local worlds that are roughly the same size, independent of their location. The coverage of both these atlases is shown on the terrestrial sphere in Figure 5.8 and on a projected map in Figure 5.9.

---

[4] The classical latitude and longitude are defined using the equatorial plane and prime meridian.

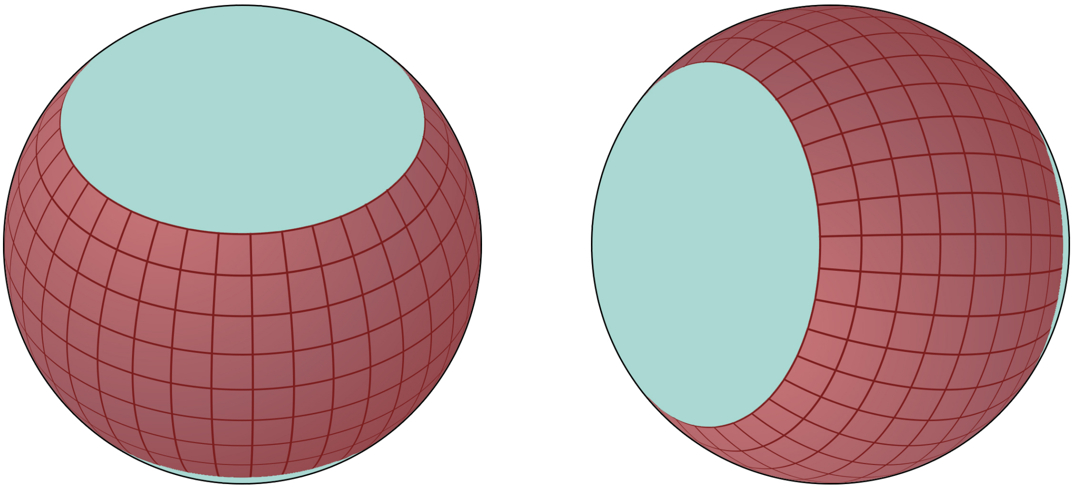

(a) Z-Atlas. **(b)** X-Atlas.

Figure 5.8: Illustration of applied atlas graticules.

During propagation of the lander motion, the algorithm will update the active local world at each time step, by computing the latitude and longitude of the lander at that time step and selecting the corresponding local world, by computing its latitude and longitude as:

$$\mathrm{Z}: \begin{cases} R_z = \sqrt{x^2 + y^2} \\ \phi_z = \arctan\left(z/R_z\right) \\ \lambda_z = \operatorname{mod}\left[\arctan\left(y/x\right), 2\pi\right] \end{cases} \qquad \mathrm{X}: \begin{cases} R_x = \sqrt{y^2 + z^2} \\ \phi_x = \arctan\left(x/R_x\right) \\ \lambda_x = \operatorname{mod}\left[\arctan\left(z/y\right), 2\pi\right] \end{cases} \tag{5.11}$$

An interesting observation can be made with respect to the selection of active local worlds during orbiting arcs of the lander pods, when a pod is far away from the asteroid. Indeed, it is possible for the algorithm to select an 'active' world that corresponds to the latitude-longitude of the lander, yet does not contain those asteroid surface features that are geometrically nearest to the lander; a direct result of the application of spherical coordinates on strongly non-spherical asteroid bodies. While this may seem problematic at first, it does not pose any issues to the detection of collisions as the correct world will eventually be selected as the pod approaches the surface. This is illustrated in Figure 5.10, where the initial world selection is off, but gets corrected as the pod approaches the asteroid.

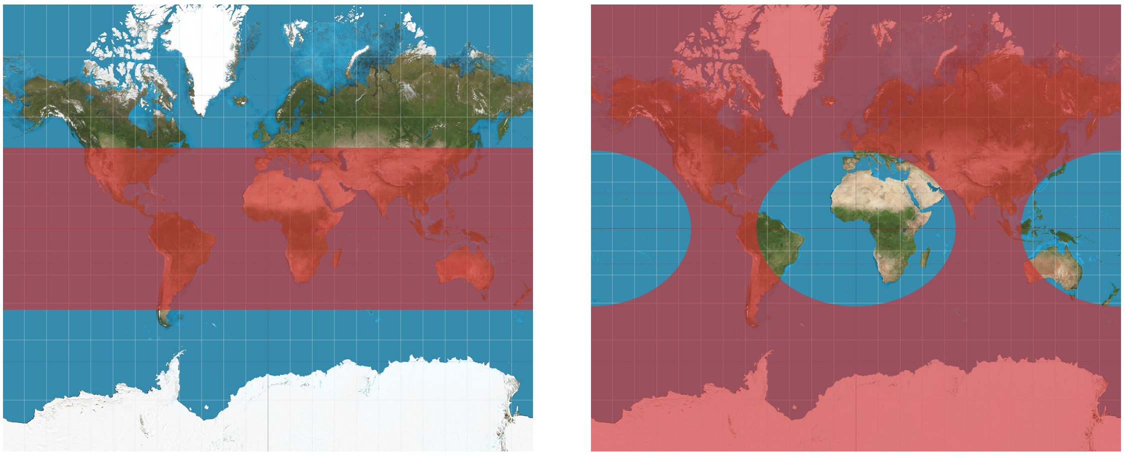

(a) Z-Atlas.

(b) X-Atlas.

Figure 5.9: Illustration of applied atlas coverages.

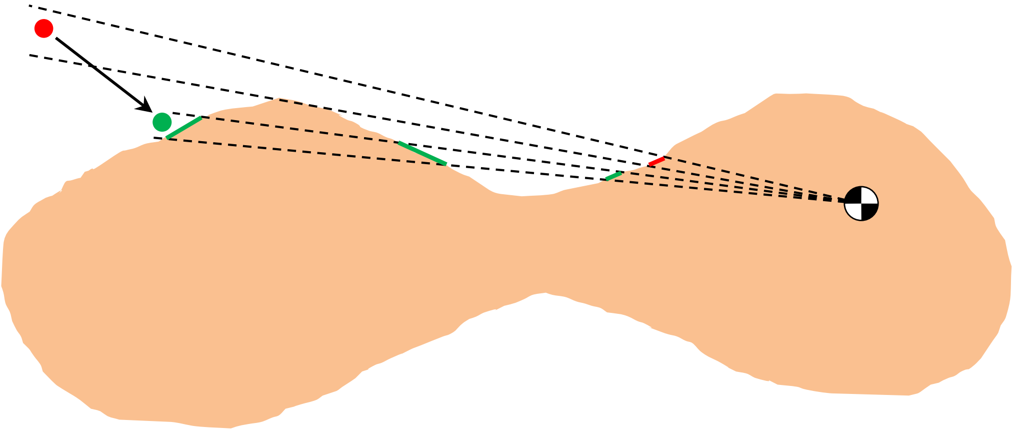

Figure 5.10: Local world selection.

Chapter 6

Propagator

THE MOTION OF a lander in orbit around and on the surface of an asteroid is the direct result of the gravitational and contact interactions between the asteroid and the lander. Unfortunately, no analytical solution of such motion exists due to the inherent complexity of the relevant equations of motion. We must therefore resort to numerical integration of the latter to be able to construct lander trajectories. The current chapter details the principles behind the numerical integration routine applied by our simulation software in Section 6.1, along with its time-step variability characteristics. In addition to simulating arcs of smooth lander motion, our integrator is also capable of detecting and handling *events*, which interrupt the continuity of the lander trajectories and are discussed in Section 6.2. Finally, the numerical implementation of all integrator modules is shown in a coherent structure in Section 6.3.

6.1 Integrator

The numerical integrator that is at the core of our software applies a Runge-Kutta (RK) method, named after the German mathematicians Carl Runge and Wilhem Kutta who originally developed the technique. This integration method was selected for its high accuracy at low computational cost. The RK methods are based on an application of the *Euler step*, which approximates the state vector $\dot{\mathbf{X}}$ of a system at some time $t_0 + h$ using a first-order Taylor expansion starting from the initial conditions $\dot{\mathbf{X}}_0 = \dot{\mathbf{X}}(t_0)$, as [41]:

$$\mathbf{X}(t_0 + h) \approx \mathbf{X}_0 + h\dot{\mathbf{X}}_0 \approx \mathbf{X}_0 + hf(t_0, \mathbf{X}_0) \approx \mathbf{X}_0 + h\boldsymbol{\phi} \tag{6.1}$$

In these equations, h is the step size and $\boldsymbol{\phi}$ is the *increment function*, which describes the variation of the differential equations that govern the system. Although a variety of RK methods exist, all of them share a common structure where, in an s-stage RK integrator, s function evaluations of the factor $\mathbf{k}_i$ are applied, following [41]:

$$\mathbf{k}_i = \begin{cases} \mathbf{f}(t_0 + c_1 h, \mathbf{X}_0) & \text{for } i = 1 \\ \mathbf{f}(t_0 + c_i h, \mathbf{X}_0 + h \sum_{j=1}^{i-1} a_{ij} \mathbf{k}_j) & \text{for } i = 2 : s \end{cases} \tag{6.2}$$

The $\mathbf{k}_i$ factors are applied to form the increment function $\boldsymbol{\phi}$, defined as [41]:

$$\boldsymbol{\phi} = \sum_{i=1}^{s} b_i \mathbf{k}_i \tag{6.3}$$

This in turn allows for the state at epoch $(t_0 + h)$ to be estimated as [41]:

$$\boldsymbol{\eta}(t_0 + h) = \mathbf{X}_0 + h\boldsymbol{\phi} \tag{6.4}$$

By repeating this procedure until the desired final integration epoch is reached, it is possible to simulate the motion of an asteroid lander that is the solution of the governing differential equations.

Coefficients

The particular RK method applied in our software is the RK5(4) method, which is frequently used as default differential equation solver [42] and performs better than higher-order methods for the relatively small time steps used during our contact motion simulations. This method applies a fifth-order approximation for the main differential equation integration and a fourth-order approximation for the local truncation error estimation. The coefficients for this method[1] have been developed by [43] and are shown in Table 6.1. By implementing these coefficients into the numerical integration scheme presented above, our integrator is capable of propagating the governing differential equations of asteroid lander motion and produce simulated trajectories.

6.1.1 Time-Step Variability

In our discussion of the state approximation $\boldsymbol{\eta}$, we have mentioned the application of the time step h, but did not expand on the particular values that should be used. A good initial step size for the simulation of orbits is $1/100^{\text{th}}$ of the object's orbital period [41], yet is by no means an optimal value to use throughout an entire simulation. Indeed, the inherent error associated with the state approximation provided by a numerical integrator strongly depends on the applied step size. As this error often varies throughout an integration, it is generally desirable to adjust the applied step size h as the integration progresses. By applying two methods of successive order based on the same set of functions evaluations, we may obtain an estimate of the local truncation error, which can be used for an efficient step size control.

---

[1] More specifically, these coefficients belong to the RK5(4)7M method, which was shown by [43] to be the most accurate RK5(4) implementation.

Table 6.1: RK5(4) coefficients [43].

c_i	$a_{i,j}$						
0							
$\frac{1}{5}$	$\frac{1}{5}$						
$\frac{3}{10}$	$\frac{3}{40}$	$\frac{9}{40}$					
$\frac{4}{5}$	$\frac{44}{45}$	$-\frac{56}{15}$	$\frac{32}{9}$				
$\frac{8}{9}$	$\frac{19372}{6561}$	$-\frac{25360}{2187}$	$\frac{64448}{6561}$	$-\frac{212}{729}$			
1	$\frac{9017}{3168}$	$-\frac{355}{33}$	$\frac{46732}{5247}$	$\frac{49}{176}$	$-\frac{5103}{18656}$		
1	$\frac{35}{384}$	0	$\frac{500}{1113}$	$\frac{125}{192}$	$-\frac{2187}{6784}$	$\frac{11}{84}$	
b_i	$\frac{5179}{57600}$	0	$\frac{7571}{16695}$	$\frac{393}{640}$	$-\frac{92097}{339200}$	$\frac{187}{2100}$	$\frac{1}{40}$
$\hat{b}_i$	$\frac{35}{384}$	0	$\frac{500}{1113}$	$\frac{125}{192}$	$-\frac{2187}{6784}$	$\frac{11}{84}$	0

Such an *embedded method* of s stages yields two independent approximations, of respectively orders p and $p+1$ [41]:

$$\boldsymbol{\eta}(t_0 + h) = \mathbf{X}_0 + h \sum_{i=1}^{s} b_i \mathbf{k}_i \tag{6.5a}$$

$$\hat{\boldsymbol{\eta}}(t_0 + h) = \mathbf{X}_0 + h \sum_{i=1}^{s} \hat{b}_i \mathbf{k}_i \tag{6.5b}$$

Using these approximations, the local truncation error e can be estimated as [41]:

$$e(h) \approx |\hat{\boldsymbol{\eta}} - \boldsymbol{\eta}| \tag{6.6}$$

If the error estimate provided by Equation 6.6 is larger than some tolerance ε, the step should be repeated with a smaller step size. This new step size h^* may be computed using [41]:

$$h^* \approx \sqrt[p+1]{\frac{e}{|\hat{\boldsymbol{\eta}} - \boldsymbol{\eta}|}}\, h \tag{6.7}$$

In practice, about 0.9 times this maximum time step is applied for safety reasons to avoid a second step with unacceptable error estimate [41].

The time step modification used in our simulation software expands on the scheme of [41] that was presented above. As mentioned, the original scheme adjusts the step size and recomputes the respective integration step whenever the error estimate $e > \varepsilon$. Although this approach ensures the integration error never exceeds the user-defined upper bound, it does not provide any control over lower values of h. One realizes that an integration step carried out with very small h yields a very small error estimate; that step is therefore perfectly acceptable. However, running a state propagation with small h will require considerably longer computation times than a propagation where h is sufficient to guarantee that the error is only just smaller than ε. Our step size control therefore also applies a lower bound on the error ratio (e/ε).

This practice results in a scheme that adjusts the step size such that the associated truncation error lies between two user-specified values $(e/\varepsilon)_{min}$ and $(e/\varepsilon)_{max}$. Whenever the error exceed the $(e/\varepsilon)_{max}$ value, the step size should be adjusted and the integration step recomputed. Whenever the error is smaller than $(e/\varepsilon)_{min}$, the step size should simply be adjusted for the next step; recomputing is not necessary as the error ratio itself is perfectly acceptable from an accuracy perspective. It is finally noted that if the $(e/\varepsilon)_{max}$ ratio is set to exactly 1, it may occur that the error of some time step is still acceptable, but that the next step exceeds $(e/\varepsilon)_{max}$ and requires that step to be recomputed. It is therefore desirable to carry out the time step modification even when $(e/\varepsilon)_{max}$ reaches some value slightly smaller than 1; the integration step computed will still be acceptable but we avoid having to recompute the next step, as the integrator essentially anticipated that the error ratio would be exceeded if the time step was not adjusted. This scheme is illustrated in Figure 6.1.

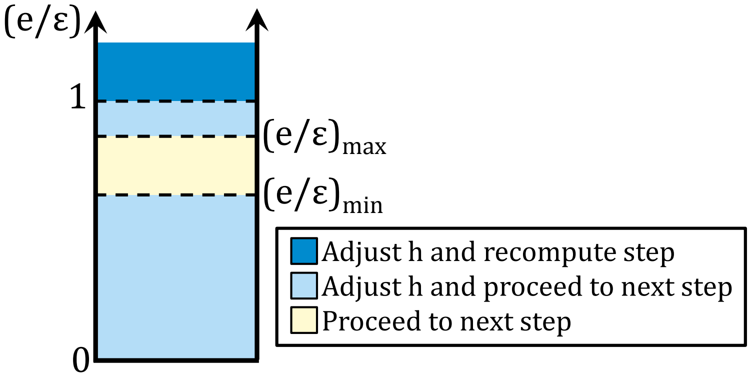
(e/ε)
1
0
(e/ε)max
(e/ε)min
Adjust h and recompute step
Adjust h and proceed to next step
Proceed to next step

Figure 6.1: Applied step adjustment scheme.

6.1.2 Constraint Application

In addition to verifying that the estimated error on the propagated state is not exceeded, our integrator is also capable of enforcing certain user-specified *constraints* on both the state and the time step. After each newly propagated step, the integrator will check for violation of the state constraints. If such violation is detected, consider for example the crossing of the Sphere of Influence (SOI) of the asteroid system, the state is modified according to that constraint's respective *constraint function*. In the case of an SOI crossing, this function might adjust the lander velocity such that the SOI crossing does not occur, or even terminate the simulation altogether.

Secondly, whenever the time step h is adjusted, the integrator will check whether this new value of h lies between the user-specified minimum and maximum time step value, *i.e.* that $h_{min} < h < h_{max}$. If the time step indeed exceeds these limits, it will be adjusted prior to carrying out any successive integration steps.

6.2 Event Capability

The numerical scheme presented above is highly capable of propagating continuous arcs of lander motion. Unfortunately, the full motion of a passive asteroid lander is far from continuous but instead interspersed with collisions and other instantaneous interactions with the asteroid. The numerical integration scheme was therefore expanded to be able to handle such instantaneous *events*; this event capability is discussed in the current section.

First and foremost, the integrator is able to detect the occurrence of events through the use of *event filler* functions. These are functions that take the state of the system as input and return either -1 or 1, values which indicate whether an event has indeed occurred. In the case of collision detection with the asteroid model, the event filler checks the value of $(d-R)$, where d is the minimum distance from the center of the lander pod to the asteroid and R the radius of the pod. As a collision occurs whenever $(d-R)=0$, the collision event filler will return:

$$\begin{cases} 1 & \text{if } (d-R) > 0 \\ -1 & \text{if } (d-R) < 0 \end{cases} \tag{6.8}$$

By checking after each integration step the value returned by the event filler and comparing it with that of the previous step, the integrator is able to detect if an event has occurred between two successive steps. As this detection does not directly provide information on the exact epoch of the event, the integrator will *converge* on that epoch upon event detection. This convergence is achieved using the *mid-point* or *bisection* algorithm.

To illustrate the working principles of this algorithm, consider that a sign change in the $(d-R)$ event filler is detected between epochs t_0 and t_1. Upon detection of the event, the integrator will compute the state and corresponding event filler at the intermediate epoch $t_m = \frac{1}{2}(t_0 + t_1)$ and compare the sign of the event filler at t_m with that at t_0 and t_1. If the sign change is found to occur in the interval $[t_0 \rightarrow t_m]$, the state at t_1 is replaced by that at t_m. If, on the other hand, the sign change occurs in $[t_m \rightarrow t_1]$, the state at t_0 is replaced by t_m. The halving of the time interval between the two considered states continues until $\Delta t = t_1 - t_0$ reaches some user-specified lower bound. This algorithm is illustrated in Figure 6.2. It is noted that when computing the mid-point t_m, one must make sure to only propagate forwards from t_0 and never propagate backwards from t_1, as the latter would result in a significant error build-up if a high number of collisions are being resolved sequentially.

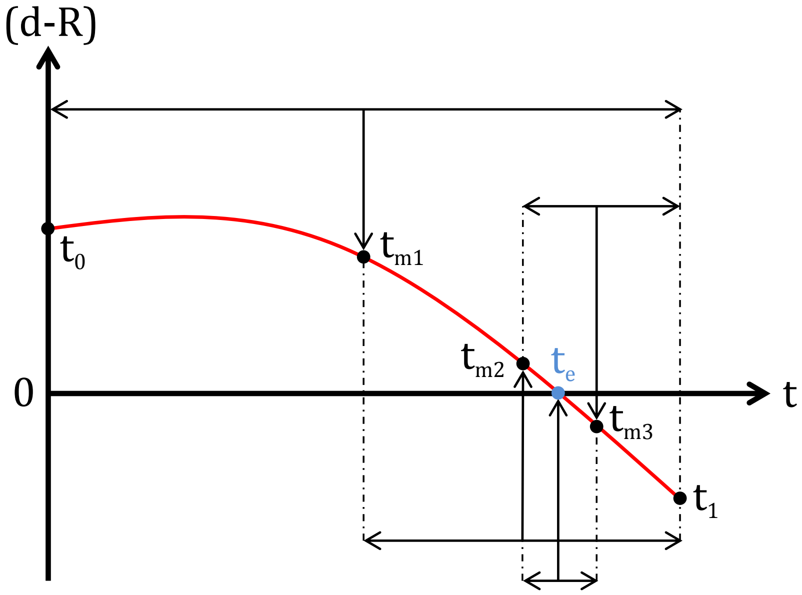

Figure 6.2: Mid-point algorithm used for event convergence.

Each event comes with a user-specified *side* property, which dictates whether the converged state instantaneously before or after the event epoch should be returned by the convergence algorithm. When considering the detection of a collision, we want the state instantaneously *before* the event epoch to be returned, as using the *after* state would result in the lander having physically crossed through the asteroid surface before the actual collision is handled. Once the algorithm has converged on the epoch of the event and constructed the corresponding state, the latter is modified by the event's respective *special* function. In the case of a collision, the velocity of the lander will be adjusted in accordance with the equations presented in Section 4.5. After handling the event, the integrator will resume propagation of the state until another event is detected.

This event detection scheme is capable of detecting multiple events between two successive integration steps, and will in that case converge on all detected events and determine their individual event epochs. Once these epochs have been obtained, the software will handle only that event which occurs *first* and then proceed with state propagation until another event is detected. It is finally noted that after event handling, the aforementioned constraint check is again performed and handled if necessary. This abstract propagation algorithm is visualized in Figure 6.3.

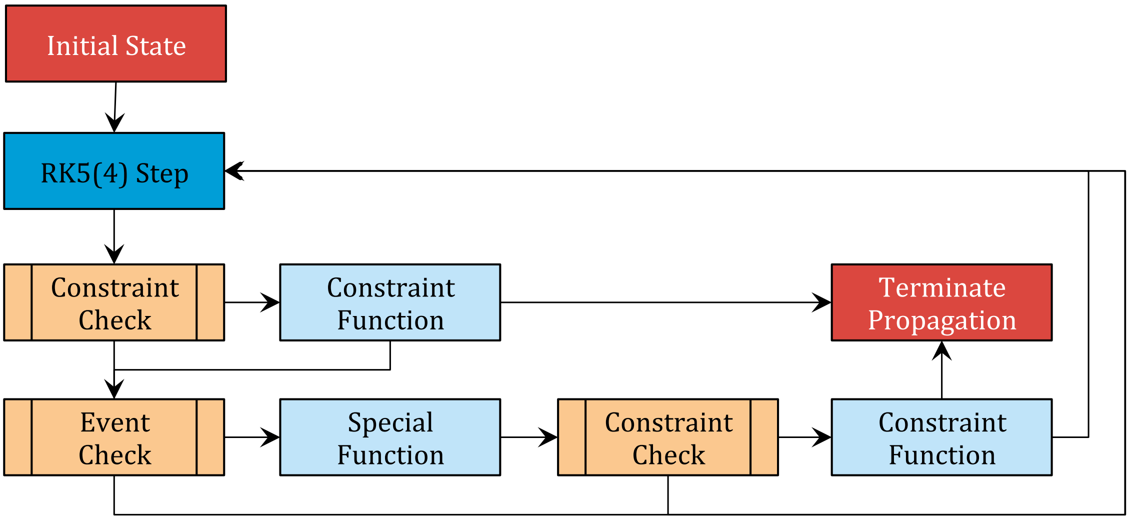

Figure 6.3: Algorithm structure of event-based propagator.

6.3 Algorithm Structure

The algorithm structure discussed in the above can be applied to the event-based propagation of any set of equations of motion. We now expand on that discussion and apply it to our problem of lander motion in the asteroid environment. In this description, we follow the 'full' algorithm structure as depicted by the flowchart shown in Figure 6.4.

The simulation of a lander trajectory starts from a construction of the initial state variables, as listed in Table 4.1, in function of the specified mode of propagation. Simulations are initiated with the lander 'flying' in the neighbourhood of the asteroid, *i.e.* without any contact present. This orbiting motion is propagated until a collision with the target asteroid body is detected, assuming propagation does *not* take place in mode 0, which ignores all contact interactions. After carrying out the collision, the software checks the value of the normal velocity $V_\perp$ of the lander relative to the surface feature it collided with. If this velocity is higher than some set limit, in our simulations $V_{\perp,\mathrm{min}} = 10^{-5}$ m/s, the 'flying' motion is continued. If $V_\perp < V_{\perp,\mathrm{min}}$, the normal velocity is set to zero and 'rolling' contact motion is initiated on the collision feature. This 'rolling' motion continues until either of the following three events are detected: the lander exits the contact feature, the lander collides with an additional feature, or the lander comes to a full stop.

The first event, the feature exit, is detected by monitoring the value of the normal force exerted by the contact feature during 'rolling' motion. When this normal force becomes smaller than zero, an exit is detected. If any of the surrounding surface features are found to produce a positive normal force, contact motion will be continued on the latter feature. This occurs, for example, when the lander rolls off one facet and onto a second facet. If no surrounding features produce a positive normal force, the lander will be returned to 'flying' motion and continue ballistic motion until it once again impacts the asteroid.

The second event, a rolling collision, is detected in the same way as collisions during 'flying' motion. Upon handling the collision, our software checks again the normal velocity relative to both the initial contact feature and the feature with which the lander collided. Depending on which of the features provide a positive normal force, the lander either continues contact motion on one or both of the features, or is returned to 'flying' motion.

Finally, the software will terminate the simulation when it detects both the lander velocity *and* rotation to be smaller than some set limits V_{end} and ω_{end}. When these two conditions are met, the software also checks the slope of the contact feature with respect to the local gravitational acceleration and ensures its value is below some set limit. The latter check is performed to verify the lander was not rolling upwards on a facet, a case in which both its velocity and rotation would be zero at some point, but would accelerate again as the lander starts rolling downwards again on that slope.

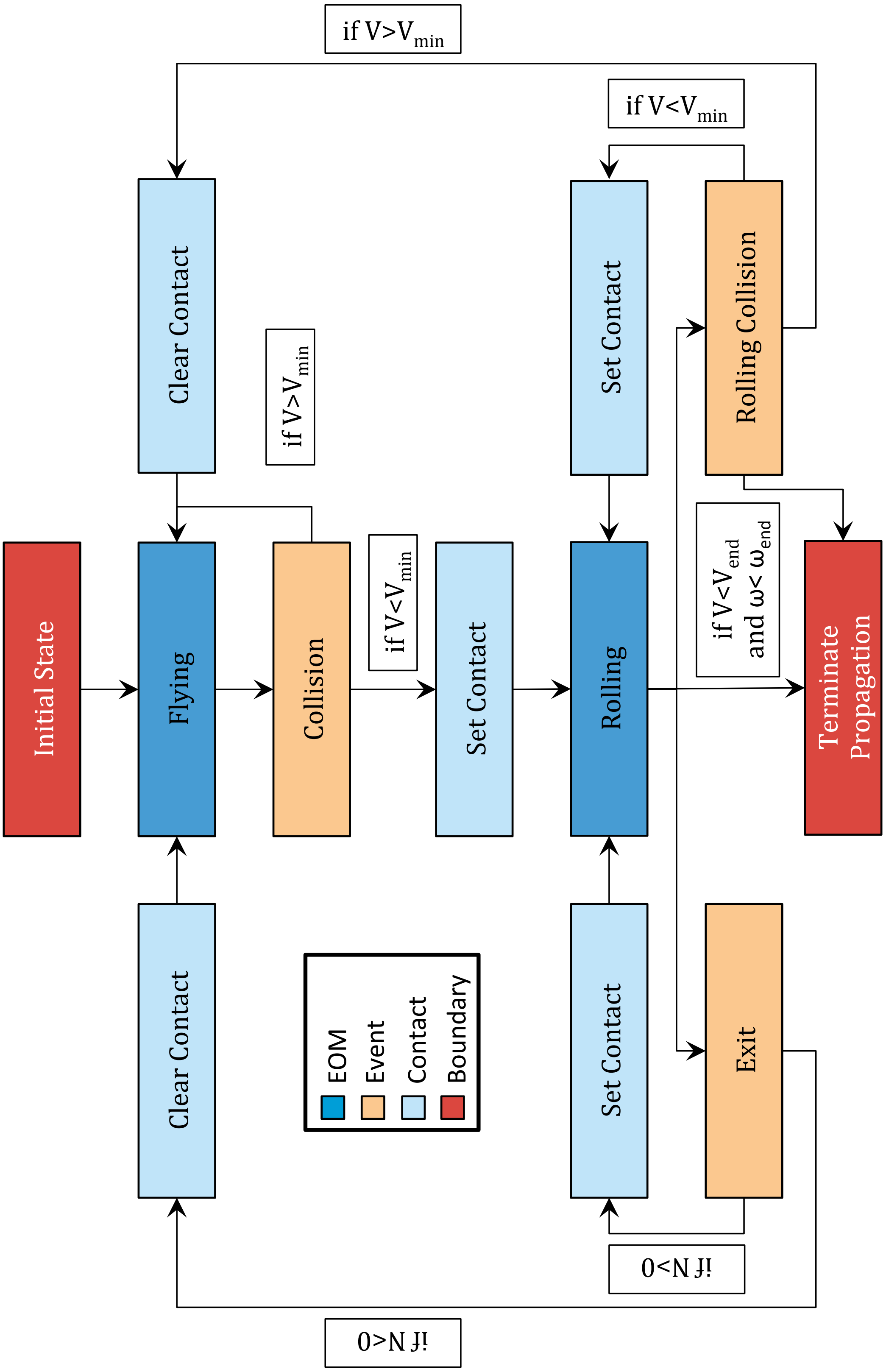
Initial State
Flying
Collision
if $V<V_{min}$
Set Contact
Rolling
if $V<V_{end}$ and $\omega<\omega_{end}$
Terminate Propagation
Clear Contact
if $V>V_{min}$
Set Contact
Rolling Collision
if $V<V_{min}$
if $V>V_{min}$
Clear Contact
Set Contact
Exit
if $N>0$
if $N<0$
EOM
Event
Contact
Boundary

Figure 6.4: Algorithm structure of asteroid lander simulation software.

Part III

Verification and Validation

Chapter 7

Gravity

THE COMPLEX GRAVITATIONAL fields of asteroids are modelled in our software using the constant density polyhedron model, which was presented in Section 4.3. The implementation of this model requires proper verification and validation, to ensure that our computations indeed yield the correct gravitational accelerations, in particular since we have modified this model in certain ways to suit our purposes. The current chapter presents the tests performed to indeed perform Verification and Validation (V&V) of this model. We first evaluate the original polyhedron model in Section 7.1, after which our linearization strategy is put to the test in Section 7.2. Next, we review the effect of the choice in model resolution in Section 7.3. Finally, in Section 7.4 we verify that trajectories are propagated correctly in the different available propagation.

7.1 Polyhedron Model

The amended potential $\Omega(\mathbf{X})$ of an asteroid body is defined as the sum of the gravitational and centrifugal potential [14]:

$$\Omega(\mathbf{X}) = U(\mathbf{X}) - \frac{1}{2}\omega^2(x^2 + y^2) \tag{7.1}$$

Where $U(\mathbf{X})$ is the gravitational potential at position $\mathbf{X}$, and ω is the uniform rotation rate of the asteroid body around its z-axis. As amended potential maps are available in literature for a number of asteroids, they provide excellent validation points for the polyhedron model, when we use it to compute the potential $U(\mathbf{X})$ in the above equation. Indeed, we apply this approach to asteroid 25143 Itokawa, where we have used a density of $\sigma = 1.98$ kg/m^3 and a rotation period of $P = 12.312$ hr, resulting in a rotation rate of $\omega = 1.4176 \times 10^{-4}$ rad/s. These are the same values as applied in [44], though unfortunately those authors' polyhedron model is not publicly available. Instead, we apply the model by [16] which consists of a similar number of facets, on the order of 13,000. The resulting amended potential field of

Itokawa is shown in Figure 7.1, where the ridge line[1] and equilibrium points of the field are marked respectively with a dashed line and stars. The colors red and blue are used to indicate respectively areas of high and low amended potential. We compare this with Figure 7.2 as taken from [16], which presents the same parameters.

We observe that Figures 7.1 and 7.2 are extremely similar, providing an initial confirmation that our computations are correct. Additionally, we have determined the locations of the equilibrium points of Itokawa's amended potential and compared them with those mentioned in [44]; both sets of values are included in Table 7.1. Furthermore, Figure 7.3 visualizes the locations of the equilibrium points as computed and as taken from [44] with black and red crosses respectively. We can see from both Table 7.2 and Figure 7.3 that although our computed equilibrium points are located close to those presented in [44], their locations do not completely match. This difference is explained through the fact that we have used a different polyhedron model than the authors of [44]. Furthermore, the amended potential field near these equilibria is extremely flat in the x-direction for maxima and in the y-direction for saddle points; these directions are therefore highly sensitive to small variations in the polyhedron model. We indeed observe that the differences in equilibrium locations are mainly in x-direction for the maxima and in y-direction for the saddle points. Finally, it is likely that the authors of [44] have used a slightly different x- and y-axes. A confirmation of this fact is visible in Figure 7.3, where the offset in equilibrium point location occurs in the same direction for all equilibria. The z-axis of both our model and that of [44] is the same, however, and aligned with Itokawa's axis of uniform rotation. This is confirmed through the fact that the difference in equilibrium point z-position is very small, as shown in Table 7.1. We conclude from this that our implementation of the polyhedral gravity model has been validated to work correctly.

7.2 Linearization

The applied gravity field linearization discussed in Section 4.3 results in strongly reduced propagation times, in particular when the lander is performing contact motion and the ap-

---

[1] For a detailed definition of the ridge line, the reader is referred to [16].

Table 7.1: Itokawa equilibrium point locations.

	Computed			Literature			Difference		
Type	x [m]	y[m]	z[m]	x[m]	y[m]	z[m]	Δx [m]	Δy [m]	Δz [m]
Max	57.8	464.7	2.0	32.5	469.2	1.9	25.3	-4.5	0.7
Saddle	-509.7	38.5	-4.7	-512.1	23.1	-4.3	2.4	15.4	-0.4
Max	13.8	-471.0	1.3	34.1	-471.9	1.5	-20.3	0.9	-0.2
Saddle	519.7	-5.3	-8.4	520.5	17.3	-8.4	-0.8	-22.6	0.0

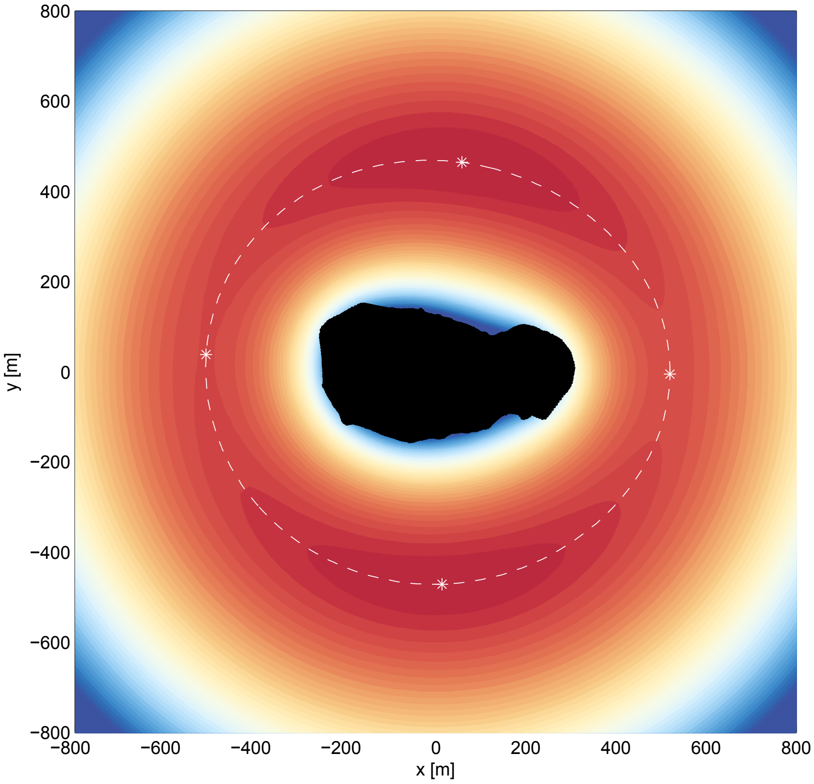

Figure 7.1: Itokawa amended potential field with equilibrium points.

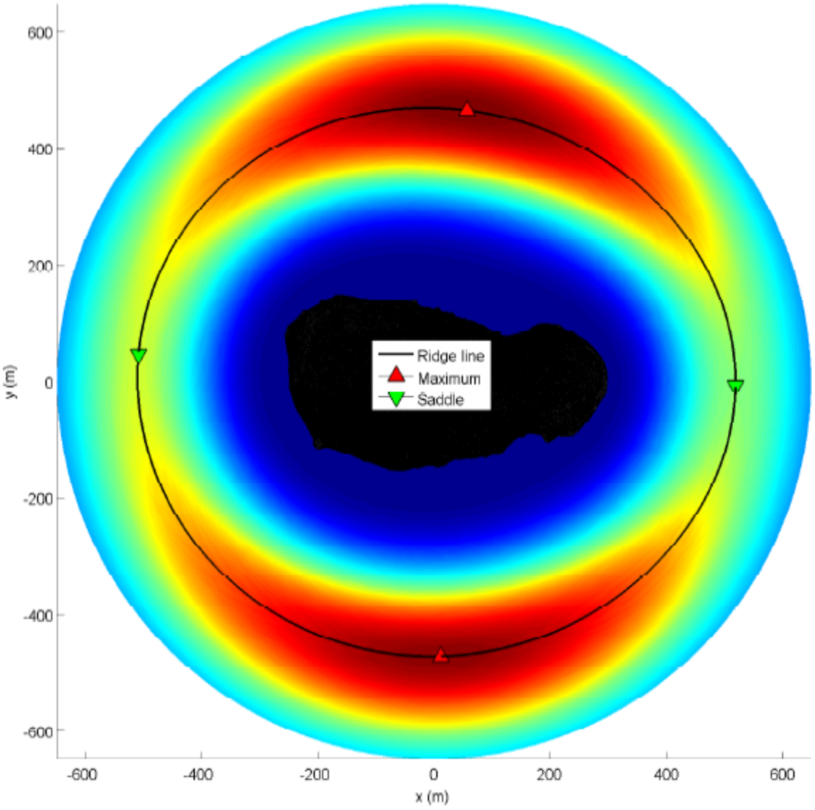

Figure 7.2: Itokawa amended potential field with equilibrium points [16].

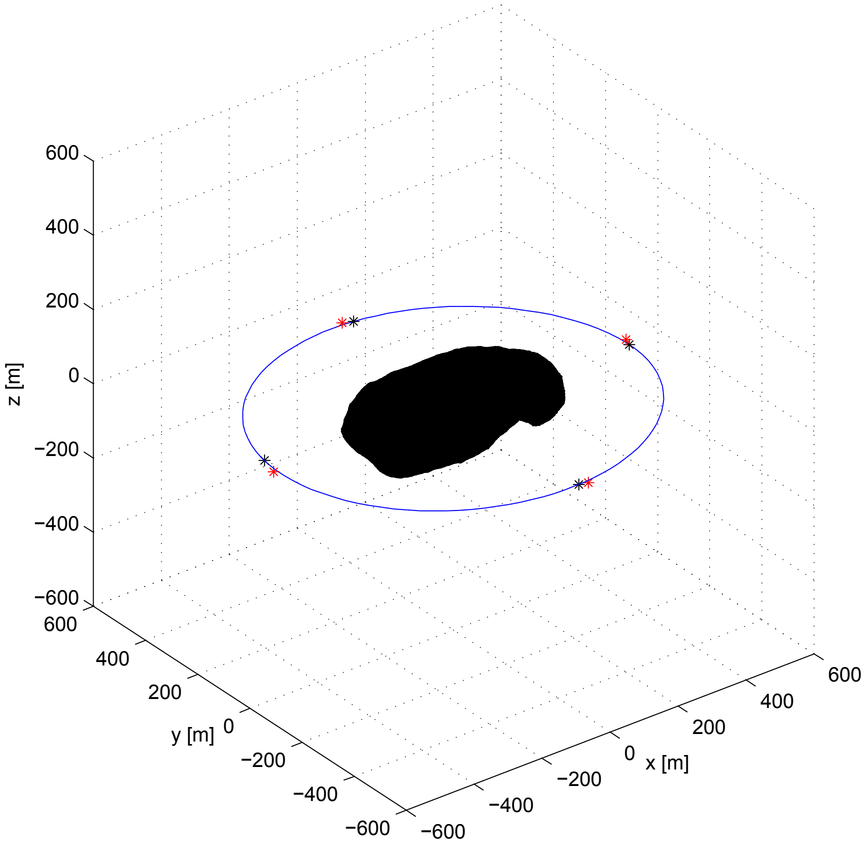

Figure 7.3: Comparison of equilibrium points of Itokawa.

plied time step is small. However, there is an error associated to this linearization that grows when moving further away from the applied reference state. It is therefore important that the particular value of $\Delta\mathbf{X}_{max}$ used during propagation is selected such that the produced error is of an acceptable magnitude. For this purpose, we have computed the gravitational acceleration at a set of collinear points for both asteroids 25143 Itokawa and 1999 KW_4 Alpha, at different values of $\Delta\mathbf{X}_{max}$. To present a meaningful comparison between both bodies, these values have been chosen as a ratio of the mean volumetric radii[2] R_V of both bodies.

The results of these tests are shown in Table 7.2 and visualized in Figure 7.4. For Itokawa, the field points tested ranged from [0,200,0] m to [0,210,0] m in steps of 0.02 m; for KW_4 Alpha, the field points tested ranged from [0,1000,0] m to [0,1040,0] m in steps of 0.1 m. We can see from Table 7.2 that indeed the inherent error of the gravity field linearization is a function of $\Delta\mathbf{X}_{max}$; the larger this value, the larger the error. Furthermore, the error magnitude of both systems as a function of $\Delta\mathbf{X}_{max}$ is very similar. This table may be used to provide control over the expected error in the gravitational acceleration; a value of $\Delta\mathbf{X}_{max}/R_V = 1/100$ is a good default value to use. It is noted that during the propagation of free-flying motion, the applied time step is generally such that $\Delta\mathbf{X}_{max}$ is exceeded at each step; the gravitational acceleration is therefore fully recomputed at each integration step. Furthermore, the applied assumptions of the contact motion model produce an error that is far greater than what is produced by most $\Delta\mathbf{X}_{max}$ values. We therefore argue that if computational speed is an absolute must, even $\Delta\mathbf{X}_{max}/R_V$ values up to 1/25 are acceptable.

---

[2] The mean volumetric radius is the radius of a sphere with the same volume as the body under consideration.

Finally, we consider Figure 7.4 which visualizes for Itokawa the relative error in acceleration for some of the values of $\Delta\mathbf{X}_{max}$ when moving from [0,200,0] to [0,210,0]. We observe that the error grows for all $\Delta\mathbf{X}_{max}$ as we move away from the initial state, due to the application of linearization. Furthermore, we observe that the error curve is tangent to zero near the applied reference state; this is expected as linearization is near-exact when being applied very close to the reference state. Upon reaching $\Delta\mathbf{X}_{max}$, the error is seen to suddenly drop as a new reference state $\mathbf{X}_1$ is computed at a distance slightly smaller[3] than $\Delta\mathbf{X}_{max}$ along the velocity direction. When continuing to move outwards, the error is seen to decrease again as the new reference state is approached. From all this we conclude that the gravity linearization indeed works correctly.

7.3 Model Resolution

The contact interactions between a lander and the asteroid surface is modelled in our software using high-resolution polyhedral models. The use of such computationally intensive models is possible in that case due to the subdivision of the global model into smaller, local worlds as discussed in Section 5.3. Unfortunately, this approach cannot be applied to the computation of an asteroid's gravity field using this model, as using the full-resolution model would ex-

---

[3] This is done to avoid numerical instabilities.

Table 7.2: Linearization.

	Itokawa ($R_V = 62.393$ m)		KW$_4$ Alpha ($R_V = 253.360$ m)	
$\frac{\Delta\mathbf{X}_{max}}{R_V}$ [-]	$\Delta\mathbf{X}_{max}$ [m]	$\left(\frac{g}{g_0}\right)_{max}$ [-]	$\Delta\mathbf{X}_{max}$ [m]	$\left(\frac{g}{g_0}\right)_{max}$ [-]
1/200	0.312	3.7254×10^{-6}	1.267	5.4177×10^{-6}
1/100	0.624	1.5592×10^{-5}	2.534	2.3089×10^{-5}
1/75	0.832	2.7246×10^{-5}	3.378	4.2319×10^{-5}
1/50	1.248	6.2170×10^{-5}	5.067	9.4947×10^{-5}
1/25	2.496	2.4711×10^{-4}	10.134	3.7658×10^{-4}
1/10	6.239	1.5252×10^{-3}	25.336	2.3096×10^{-3}

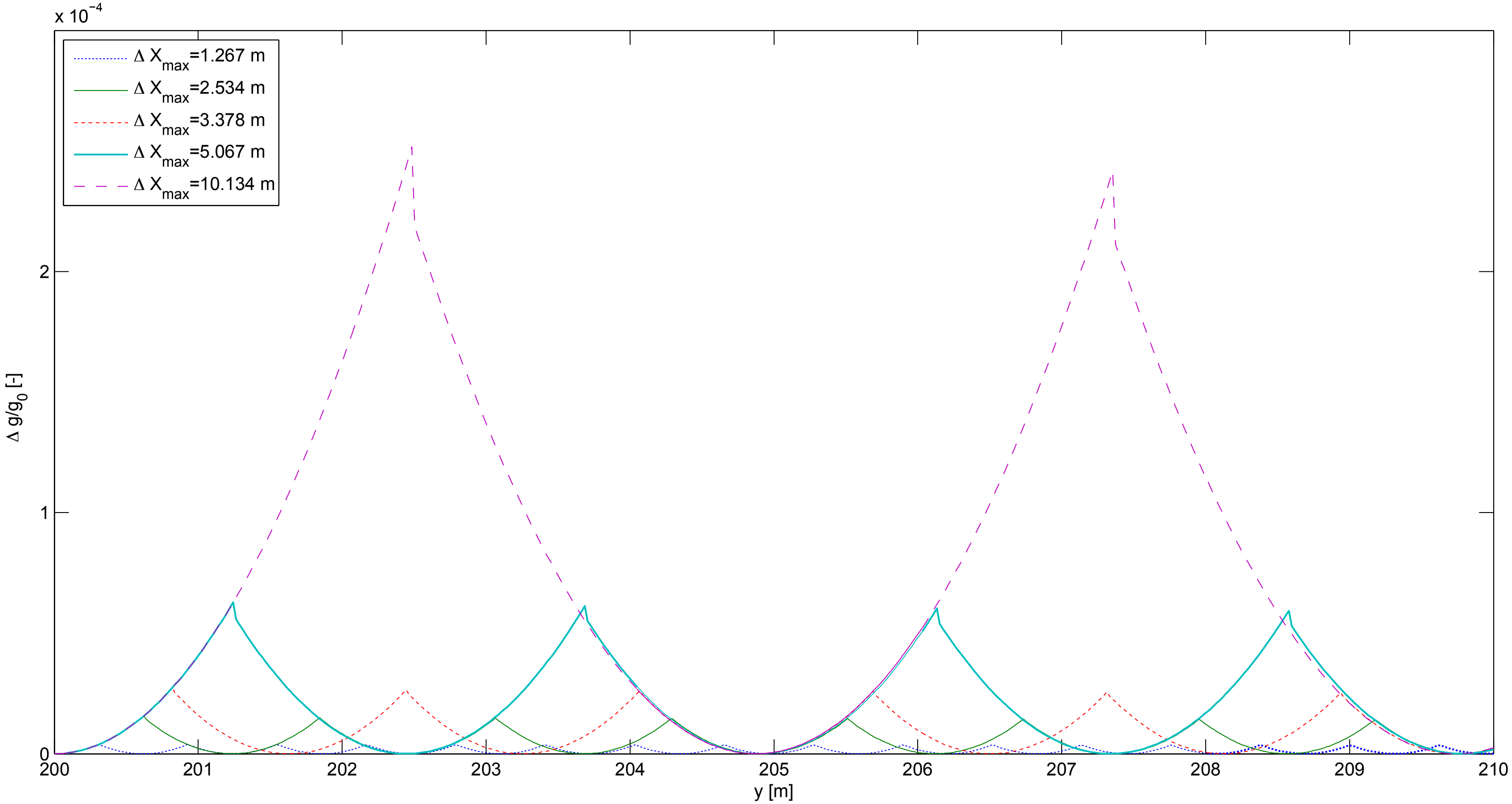

Figure 7.4: Linearization error for Itokawa for different values of $\Delta \mathbf{X}_{max}$.

plode the total time required to propagate even a single simulation. Instead, we use simplified models of lower resolutions to reduce the computation effort of evaluating the gravitational model. These simplified models are constructed from an asteroid's full-resolution model, by reducing the total number of vertices of the model. As a result, the simplified models 'average' the shape of their respective full model.

Due to this shape averaging, the volume of a simplified model differs from that of the original, full-resolution model. To ensure coherence between the original and simplified models of an asteroid, the density σ of any model is computed using the mass of that asteroid, and the volume contained by the considered polyhedron model. The computed mass $m = \sigma V$ and equivalent point-mass acceleration $g = Gm/r$ will therefore always be the same, regardless of the resolution of the applied model. Additionally, the coordinates of the simplified models are shifted such that the center of mass of the polyhedron coincides with the origin of the applied coordinate system.

By constructing simplified models using this strategy, they provide the best possible approximation of the full-resolution gravity model, using a reduced number of polyhedron vertices. Nevertheless, an inherent error is introduced. To obtain an estimate of the magnitude of this error, we evaluate the gravitational attraction at a number of field points near asteroid 25143 Itokawa, for models of different resolution. The applied models and their relevant parameters are shown in Table 7.3; a visual comparison of their resolutions is shown in Figure 7.5. It can be seen from Table 7.3 that models with a lower resolution have a higher density, this is consistent with their decrease in volume and the requirement of constant total mass. The coordinates of the tested field points are listed in Table 7.4; the norms of the differences in gravitational attraction between the simplified and full models are shown in Table 7.5, for all field points.

We observe from Table 7.5 that the error in gravitational attraction e_i increases when the total number of facets is reduced. This is to be expected; when we decrease the number of

Table 7.3: Overview of tested polyhedron models M_i of 25143 Itokawa.

Model	$N_{\mathcal{V}}$	$N_{\mathcal{F}}$	V [10^7 m^3]	σ [kg/m^3]	Surf. err. [%]
Full	98,306	196,608	1.7968	1,953.44	
M_4	2,562	5,120	1.7539	2,001.32	0.97
M_3	642	1,280	1.7255	2,034.10	1.65
M_2	162	320	1.5913	2,205.75	8.89
M_1	42	80	1.2678	2,768.55	24.40
M_0	12	20	0.7539	4,655.78	57.26

Table 7.4: Coordinates of tested field points.

Point #	1	2	3	4	5	6	7	8	9	10	11	12	13	14	15
x [m]	300	350	400	450	500	0	0	0	0	0	0	0	0	0	0
y [m]	0	0	0	0	0	-150	-200	-250	-300	-350	0	0	0	0	0
z [m]	0	0	0	0	0	0	0	0	0	0	-100	-150	-200	-250	-300

Table 7.5: Analysis of results of polyhedron gravity-model verification.

Point #	e_4 [%]	e_3 [%]	e_2 [%]	e_1 [%]	e_0 [%]
$N_{\mathcal{F}}$	5,120	1,280	320	80	20
P_1	0.54	0.91	5.55	17.65	52.58
P_2	0.12	1.34	5.65	23.15	39.22
P_3	0.10	1.20	5.07	18.14	29.51
P_4	0.18	1.04	4.24	14.16	22.82
P_5	0.20	0.88	3.52	11.26	18.11
P_6	0.37	0.28	6.16	16.27	22.89
P_7	0.61	0.77	4.82	13.02	21.86
P_8	0.49	0.69	3.75	10.24	17.59
P_9	0.39	0.59	2.98	8.14	13.96
P_{10}	0.31	0.50	2.39	6.56	11.16
P_{11}	1.99	3.78	15.28	39.27	96.31
P_{12}	1.55	3.00	11.48	32.02	63.75
P_{13}	1.18	2.36	8.70	23.33	41.40
P_{14}	0.88	1.82	6.55	17.19	28.73
P_{15}	0.65	1.40	4.97	12.91	20.90

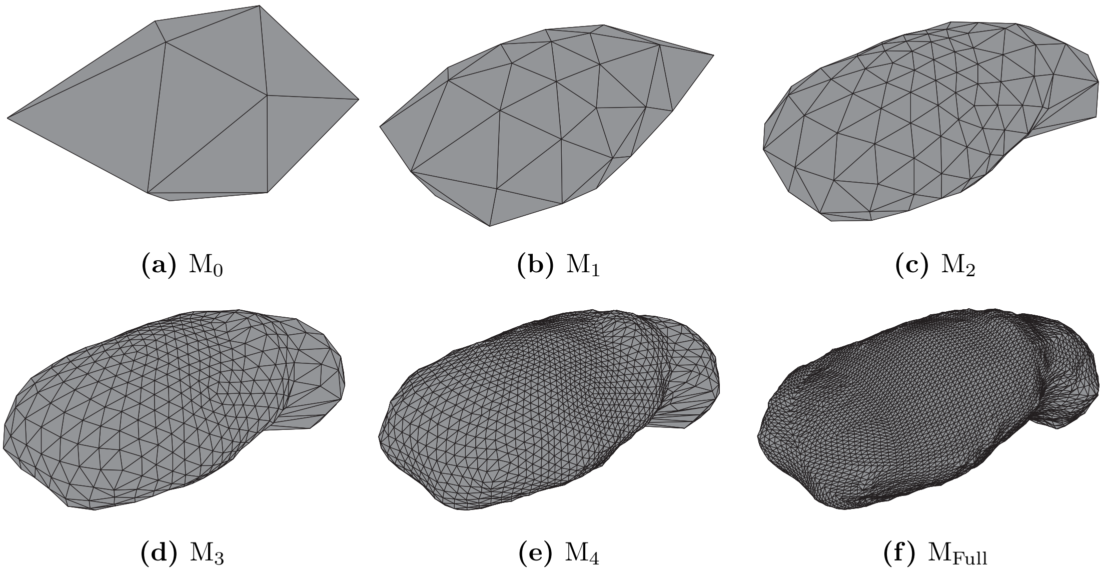
(a) M_0 (b) M_1 (c) M_2

(d) M_3 (e) M_4 (f) M_{Full}

Figure 7.5: Overview of different model resultions of 25143 Itokawa.

facets, we decrease the capability of the polyhedron model to capture small gravity variations. Furthermore, the error is seen to decrease as we move away from the asteroid surface. This fact also agrees with our expectations; with increasing distance from the surface, the gravity field will approach that of a point mass and lose its sensitivity to local mass variations. We observe that the error for points along the z-axis is about 2.5 times as high as that encountered along the x- and y-axes. The cause of this fact, which is visible in all model resolutions, remains unknown.

We conclude from Table 7.5 that models M_0 and M_1 are completely unusable due to their large error; this could be expected when reviewing the shape models in Figure 7.5. Indeed, models M_0 and M_1 lack the resolution to even capture Itokawa's irregular shape to a limited degree. Model M_2 does a far better job, with an error of $\sim 7\%$ near the surface, using a 'mere' 320 facets - yielding appreciably fast simulations on the order of 10 seconds computation time. While models M_3 and M_4 further reduce the error in gravitational acceleration to less than 1%, they consist of a large number of facets and therefore require significant CPU time to be evaluated. Therefore, we have chosen to restrict our simulation to using the M_2 model, despite its slightly larger-than-desired error. This will ensure our simulations can be run in acceptable time spans. It is also argued that the polyhedron model itself is inherently erroneous as its assumption of constant density fails to capture local mass variations in the asteroid body; further justifying the acceptability of the M_2 model's error. Nevertheless, improvements of the applied gravity modelling will be given significant attention in the recommendations for future work presented in Chapter 11.

7.4 Propagation Mode

For the final step in the V&V of the applied gravity field modelling, we switch our attention to the selected mode of propagation. As discussed in Section 4.7, the state variables will be propagated in different reference frames, depending on the selected mode. To verify whether propagation is carried out correctly regardless of the mode, we compare the results for simulations of the same orbit propagated in all modes. This was done for Itokawa in respectively modes Uni 0 and Uni 1, where the initial conditions were selected to resemble a circular orbit the asteroid, and converted into the proper reference frames. This resulted in two representations of the same lander trajectory, in respectively the TIF and the RB1F. To verify whether these trajectories indeed coincide, we have respectively converted each to the other, leading to a total of 4 trajectories; these are shown in Figure 7.7. For clarification, 'TIF→TIF' is the trajectory propagated in the TIF, shown in the TIF. On the other hand, 'TIF→RB1F' is the same trajectory but converted into the RB1F.

We observe that both sets of trajectories indeed seem to coincide; for a more detailed analysis we have computed the difference in position between the trajectory propagated in the TIF, and the trajectory propagated in the RB1F converted to the TIF. These differences are shown in Figure 7.6. We can see from this graph that the differences between both trajectories are indeed minimal and do not exceed 10^{-5} m within our 70-hour mission time, and are limited to far lower values during the first 15 hours of the simulation. Though this shows the error does grow in time and limits the accuracy of our simulations over an extended period of time, we are not interested in simulations that last over 15 hours as any realistic lander hardware will be restricted in battery life. We therefore conclude that propagation is handled correctly in all frames for unitary systems.

This comparison was repeated for an orbit around 1999 KW_4 Alpha, propagated in modes Bin 0, Bin 1, and Bin 2. The resulting trajectories are converted into all three frames and shown in Figure 7.8; they again seem to be consistent. For a more detailed analysis, Figure 7.9 shows the differences in lander position for the trajectories in the RB1F. We can see that the maximum error encountered in the 70-hour propagation time is about 10^{-1} m, four orders of magnitude larger than the maximum error encountered during the unitary-body simulations. While this is a considerable error, when restricting ourselves to the first 15 hours of propagation, the maximum error is of the acceptable order of 10^{-4} m. We therefore conclude that also the propagation of lander motion in a binary system is carried out correctly in all reference frames. The exact source of these seemingly regular oscillations remains unknown.

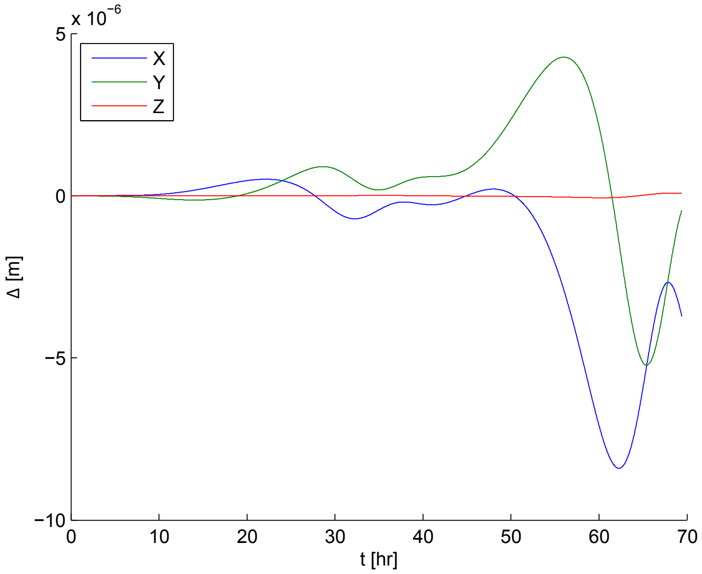

Figure 7.6: Difference of results from propagation in Uni 0 and Uni 1 around Itokawa.

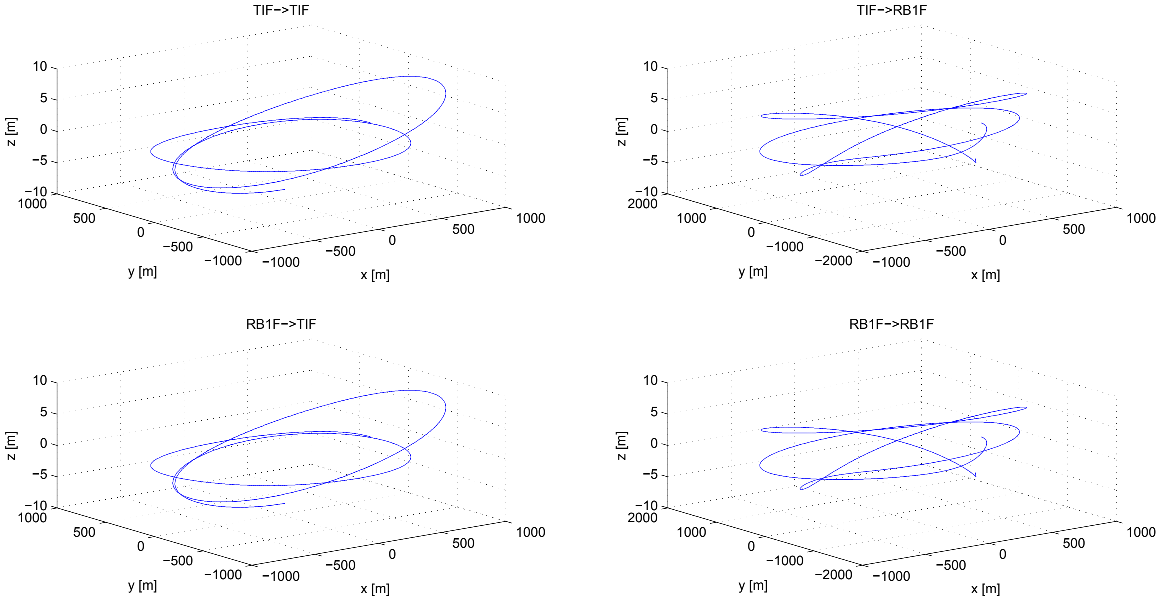

Figure 7.7: Transformed results from propagation in Uni 0 and Uni 1 around Itokawa.

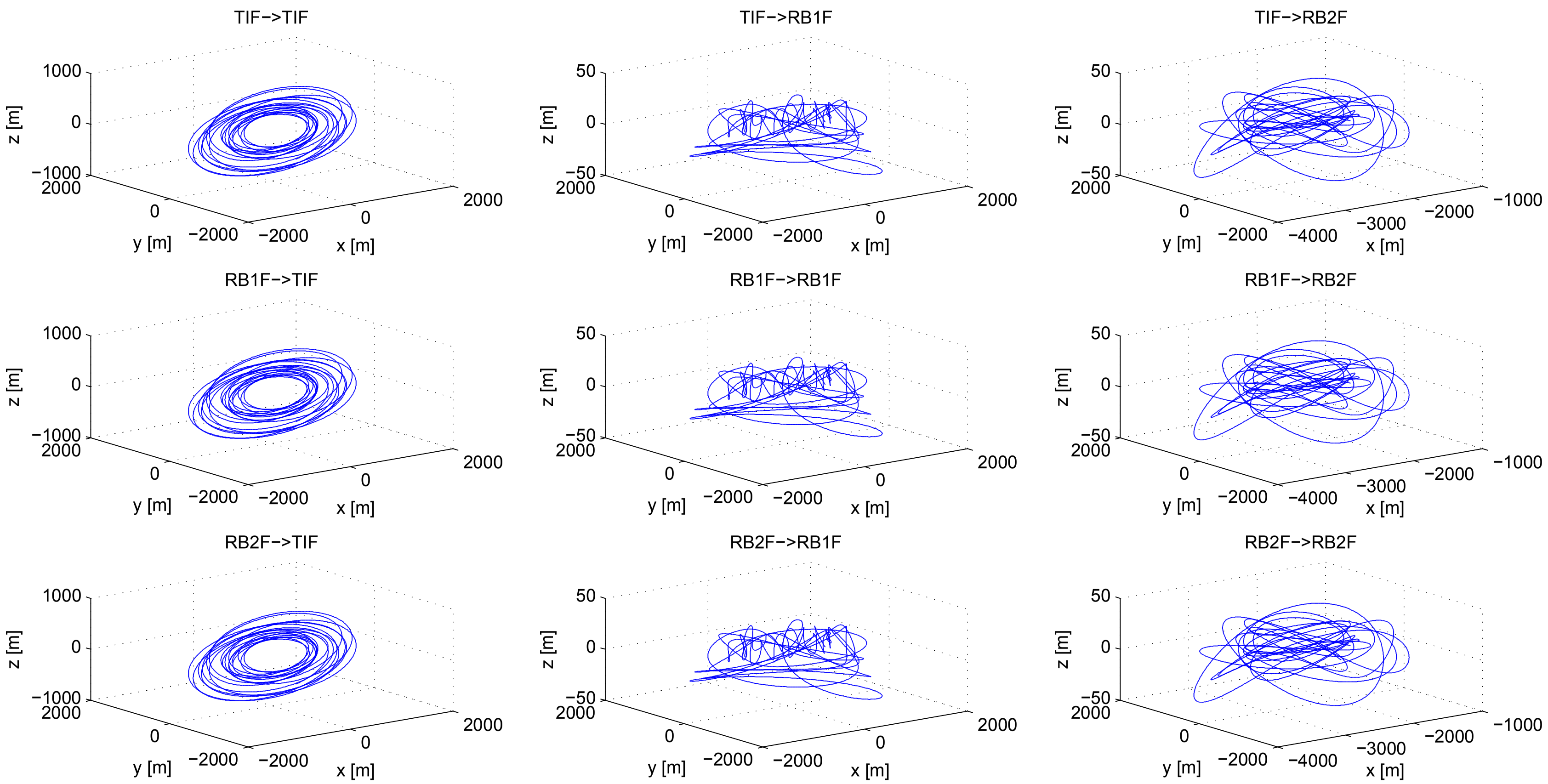

Figure 7.8: Transformed results from propagation in Bin 0, Bin 1 and Bin 2 around around 1999 KW_4 Alpha.

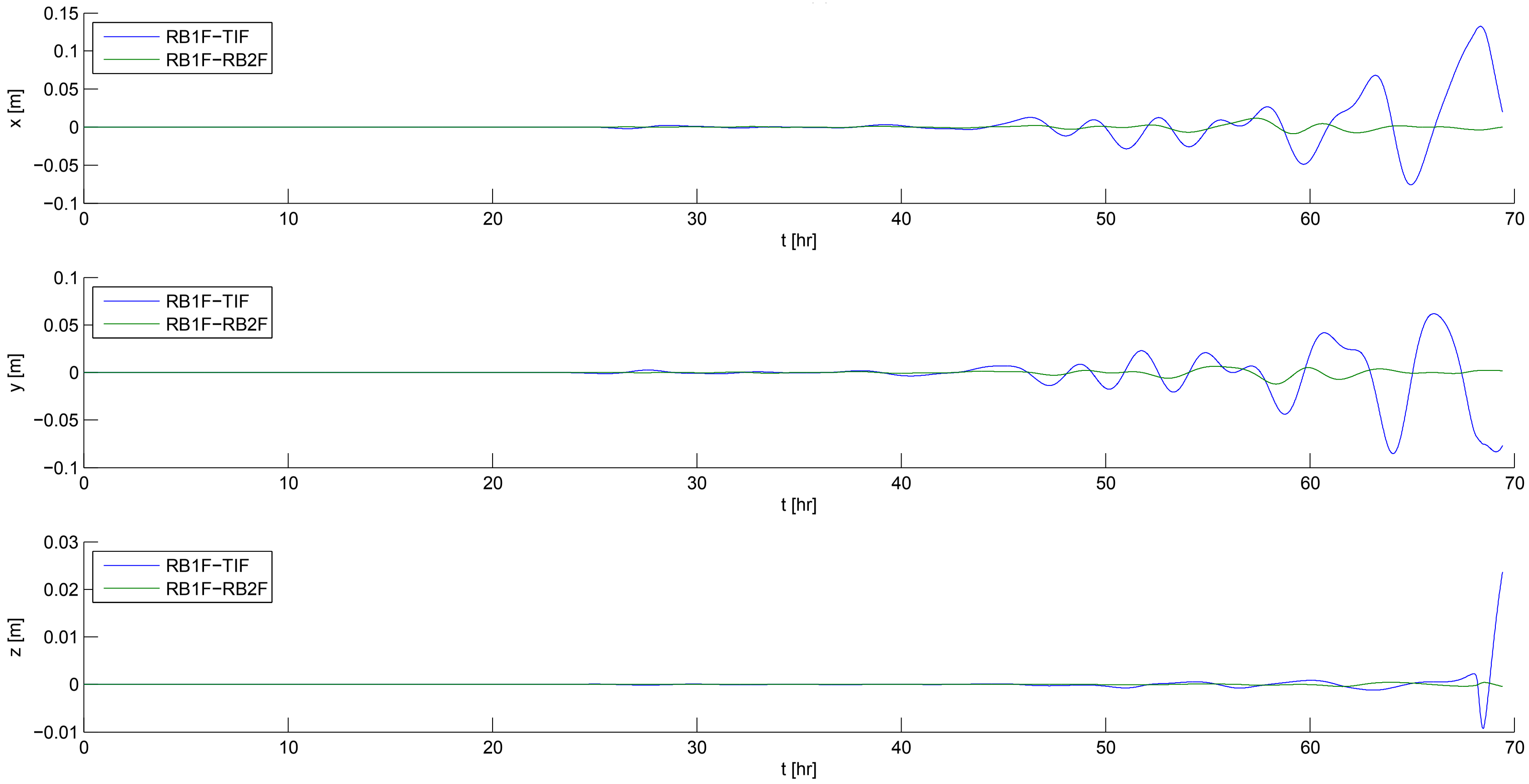

Figure 7.9: Difference of results from propagation in Bin 0, Bin 1 and Bin 2 around 1999 KW_4 Alpha.

Chapter 8

Contact Motion

Analagous to the verification and validation that was performed for our gravity modelling in Chapter 7, the present chapter is focused on detailing the steps taken in the V&V of the contact motion modules. We first set out a basic environment in Section 8.1, and then use this in Section 8.2 to verify our implementations of impacts, and in Section 8.3 to verify rolling motion. Finally, we provide simulations with a number of more complex surfaces to extend our V&V to these situations.

8.1 World Set-Up

Performing verification of contact motion directly on a full asteroid model is difficult due to the variability in local slope and gravity of the polyhedron model, as discussed in Section 4.3. Instead, a unit test is performed using a perfectly flat world with a uniform gravity field. This world is implemented into the lander simulator software as a collection of parallel facets which together form a square with side 160 meters. The center of this square coincides with the origin of the applied axis system; the surface of the square lies in the xy-plane with coordinate z=0. A visualization of this surface may be seen in Figure 8.1. Imposed on this flat world is a uniform gravity field, which provides a constant and position-independent acceleration in the negative z-direction. The potential energy of a particle in such a gravity field may be expressed as:

$$E_{pot} = -gz \tag{8.1}$$

In this equation, z is the distance of the particle along the z-axis, defined with respect to the flat surface and g is the (constant) gravitational acceleration. We note that this acceleration is defined along the positive z-axis, and that therefore $g < 0$.

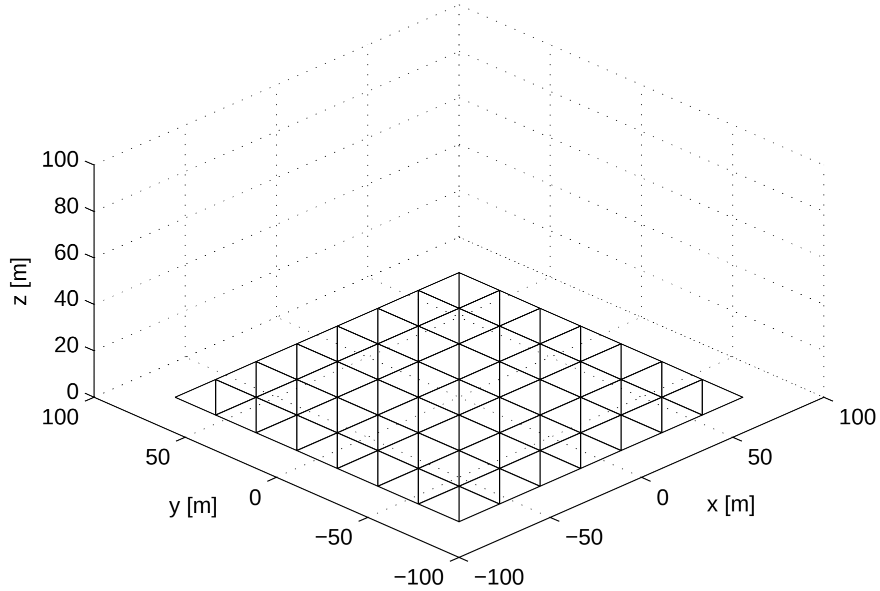

Figure 8.1: Flat world used for validation of contact motion.

8.2 Collisions

As a first unit test, we consider the bouncing motion of a ball along the x-axis of the flat world shown in Figure 8.1. For this case, all motion along the y-axis may be disregarded as $y = \dot{y} = \ddot{y} = 0$. The forces and torques acting on the pod in this set-up are shown in Figure 8.2; these are the same surface interactions discussed in Section 4.5.

8.2.1 Analytical Results

Assuming the ball is released with some initial conditions $[x_0,\dot{x}_0,z_0,\dot{z}_0]$, it will descend towards the surface along a parabola in the xz-plane as a result of the uniform gravitational acceleration. The motion of the ball during this ballistic flight can be described by the free-fall equations as:

$$\text{Free fall:} \begin{cases} x(t) = x_0 + \dot{x}t \\ z(t) = z_0 + \dot{z}_0 t + \frac{1}{2}gt^2 \end{cases} \tag{8.2}$$

By setting $z(t_1) = r$, where r is the radius of the ball, it is possible to compute the time of first impact of the ball with flat surface as:

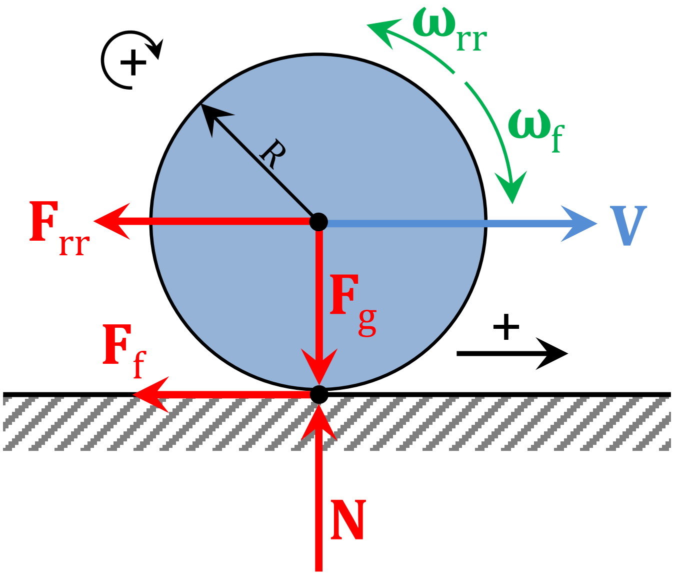

Figure 8.2: Contact forces and torques acting on the ball during surface contact.

$$t_1 = \frac{-\dot{z}_0 - \sqrt{\dot{z}_0^2 - 2g(y_0 - r)}}{g} \tag{8.3}$$

The corresponding x-position at this first impact can be computed as:

$$x_1 = x_0 + \dot{x}_0 t_1 \tag{8.4}$$

Upon impacting the flat surface, the ball will experience an instantaneous change in velocity and rotation rate as a result of the normal, friction and rolling resistance forces and torques that produce impulses during the bounce. For the uni-axial unit test applied here, the normal velocity impulse may be computed in function of the ball's coefficient of restitution e as (see also Section 4.5):

$$J_N = -(1+e)\dot{z} \tag{8.5}$$

The normal velocity before and after the first impact are related through this normal impulse as:

$$\dot{z}_{1+} = \dot{z}_{1-} + J_N \tag{8.6}$$

In this equation, the indices - and + refer to the state of the ball before and after the impact, respectively. The associated friction force impulse was presented in Section 4.5 and reduces for this uni-axial case to:

$$J_F = -\min\left(fJ_N, \frac{\dot{x} + \omega r}{1 + r^2 \bar{I}^{-1}}\right) \tag{8.7}$$

Note how the negative sign in Equation 8.7 indicates that the force opposes the velocity of the ball, as also shown in Figure 8.2. The associated friction-torque impulse can be computed as:

$$T_F = -rJ_F \tag{8.8}$$

This impulse acts in the positive rotation direction, see again Figure 8.2. The velocity of the ball parallel to the flat surface, as well as its rotation, can therefore be calculated instantaneously after the collision as:

$$\begin{cases} \dot{x}_{1f} = \dot{x}_{1-} + J_F \\ \omega_{1f} = \omega_{1-} + \bar{I}^{-1} T_F \end{cases} \tag{8.9}$$

In this equation, $\bar{I} = \frac{2}{5}r^2$ is the mass-normalized inertia of the ball. In addition to the normal and friction impulses discussed above, the ball also experiences a torque and related force impulse generated by rolling resistance. The torque impulse resulting from this interaction was presented in Section 4.5 and reduces for the unit test to:

$$T_{rr} = -\min\left(C_{rr} r J \omega_{1f}, \bar{I}\omega\right) \tag{8.10}$$

This torque is applied on the ball together with the associated rolling resistance force, given for this case by:

$$J_{rr} = \bar{I}^{-1} r T_{rr} \tag{8.11}$$

By applying these rolling resistance impulses, the final velocity and rotation of the ball at an epoch instantaneously after the impact may be computed as:

$$\begin{cases} \dot{z}_{1+} = \dot{z}_{1f} + J_{rr} \\ \omega_{1+} = \omega_{1f} + \bar{I}^{-1} T_{rr} \end{cases} \tag{8.12}$$

Using these equations, the post-impact state of the ball is computed, after which it will describe a second parabolic arc of ballistic motion under influence of the uniform gravitational attraction. The time to this second, and any subsequent impacts, can be computed by applying again the free-fall equations as:

$$t_i = t_{i-1} - \frac{2\dot{z}_{i+}}{g} \tag{8.13}$$

The x-position of the ball at the time of these respective impacts is expressed as:

$$x_i = x_{i-1} + \dot{x}_{(i-1)}(t_i - t_{i-1}) \tag{8.14}$$

By repeatedly applying these equations, the effects of the infinite bounces resulting from $e \neq 1$ can be computed. As this process would require an infinite number of computations, in practice some velocity $\dot{z}_{min}$ is specified by the user. When the velocity $\dot{z}$ of the ball reaches below this minimum velocity as a result of some n-th bounce, this vertical velocity will be set to zero, *i.e.* $\dot{z} = 0$. However, as it has been implicitly assumed that the coefficient of restitution e is independent of the state of the ball, it is possible to solve for the effect of the remaining infinite number of bounces that occur over a finite time span after $\dot{z} < \dot{z}_{min}$. This is done by applying one final bounce immediately after the bounce that resulted in $\dot{z} < \dot{z}_{min}$, with a (virtual) incoming velocity as defined in Section 4.5 as:

$$\dot{z}_{\infty} - = -\frac{1}{1-e}\dot{z}_{1+} \tag{8.15}$$

If the vertical velocity of the ball is set to $\dot{z} = 0$ after carrying out this final bounce, the state of the ball will match the state of a ball for which the full infinite series of bounces was carried out, as discussed in Section 4.5.

8.2.2 Numerical Simulations

By comparing results from numerical simulations with solutions to the aforementioned analytical approach, it is possible to verify and validate the correct workings of the collision handling software. This validation is discussed here in separate steps, so as to analyse the effect of the collisions themselves, of different $\dot{z}_{min}$ values, and of the application of the virtual bounce. Table 8.1 lists the initial conditions and system parameters that were applied to both the analytical and numerical model, for the flat world with uniform gravity discussed in Section 8.1. Please note that these parameters were selected such that the ball does not interact with more than a single facet; extended motion that spans multiple facets will be discussed further on in this chapter. It is also noted that the magnitude of the ball's velocity and of the gravitational acceleration are representative of those encountered in the typical asteroid environment.

The time and resulting state of the first three impacts were computed using both the analytical and numerical models. Both these sets of results are shown with their absolute differences in Table 8.2, where digits differing between the two solutions are marked in bold type. It is noted that the numerical results were obtained using a relative tolerance of 10^{-9} with a time convergence precision of 10^{-7} s. Furthermore, the values were recorded using Matlab's `long` precision format. Also, note that the coordinate z is equal to $r = 0.05$ m for all impacts.

Table 8.2 shows a clear consistency between the analytical and numerical solutions; indeed, the observed differences are extremely small and do not exceed order 10^{-8} over the three

Table 8.1: Initial conditions for flat world simulations.

Parameter	Value
x_0	-80 m
z_0	20 m
$\dot{x}_0$	0.01 m/s
$\dot{z}_0$	-0.023 m/s
ω_0	0 rad/s
g	-10^{-4} m/s^2
e	0.5
f	0.6
C_{rr}	0.04
r	0.05 m

Table 8.2: Comparison of initial collision results.

	Analytical	Numerical	Difference
1st Impact			
t [s]	442.2350779**30332**	442.2350779**17576**	1.2756×10^{-08}
x [m]	-75.57764922 0**6967**	-75.577649220**8242**	1.2750×10^{-10}
$\dot{x}$ [m/s]	0.0057023534**04435**	0.0057023534**35642**	3.1207×10^{-11}
$\dot{z}$ [m/s]	0.03361175389**6517**	0.03361175389**5879**	6.3800×10^{-13}
ω [rad/s]	0.11404706**80887**	0.11404706**67568**	1.3319×10^{-09}
2nd Impact			
t [s]	1114.4701558**6066**	1114.4701558**1026**	5.0400×10^{-08}
x [m]	-71.7443272**3548**	-71.7443272**1484**	2.0637×10^{-08}
$\dot{x}$ [m/s]	0.0051273551**06653**	0.0051273551**3979**	3.3137×10^{-11}
$\dot{z}$ [m/s]	0.01680587694**8258**	0.01680587694**6695**	1.5630×10^{-12}
ω [rad/s]	0.1025471021**330**	0.102547099321**852**	2.8112×10^{-09}
3rd Impact			
t [s]	1450.5876948**2583**	1450.5876948**1677**	9.0602×10^{-09}
x [m]	-70.0209332**556314**	-70.0209332**236449**	3.1987×10^{-08}
$\dot{x}$ [m/s]	0.00486884600**9675**	0.00486884600**4662**	5.0130×10^{-12}
$\dot{z}$ [m/s]	0.00840293847**4129**	0.00840293847**6978**	2.8490×10^{-12}
ω [rad/s]	0.0973769201 9**3505**	0.097376919**1705**	1.0230×10^{-09}

initial impacts. It is concluded from this comparison that the numerical simulations of these first impacts work correctly.

As next verification and validation step, not the initial but rather the final impact is considered. For now, both the analytical and numerical models iterate bouncing until the normal velocity reaches below some specified limit $\dot{z} < \dot{z}_{min}$. Indeed, the virtual bounce described by Equation 8.15 will be considered further on in this chapter, but is at present ignored. This approach allows for a clear analysis of the workings of the virtual bounce. Table 8.3 displays, for various values of $\dot{z}_{min}$, the time and state of the ball after its respective final collision. The results were obtained using again the initial conditions listed in Table 8.1 and the aforementioned numerical accuracies.

Table 8.3 shows how the state of the ball and the final impact time converge towards some particular value as more and more collisions are taken into account with decreasing $\dot{z}_{min}$. The observed differences between the analytical and numerical models are again small, with the largest differences on the order of 10^{-6}. This proves that the numerical simulations correctly propagate impacts between the ball and the flat surface, down to any value of $\dot{z}_{min}$.

As final unit test of the collision modelling, the full impact model including the virtual bounce is considered, by applying once more the initial conditions of Table 8.1 to both analytical and numerical models. The results of this comparison are shown in Table 8.4, note how only the horizontal velocity $\dot{x}$ and rotation ω of the ball are shown, as all other values are equal to those shown in Table 8.3. Again, the numerical results are seen to be in agreement with the analytical solution, thereby proving that the former method was correctly implemented.

One final result set is now presented, to verify that the virtual bounce achieves the desired effect of representing the infinity of bounces. To this end, the numerical simulation results for different values of $\dot{z}_{min}$ are shown in Table 8.5, for both models with and without virtual bounce. Assuming that the simulation without virtual bounce at the lowest value of $\dot{z}_{min}$ approaches the true solution to an acceptable degree, it is possible to use this particular solution to verify the accuracy of the other numerical solutions. As such, Table 8.5 shows the difference of the tested numerical model variations with respect to the 'true' solution.

Table 8.5 clearly shows that a certain error remains when the virtual bounce is not taken into account, although it decreases with decreasing $\dot{z}_{min}$ and has a negligible magnitude even for the largest tested value of $\dot{z}_{min}$. When applying the virtual bounce, the error is further reduced by three orders of magnitude to completely negligible values on the order of 10^{-10}. From this it is argued that the virtual bounce indeed successfully captures the infinite series of bouncing in a finite number of computations.

Table 8.3: Comparison of final collision results without virtual bounce.

	Analytical	Numerical	Difference
Final impact for $\dot{z}_{min} = 10^{-3}$ m/s ($n_{\mathrm{imp}} = 7$)			
t [s]	1765.69788**60567**	1765.69788**89057**	2.8490×10^{-07}
x [m]	-68.5091495**515302**	-68.5091495**214147**	3.0116×10^{-08}
$\dot{x}$ [m/s]	0.00464207845**5406**	0.0046420784**36315**	1.7745×10^{-11}
$\dot{z}$ [m/s]	$5.2518365\mathbf{463}\times10^{-4}$	$5.2518365\mathbf{717}\times10^{-4}$	2.5395×10^{-12}
ω [rad/s]	0.09284156**9081201**	0.09284156**8719567**	3.6163×10^{-10}
Final impact for $\dot{z}_{min} = 10^{-5}$ m/s ($n_{\mathrm{imp}} = 13$)			
t [s]	1786.37699**400685**	1786.37699**483725**	8.3040×10^{-07}
x [m]	-68.4132531**541307**	-68.4132531**218547**	3.2276×10^{-08}
$\dot{x}$ [m/s]	0.00462769399**445**	0.00462769397**614**	1.8302×10^{-11}
$\dot{z}$ [m/s]	$8.20599\mathbf{46036}\times10^{-6}$	$8.20599\mathbf{98934}\times10^{-6}$	5.2898×10^{-12}
ω [rad/s]	0.092553879**889002**	0.092553879**521748**	3.6725×10^{-10}
Final impact for $\dot{z}_{min} = 10^{-7}$ m/s ($n_{\mathrm{imp}} = 20$)			
t [s]	1786.7026**6941768**	1786.7026**711913**	1.7736×10^{-06}
x [m]	-68.4117460**523361**	-68.4117460**157014**	3.6635×10^{-08}
$\dot{x}$ [m/s]	0.004627467**929181**	0.004627467**910027**	1.9154×10^{-11}
$\dot{z}$ [m/s]	$6.41\mathbf{09332840}\times10^{-8}$	$6.41\mathbf{10548079}\times10^{-8}$	1.2152×10^{-12}
ω [rad/s]	0.092549358**583619**	0.092549358**200528**	3.8309×10^{-10}
Final impact for $\dot{z}_{min} = 10^{-9}$ m/s ($n_{\mathrm{imp}} = 27$)			
t [s]	1786.70521**375683**	1786.70521**620551**	2.4487×10^{-06}
x [m]	-68.4117342**784898**	-68.4117342**387312**	3.9759×10^{-08}
$\dot{x}$ [m/s]	0.004627466**163104**	0.004627466**143301**	1.9803×10^{-11}
$\dot{z}$ [m/s]	$5.0\mathbf{08541628}\times10^{-10}$	$5.0\mathbf{46215238}\times10^{-10}$	3.7674×10^{-12}
ω [rad/s]	0.09254932**326208**	0.09254932**2866029**	3.9605×10^{-10}

Table 8.4: Comparison of final collision results with virtual bounce.

	Analytical	Numerical	Difference
Final impact for $\dot{z}_{min} = 10^{-3}$ m/s ($n_{\mathrm{coll}} = 8$)			
$\dot{x}$ [m/s]	0.004627450**791694**	0.004627450**773933**	1.7761×10^{-11}
ω [rad/s]	0.09254901**583388**	0.09254901**547196**	3.6193×10^{-10}
Final impact for $\dot{z}_{min} = 10^{-5}$ m/s ($n_{\mathrm{coll}} = 14$)			
$\dot{x}$ [m/s]	0.0046274661**4545**	0.0046274661**2701**	1.8448×10^{-11}
ω [rad/s]	0.092549322**909169**	0.092549322**538995**	3.7017×10^{-10}
Final impact for $\dot{z}_{min} = 10^{-7}$ m/s ($n_{\mathrm{coll}} = 21$)			
$\dot{x}$ [m/s]	0.0046274661**4919**	0.0046274661**3001**	1.9188×10^{-11}
ω [rad/s]	0.092549322**983953**	0.092549322**600187**	3.8377×10^{-10}
Final impact for $\dot{z}_{min} = 10^{-9}$ m/s ($n_{\mathrm{coll}} = 28$)			
$\dot{x}$ [m/s]	0.004627466**149198**	0.004627466**129291**	1.9907×10^{-11}
ω [rad/s]	0.092549322**983957**	0.092549322**585815**	3.9814×10^{-10}

Table 8.5: Comparison of numerical final collision results with and without virtual bounce.

	Without V_∞	With V_∞	$\Delta_{\text{True}-\text{Without}}$	$\Delta_{\text{True}-\text{With}}$
Final impact for $\dot{z}_{min} = 10^{-3}$ m/s				
$\dot{x}$ [m/s]	0.00464**2078436315**	0.0046274**50773933**	1.4612×10^{-05}	1.5369×10^{-08}
ω [rad/s]	0.092**841568719567**	0.0925**4901547196**	2.9225×10^{-04}	3.0739×10^{-07}
Final impact for $\dot{z}_{min} = 10^{-5}$ m/s				
$\dot{x}$ [m/s]	0.004627**693976148**	0.00462746612**2701**	2.2783×10^{-07}	1.6291×10^{-11}
ω [rad/s]	0.0925**53879521748**	0.092549322**538995**	4.5567×10^{-06}	3.2703×10^{-10}
Final impact for $\dot{z}_{min} = 10^{-7}$ m/s				
$\dot{x}$ [m/s]	0.00462746**7910027**	0.00462746613**001**	1.7667×10^{-09}	1.3291×10^{-11}
ω [rad/s]	0.0925493**58200528**	0.092549322**600187**	3.5334×10^{-08}	2.6584×10^{-10}
(True) Final impact for $\dot{z}_{min} = 10^{-9}$ m/s				
$\dot{x}$ [m/s]	0.004627466143301	0.0046274661**29291**	ø	1.4010×10^{-11}
ω [rad/s]	0.092549322866029	0.0925493225**85815**	ø	2.8021×10^{-10}

One also realizes from Table 8.5 that a regularization velocity of $\dot{z}_{min} = 10^{-5}$ m/s is sufficient to obtain the highest accuracy possible. Indeed, further lowering this velocity would result in a far larger number of bounces to be taken into account (as shown in Table 8.3), yet fail to reduce the error below 10^{-10}. As such, the regularization velocity of $\dot{z}_{min} = 10^{-5}$ m/s will be applied in any future simulations of this research. This concludes the full verification and validation of the collision handling software, which has been proven to work correctly and as designed.

8.3 Rolling

Upon completing the infinite series of impacts discussed in the previous section, the ball will transition into a regime of rolling motion where instead of experiencing impulsive forces and torques, it will be continuously at bay of these contact interactions.

Indeed, the normal, friction and rolling resistance forces and torques shown in Figure 8.2 act on the system at all times, and the ball no longer demonstrates any vertical motion with respect to the flat surface. The verification and validation of this rolling motion is the subject of the present section, and will be detailed in a manner similar to that of the previous section.

8.3.1 Analytical Results

In accordance with their definition in Section 4.4, the friction force and related torque act on the ball only when the velocity of its contact point on the flat surface $V_H = \dot{x} - \omega r \neq 0$. This condition holds whenever the ball's velocity and rotation are *not* synchronized, or $\dot{x} \neq \omega r$ at some t_0. Indeed, as discussed in Section 4.4, the friction force and torque serve to drive the ball into this synchronization at t_s. Applying their definition as given in Section 4.4, the change in velocity and rotation of the ball as a result of the friction force and torque may be given as:

$$\text{Friction} \quad \Rightarrow \; \forall t < t_s : \begin{cases} \ddot{x} = -fg \\ \dot{\omega} = -\frac{5fg}{2r} \end{cases} \quad \forall t > t_s : \begin{cases} \ddot{x} = 0 \\ \dot{\omega} = 0 \end{cases} \tag{8.16}$$

Analogously, the change in velocity and rotation rate resulting from the rolling resistance force and torque may be determined by:

$$\text{Rolling resistance } \Rightarrow \begin{cases} \ddot{x} = -\frac{5C_{rr}g}{2} \\ \dot{\omega} = -\frac{5C_{rr}g}{2r} \end{cases} \tag{8.17}$$

These accelerations acts during the ball's *entire* motion. Assuming now that the velocity and rotation of the ball are indeed *not* synchronized at some time $t_0 = 0$, they may be computed as a function of time by:

$$\forall t < t_s : \begin{cases} \dot{x}(t) = \dot{x}_0 + \ddot{x}t \\ \omega(t) = \omega_0 + \dot{\omega}t \end{cases} \tag{8.18}$$

It is now possible to compute the synchronization time t_s by setting $\dot{x}(t_s) = \omega(t_s)r$ and substituting Equations 8.16 through 8.18. The time t_s is then obtained as:

$$t_s = \frac{-2(\dot{x}_0 - \omega_0 r)}{7fg} \tag{8.19}$$

Furthermore, the position and velocity of the ball in $[t_0, t_s]$ are described by the following equations of motion:

$$\forall t < t_s : \begin{cases} x(t) = x_0 + \dot{x}_0 t + \frac{1}{2}g(f + \frac{5}{2}C_{rr})t^2 \\ \omega(t) = \omega_0 + \frac{5}{2}gr(C_{rr} - f)t \end{cases} \tag{8.20}$$

Once this synchronization has occurred, the velocity of the contact point $V_H = 0$, and friction will no longer act on the ball. The subsequent motion is therefore influenced *only* by rolling resistance. The velocity and rotation of the ball in this regime may be described, applying Equations 8.17, as:

$$\begin{cases} \ddot{x} = \frac{5}{2}gC_{rr} \\ \dot{\omega} = \frac{5gC_{rr}}{2r} \end{cases} \tag{8.21}$$

Assuming now that the initial velocity and rotation rate of the ball have some non-zero value at time t_s, it is possible to calculate the stopping time t_{end} of the ball using Equation 8.18 by setting $\dot{x}(t_{end}) = 0$, as:

$$t_{end} = -\frac{2\dot{x}_0}{5gc_{rr}} + t_s \tag{8.22}$$

Finally, the position and rotation of the ball in the regime $[t_s, t_{end}]$, governed purely by rolling resistance, may be described by the following equations of motion:

$$\begin{cases} x(t) = x_0 + \dot{x}_0 + \frac{5}{4}gC_{rr}t^2 \\ \omega(t) = \omega_0 + \frac{5gC_{rr}}{2r}t \end{cases} \tag{8.23}$$

8.3.2 Numerical Simulations

By using the aforementioned equations, it is now possible to construct analytical solutions to the uni-axial rolling motion of a ball on a flat surface in a uniform gravity field. By comparing these solutions with results from the numerical simulations, it is possible to verify and validate that part of the software that handles such contact motion. As primary test, the ball is released from the same initial position and velocity used in the previous section, as shown in Table 8.1. However, the coefficient of restitution e is set to zero, and all effects from friction and rolling resistance are ignored during bouncing motion. As a result, the ball will dissipate all of its normal velocity $\dot{z}$ on first impact, and immediately start contact motion. Furthermore, since $f = C_{rr} = 0$ during that bounce, the rotation of the ball will remain unaffected by the impact and be equal to zero when contact motion is initiated. Applying this (physically unrealistic[1]) approach allows for a clear verification and validation of the regime of contact motion where friction drives the ball's velocity and rotation rate into synchronization and, subsequently, of the regime where rolling resistance draws both to zero. Table 8.6 contains results from both analytical numerical models obtained for different values of the regularization velocity, together with the difference between these numerical cases and the analytical solution. This table shows how the numerical results are in agreement with the analytical solution, and converge more closely as the regularization velocity is decreased. This proves that the software correctly simulates the ball's rolling motion, although the inherent error is larger than was the case for the bouncing motion. This is expected, as the analytical model does not require the application of regularization velocities, which are unrepresentative of true physical phenomena. Nevertheless, the implied position error is of order 10^{-5} m for the previously selected regularization velocity of $\dot{z}_{min} = 10^{-5}$ m/s, which is of the acceptable sub-millimeter order.

Finally, the full motion with all contact forces and torques active during contact motion is investigated, again for different values of the regularization velocities. Analytical and numerical results for this situation are shown in Table 8.7. It is once more observed that the numerical

---

[1] In reality, friction draws the ball's velocity and rotation into synchronization during the bounces, yielding that $t_s = 0$.

Table 8.6: Comparison of trajectory results with ineffective $e/C_{rr}/f$ during bouncing.

	Analytical	Numerical	Difference	Numerical	Difference	Numerical	Difference
		$V_{reg} = 10^{-4}$ m/s		$V_{reg} = 10^{-5}$ m/s		$V_{reg} = 10^{-6}$ m/s	
t_f [s]	442.235077930332	442.235077917**575**	1.2757×10^{-08}	442.235077917**575**	1.2757×10^{-08}	442.235077917**575**	1.2757×10^{-08}
x_f [m]	-75.5776492206966	-75.5776492208**242**	1.2760×10^{-10}	-75.5776492208**242**	1.2760×10^{-10}	-75.5776492208**242**	1.2760×10^{-10}
t_s [s]	489.85412554938	4**90.600745876312**	7.4662×10^{-01}	489.**934104354938**	7.9979×10^{-02}	489.8**63436141683**	9.3106×10^{-03}
x_s [m]	-75.1808238238712	-75.1**758351583033**	4.9887×10^{-03}	-75.180**2897503926**	5.3407×10^{-04}	-75.180**7616665092**	6.2157×10^{-05}
$\dot{x}_s$ [m/s]	0.006666666666667	0.00666**1562007506**	5.1047×10^{-06}	0.006666**080774254**	5.8589×10^{-07}	0.006666**590254752**	7.6412×10^{-08}
ω_s [rad/s]	0.133333333	0.133**077839047783**	2.5549×10^{-04}	0.1333**07899155123**	2.5434×10^{-05}	0.13333**0765582525**	2.5674×10^{-06}
t_{end} [s]	1156.52079221605	11**60.99787618283**	4.4771×10^{0}	1156.**85008523774**	3.2929×10^{-01}	1156.5**3813205968**	1.7340×10^{-02}
x_{end} [m]	-72.9586016016491	-72.958**4720667853**	1.2953×10^{-04}	-72.958**5887187504**	1.2883×10^{-05}	-72.95860**03014068**	1.3002×10^{-06}

Table 8.7: Comparison of trajectory results with full bouncing.

	Analytical	Numerical	Difference	Numerical	Difference	Numerical	Difference
		$V_{reg} = 10^{-4}$ m/s		$V_{reg} = 10^{-5}$ m/s		$V_{reg} = 10^{-6}$ m/s	
t_{end} [s]	2249.1236085527	22**52.96969279801**	3.8461×10^{0}	2249.**42005911822**	2.9645×10^{-01}	2249.1**4215782108**	1.8549×10^{-02}
x_{end} [m]	-67.342581007762	-67.3425**797347554**	1.2730×10^{-06}	-67.34258**0971544**	3.6218×10^{-08}	-67.34258**09839146**	2.3847×10^{-08}

results are in agreement with the analytical solution, and again have a negligible position error of 10^{-8} for the selected regularization velocity. Although the time error is roughly 0.3 seconds, it is argued that this error, too, is negligible considering the total simulation time of approximately 2500 seconds. As such, the numerical implementation of contact motion has been verified and validated and can be used to produce high-fidelity simulations.

8.3.3 Extended Flat-World Motion

The simulations considered in the previous sections were performed at relatively low velocities, for which the motion of the ball does not extend beyond a single facet. To verify that the software is indeed capable of carrying out motion spanning multiple facets, a visual analysis is performed for ball motion on the flat world at higher velocities. Analogous to the strategy employed in the previous section, the effects of friction and rolling resistance during the bounce are ignored, so as to be able to distinguish the effects from both forces during rolling motion. The applied initial conditions and parameters are shown in Table 8.8.

The resulting numerically simulated motion for these initial conditions is shown in Figure 8.3a; it is noted that the ball comes to a stop at approximately 3,060 seconds at position $[68.7693, 31.2616, 0.0500]$ m. The altitude of the ball, corresponding to its z-coordinate, is shown in Figure 8.3b. These two figures clearly show how the ball reaches a lower maximum altitude after each successive bounce, until it is forced in contact motion where its altitude remains constant and equal to $r = 0.05$ m.

Figures 8.3c and 8.3d show the velocity of the ball and of the contact point between the ball and the flat surface, respectively. Inspecting the ball's velocity, the effects of the successive impacts and intermediate parabolic arcs are clearly observed. The linear velocity behavior between approximately 1,900 and 2,200 seconds corresponds to the regime of contact motion where the velocity is reduced and transferred into rotation, until the two reach synchronization. Once this occurs, the linear slope of the velocity changes as rolling resistance becomes the only force acting on velocity, and eventually drives the ball's velocity to zero. This matches the observed behavior of the contact point velocity, which is drawn to zero by friction, and maintains that value throughout the rolling resistance-dominated regime. For clarity, the three successive flying/friction/rolling resistance regimes are marked by respectively blue, yellow and red backgrounds in both figures. Complementary to these velocity plots is the time history of the ball's rotation, as shown in Figure 8.4a. In this figure, the effects of friction and rolling resistance are clearly distinguishable in the respective increase and decrease of the rotation.

To further analyze the motion of the ball, several of energy plots have also been constructed.

Table 8.8: Initial conditions for extended flat world simulations.

Parameter	Value
x_0	-50 m
y_0	-40 m
z_0	40 m
$\dot{x}_0$	0.05 m/s
$\dot{y}_0$	0.03 m/s
$\dot{z}_0$	-0.07 m/s
ω_0	0 rad/s
g	-10^{-4} m/s^2
e	0.4
f	0.8
C_{rr}	0.15
r	0.05 m

Figure 8.4b shows the variation of the total energy of the ball, where the successive collisions produce the expected instantaneous drops in energy. Furthermore, one also observes the predicted drop in total energy in the yellow, friction-dominated regime resulting from the imperfect conversion from kinetic to rotational energy. Finally, the purple, rolling resistance regime illustrates how the rolling resistance force and torque reduce the total energy of the system until the ball comes to a full stop with zero rotation.

The total energy of the ball may be separated into potential, kinetic and rotational energy, as plotted respectively by Figures 8.4c, 8.4d and 8.4e. These figures, too, match the ball's expected and observed behavior. The potential energy fluctuates during the bouncing motion, and remains constant during rolling. The kinetic energy displays similar fluctuations between collisions, and instantaneous jumps at the collision epochs, which match the velocity jumps shown in Figure 8.3c. The energy dissipation during the friction and rolling resistance regimes is also visible. The rotational energy is zero until contact motion starts, as expected since neither friction nor rolling resistance effects are currently taken into account during bouncing. Once contact motion is initiated, the rotational energy is first seen to increase and then decrease, matching the observed variation in rotation shown in Figure 8.4a. Finally, Figure 8.4f plots all of these energies versus their final value, which visualizes the expected energy exchanges during bouncing and rolling motion. It can be seen from these figures that the software is indeed capable of handling the transfer of the ball between adjacent facets of the flat world.

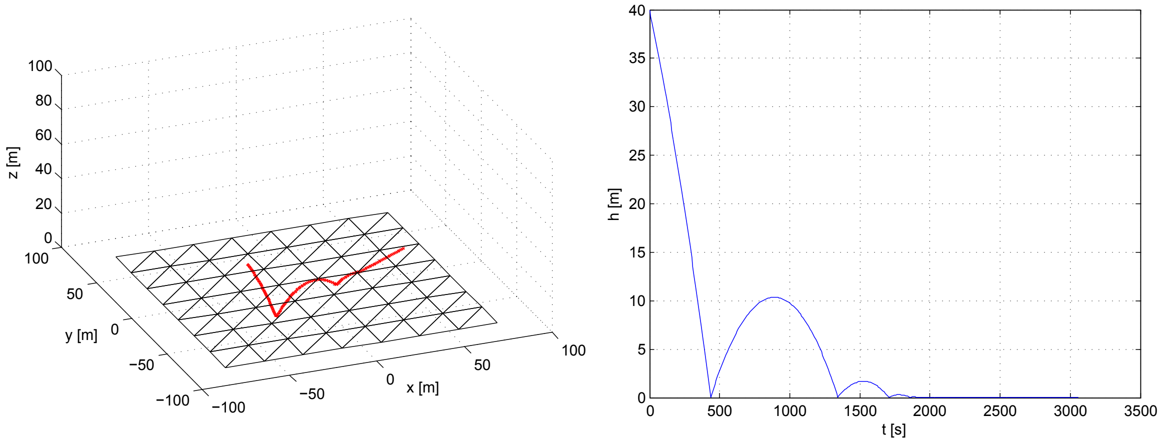

(a) Trajectory. **(b)** Altitude.

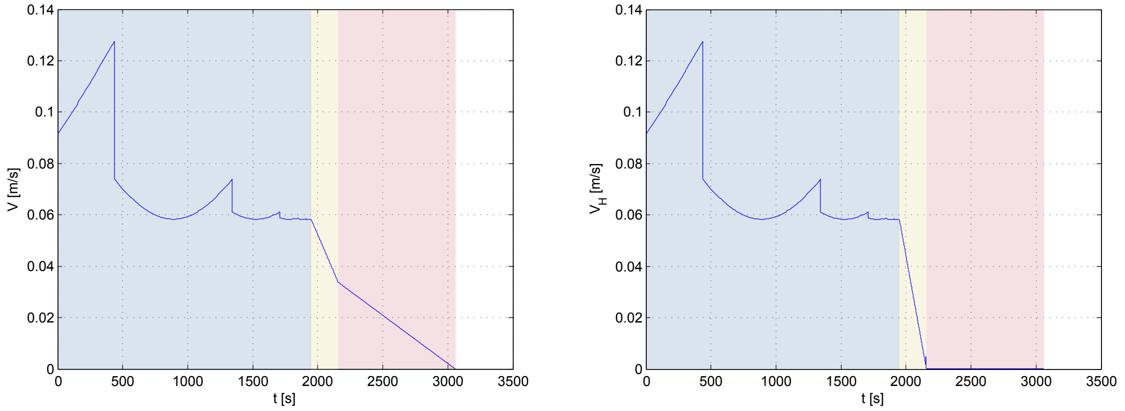

(c) Velocity. **(d)** Contact point velocity.

Figure 8.3: Results for extended-flat world motion.

8.4 Motion on Relief Worlds

The previous sections have considered the motion of a lander pod on a perfectly flat world. We now expand our V&V to worlds that are topographically more irregular to analyze our software's handling of those more complex situations.

8.4.1 Table World

As primary 'relief' world, consider the collection of facets shown in Figure 8.5. This world is similar in size to the flat world used in the previous sections, but features a vertical drop along the y-axis of roughly 16 meters near $x = -10$ m. We call this world the *table* world.

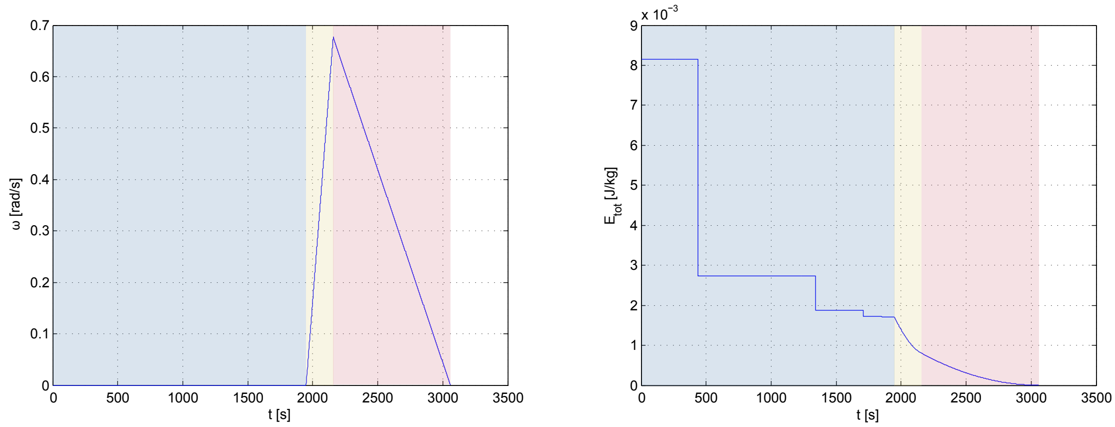

(a) Rotation rate.

(b) Total energy.

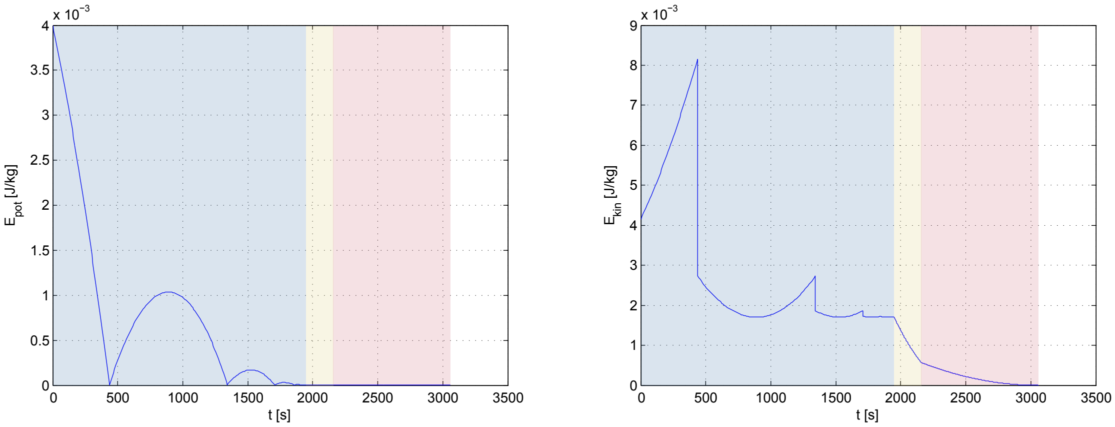

(c) Potential energy.

(d) Kinetic energy.

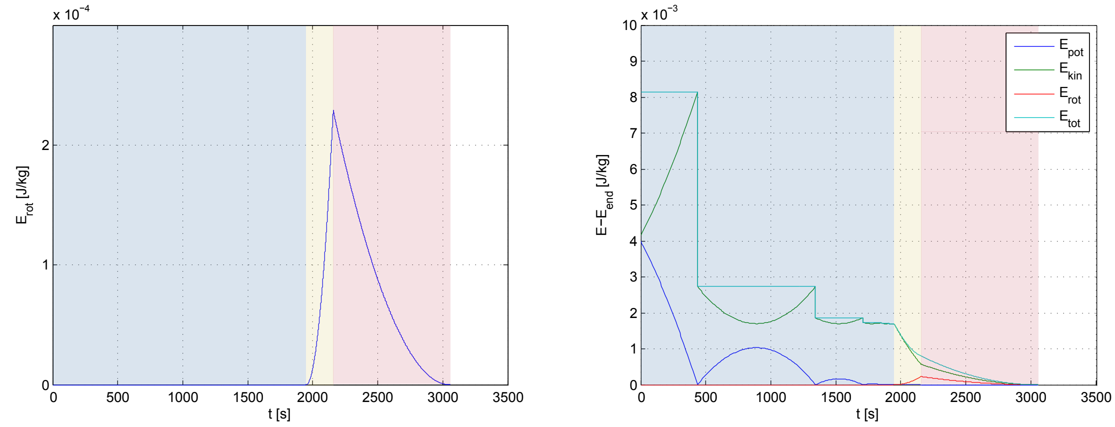

(e) Rotational energy.

(f) Energy comparison.

Figure 8.4: Continued results for extended-flat world motion.

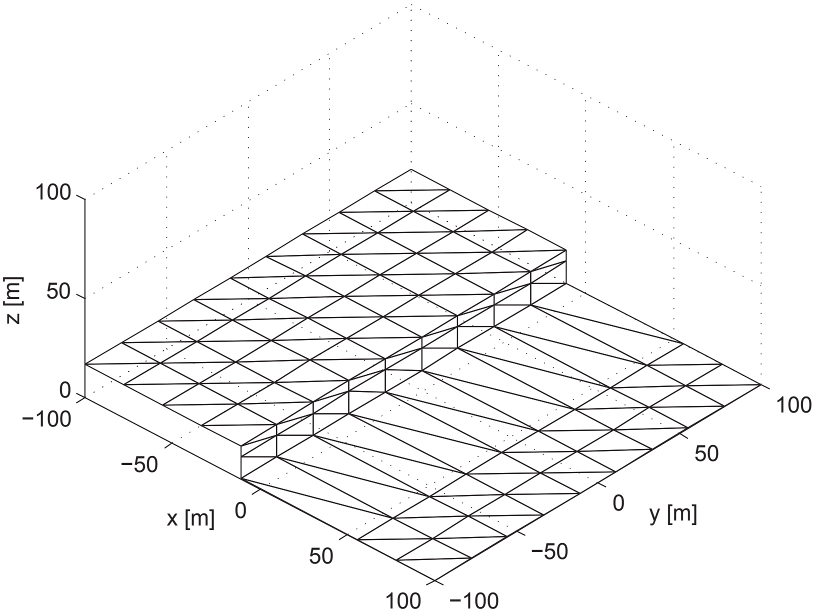

Figure 8.5: Table world used in contact motion V&V.

Motion on an Edge

Prior to reviewing global motion on this table world, a particular and unique validation point may be constructed for the case where the ball slowly rolls off the 'cliff'. In this case, it is assumed that the ball has zero velocity V and rotation ω when it is directly above the ledge, represented by situation '0' in Figure 8.6. If the ball is then given an infinitesimally small velocity, it will move towards the vertical drop and start to be pulled down by gravity. The ball then rolls on the edge between the horizontal and vertical facet, as shown by situation '1', until separation occurs at some angle θ_{esc}, see situation '2'. If the coefficient of friction f between the ball and the edge is sufficiently high to guarantee continuous synchronization of velocity and rotation, it is possible to derive an analytical expression for this θ_{esc}. Using the principle of conservation of energy, it is possible to equate the total energy of the ball at situations '0' and '1' as[2]:

$$E_{pot,0} = E_{pot,1} + E_{kin,1} + E_{rot,1} \quad \Leftrightarrow \quad gr = gr\cos\theta + \frac{1}{2}V^2 + \frac{1}{2}\bar{I}\omega^2 \tag{8.24}$$

If f is indeed sufficiently high to guarantee synchronization between the ball's velocity and rotation, they will be related to reach other through:

$$V = \omega r \tag{8.25}$$

---

[2] Both kinetic and rotational energy are zero in situation '0' as the ball does not possess any velocity or rotation.

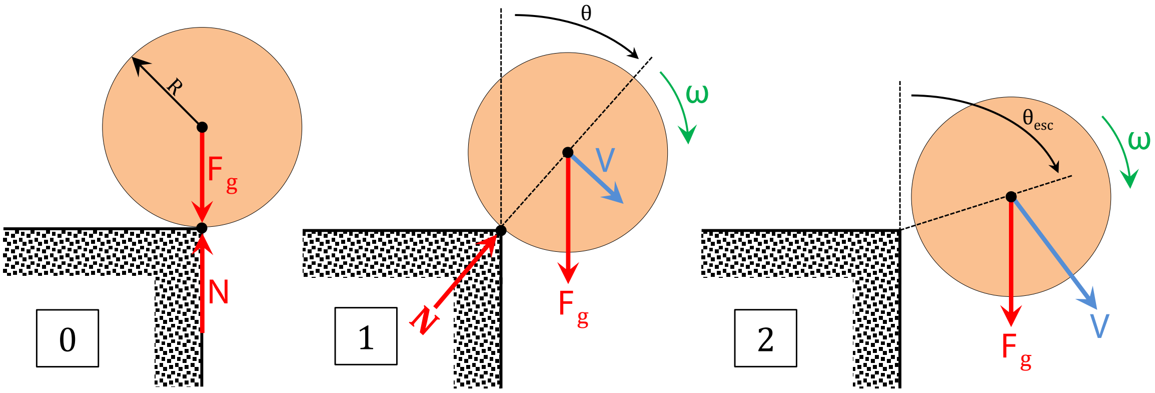
R
F g
N
0
θ
ω
V
1
F g
N
θesc
ω
V
2
F g

Figure 8.6: Illustrated motion of a ball rolling off a vertical edge.

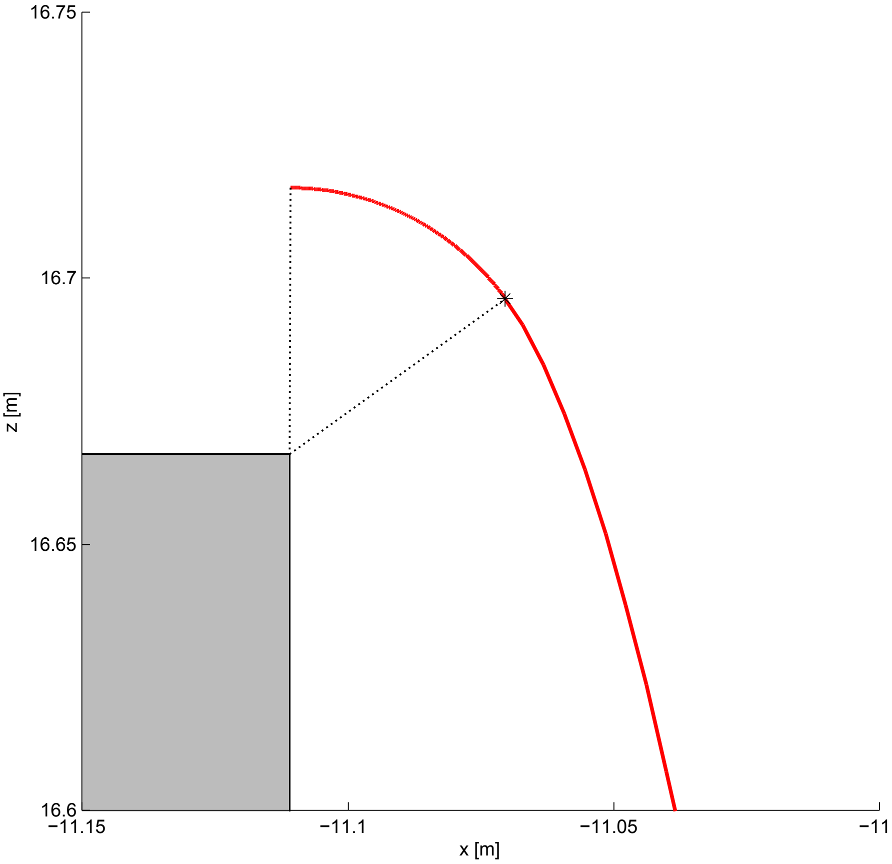

Figure 8.7: Simulated motion of a ball rolling off a vertical edge.

Furthermore, as presented in Section 4.4, the acceleration produced by the normal force on a ball rolling on an edge is given by:

$$N = \dot{\theta} r^2 - g \cos\theta \tag{8.26}$$

The ball will exit the edge and continue contact-less ballistic flight as soon as the normal force $N = 0$, which can be stated using Equation 8.26 as:

$$\dot{\theta}^2 r = g \cos\theta \tag{8.27}$$

One realizes from Figure 8.6 that $\dot{\theta} = \omega$, allowing for Equation 8.27 to be rewritten as:

$$\omega^2 r = g \cos\theta \tag{8.28}$$

It is now possible to obtain an expression for the release angle θ_{esc} by substituting Equations 8.25 and 8.28 into Equation 8.24 and rewriting the result as:

$$\cos\left(\theta_{esc}\right) = \frac{2}{3 + j} \tag{8.29}$$

In this equation, the massless inertia $\bar{I} = jr^2$ of the ball was substituted, with $j = 2/5$ for a ball with homogeneous mass distribution. By applying the arccosine, the angle θ can finally be computed as:

$$\theta_{esc} \simeq 53.968^\circ \tag{8.30}$$

It is therefore concluded that when a ball is pushed over an edge with infinitesimal initial velocity, and if friction is sufficiently high, it will leave the edge and continue to move away when the angle between the local normal direction and the center of the ball exceeds an angle of $\sim 54^\circ$. By numerically simulating this case using the developed software, it is possible to validate the software's correct handling of motion along an edge.

To indeed simulate this case, the ball was placed directly above the edge and given a velocity of 10^{-4} m/s toward the drop. The resulting trajectory is shown, in the XZ-plane of the table world, in Figure 8.7. In this figure, the position at which the ball ceases contact with the edge is marked by a star and has XZ-coordinates $[-11.0703, 16.6961]$ m. The angle θ of this point with respect to the vertical, as defined in Figure 8.6, was computed as $\theta = 54.4166^\circ$, where a friction coefficient of $f = 50$ was applied[3]. The small remaining difference of $\sim 0.4^\circ$ is attributed to the application of regularization applied to the small velocities involved in this situation; it is therefore concluded that the software correctly handles the motion of a ball rolling off a vertical edge.

---

[3] Although the theory outlined above applied infinite friction, using a very large friction coefficient would lead to numerical instabilities.

Global Motion

As mentioned at the start of this section, the example of a ball rolling off a vertical edge covers but a small portion of the total table world. Indeed, it is interesting to simulate bouncing and rolling motion across the entirety of this world, as was performed using the initial conditions and parameters shown in Table 8.9. Please note that all contact interactions are set to active during this simulation. The resulting trajectory is shown in Figure 8.8a. It can be seen from this figure that the ball first bounces on the 'upper' part of the world and eventually transitions into a rolling motion on this same surface. It then rolls off the vertical drop and bounces on the 'lower' part of the world, after which it briefly rolls on this surface and finally comes to a full stop. To illustrate this motion more clearly, Figure 8.8b shows the time history of the z-coordinate[4], where the bouncing and rolling segments are marked by respectively blue and red backgrounds.

The dichotomy between bouncing and rolling regimes is also clearly visible from Figure 8.8c, where the velocity of the ball is seen to fluctuate and instantaneously decrease during the former, and gets drawn to zero during the latter. The effects of friction are clearly visible in Figure 8.8d, which shows the contact point velocity as varying during bouncing motion and as constant zero during rolling motion, confirming the expected synchronization between the ball's velocity and rotation rate. Complementary to the velocity plots, Figure **??** illustrates the variation of the ball's rotation rate. This figure matches the change in velocity resulting from friction during rolling motion; one also observes the expected constant behavior during ballistic arcs, with instantaneous changes in rotation at every surface impact.

Table 8.9: Initial conditions for table world simulations.

Parameter	Value
x_0	-75.215 m
y_0	17.659 m
z_0	50.658 m
$\dot{x}_0$	0.0372 m/s
$\dot{y}_0$	-0.0156 m/s
$\dot{z}_0$	-0.0213 m/s
ω_0	0 rad/s
g	-10^{-4} m/s^2
e	0.55
f	0.85
C_{rr}	0.045
r	0.05 m

Reviewing the time history of the total energy of the ball as shown in Figure 8.8f, it displays instantaneous changes at every impact and remains constant during the intermediate ballistic

---

[4] For this world, the z-coordinate of the ball is equal to its altitude with respect to the 'lower' surface.

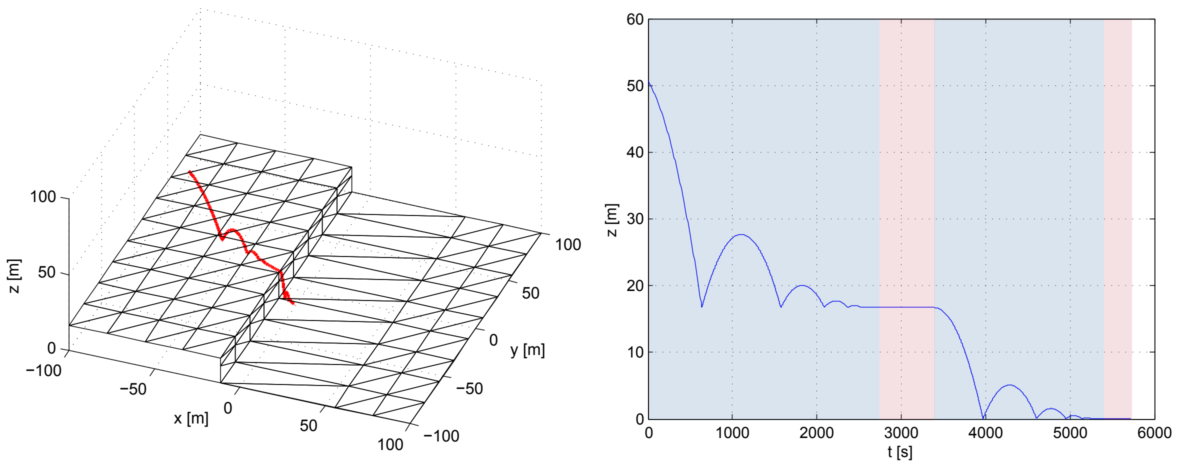

(a) Trajectory. **(b)** Altitude.

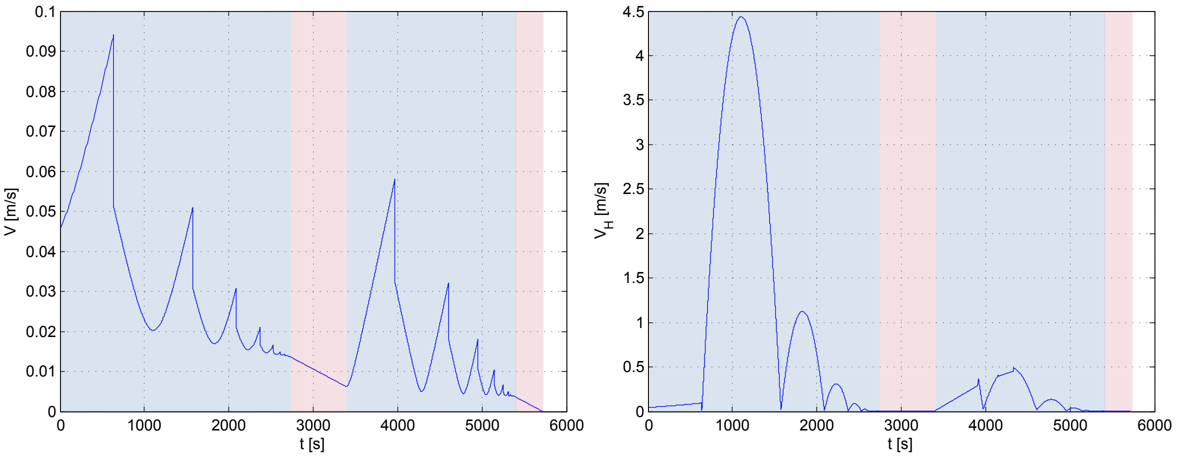

(c) Velocity. **(d)** Contact point velocity.

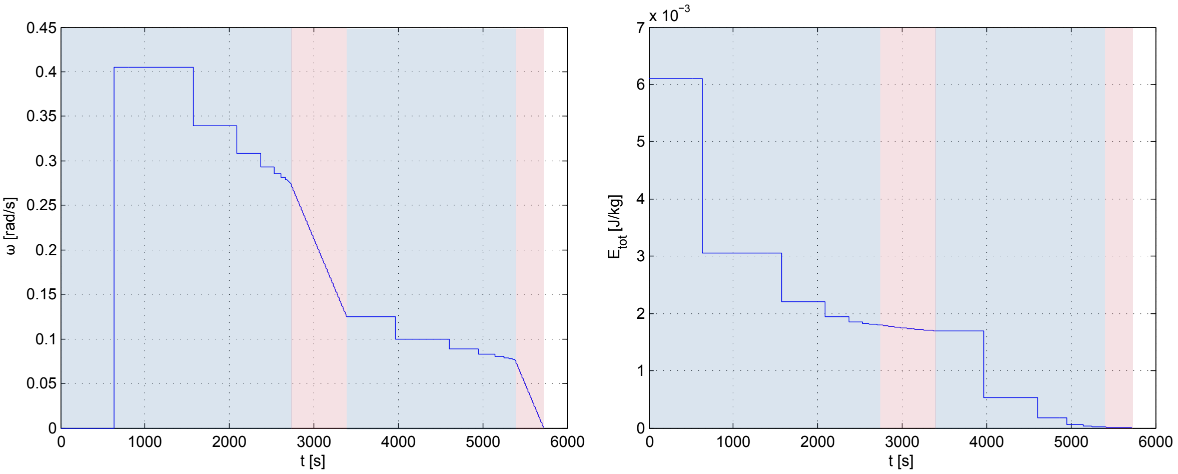

(e) Rotation. **(f)** Total energy.

Figure 8.8: Results for table world motion.

arcs. This behavior was anticipated, as was the decrease in total energy during rolling motion. Finally, the variations in potential, kinetic and rotational energy of the ball as shown in Figures 8.9a, 8.9b and 8.9c match the observed state of the ball and, too, show their respective expected variations with Figure 8.9d clearly expressing the energy exchanges that occur over the entire motion of the ball. It is concluded that the global motion of the ball on the table world is carried out correctly by the software.

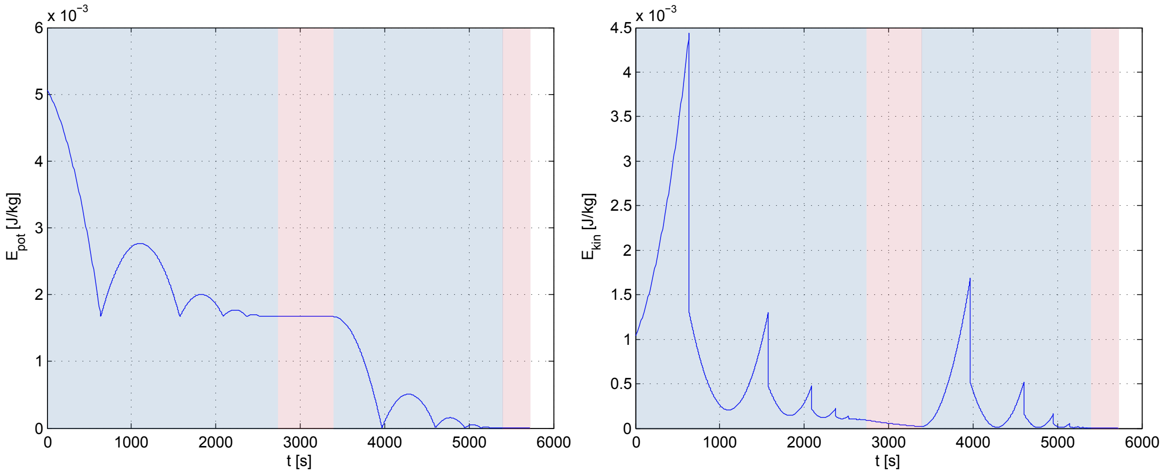

(a) Potential energy.

(b) Kinetic energy.

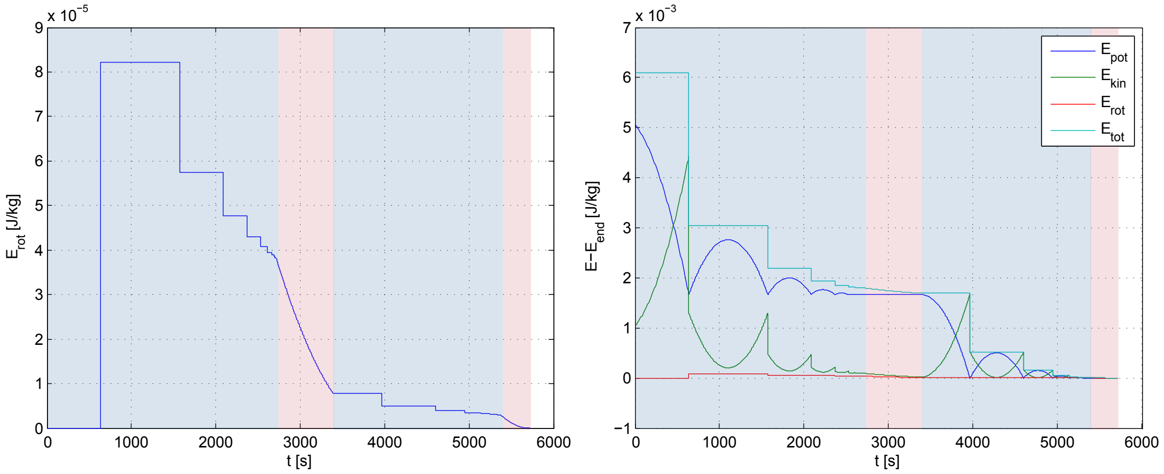

(c) Energy comparison.

(d) Contact point velocity.

Figure 8.9: Continued results for table world motion.

Impacting a Wall

A final V&V case occurs when the ball approaches the vertical wall along a rolling motion on the 'lower' surface, and subsequently impacts it. This situation is illustrated in Figure 8.10, where the ball is seen to roll towards the vertical wall on the right and impact it with a velocity V_0 and rotation ω_0. As a result of the normal, friction and rolling resistance impulses, the ball will convert some of its rotation into vertical velocity. Rather than bouncing back horizontally, it will therefore be thrown into the air and move away from the wall on a ballistic trajectory, eventually re-impacting the horizontal surface.

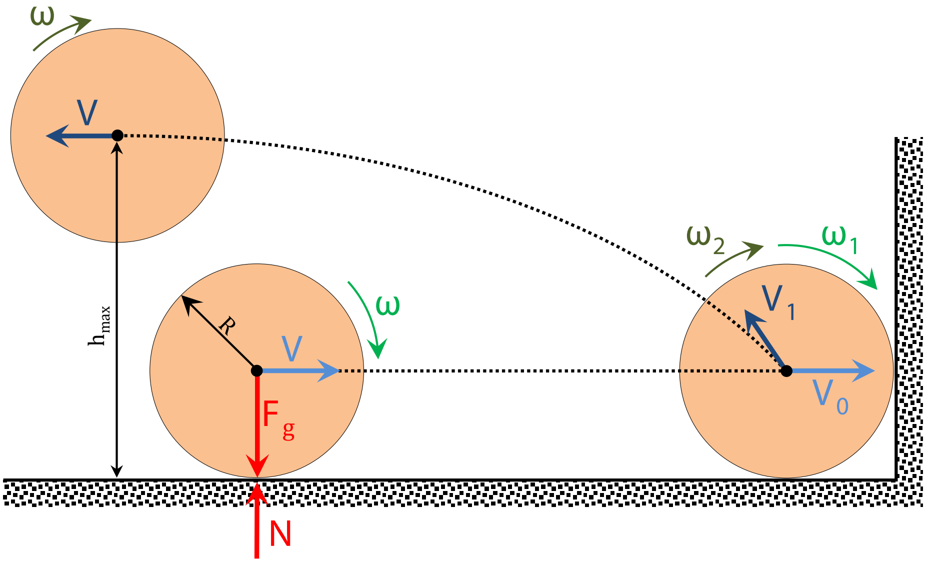

Figure 8.10: Illustration of a pod impacting a wall.

Not only can this particular case be simulated to visually verify whether it is carried out correctly, but it is also possible to construct an analytical solution to this motion, using the approach outlined in Section 8.2.1. To perform this verification and validation, a simulation is launched with initial conditions that have the ball impact the vertical wall during rolling motion. The applied initial conditions and parameters are shown in Table 8.10. An overview of the simulated motion is shown in Figure 8.11. One observes the ball bouncing on the 'lower' surface and transitioning into a rolling motion which impacts the vertical wall. Since the recoil motion is virtually impossible to distinguish at this scale, Figure 8.12 presents a detail of the motion in the immediate neighbourhood of the wall. Please note that the axes of this figure are shown such that the direction of motion of the ball corresponds with that illustrated in Figure 8.10.

The state of the ball just before the collision was retrieved from the simulated trajectory and entered into the analytical model. The resulting analytical post-impact state is shown in Table 8.11, together with the analytically computed maximum altitude h_{max} which the ball will reach along its first ballistic arc after the collision. This table also shows the same results as produced by the numerical simulation, allowing for the final verification and validation.

Table 8.10: Initial conditions for wall impact simulation.

Parameter	Value
x_0	75.0 m
y_0	17.659 m
z_0	15.0 m
$\dot{x}_0$	-0.0572 m/s
$\dot{y}_0$	0 m/s
$\dot{z}_0$	-0.0113 m/s
ω_0	0 rad/s
g	-10^{-4} m/s^2
e	0.55
f	0.85
C_{rr}	0.045
r	0.05 m

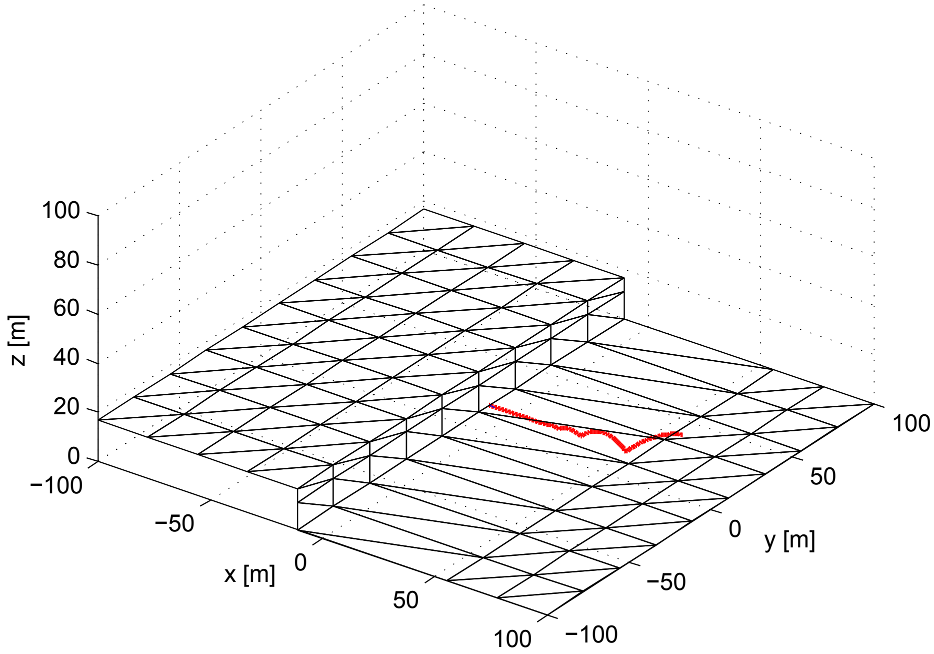

Figure 8.11: Simulated trajectory of a pod impacting a vertical wall.

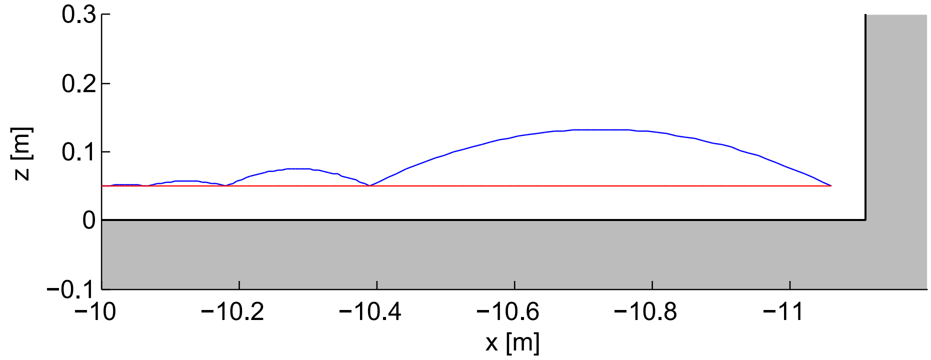

Figure 8.12: Detail of simulated trajectory of a pod impacting a vertical wall.

Table 8.11: Comparison of wall impact results.

	Analytical	Numerical	Difference
$\dot{x}$ [m/s]	0.008264117241**481**	0.008264117241**572**	9.2001×10^{-14}
$\dot{z}$ [m/s]	0.0040680835**89284**	0.00468083**564989**	6.1275×10^{-04}
ω [rad/s]	-0.08136167**178569**	-0.08136167**0295539**	1.4902×10^{-09}
h_{max} [m]	0.1327465**20447009**	0.1327465**15487654**	4.9594×10^{-09}

The simulated trajectory shown in Figure 8.12 matches the expected trajectory presented by Figure 8.10, where the ball's trajectory towards the wall is plotted in red, and the trajectory away from the wall is shown in blue. Indeed, the numerically simulated post-impact state of the ball matches the analytical solution, as can be read from Table 8.11. All cases of motion tested for the table world have shown the expected behavior; furthermore, the simulated motions correspond to the analytical solutions with only a negligible error remaining. It is therefore concluded that the software correctly handles all motion on the table world, justifying the continuation of contact motion validation on more complicated worlds that involve multi-contact situations.

8.4.2 Gutter World

To allow for V&V of such multi-contact cases, we have constructed the *gutter* world illustrated in Figure 8.13a, where the coloring of the facets is indicative of their vertical slope. The world features a gutter with both an inclined and a flat section, on which a pod may exhibit rolling motion while in contact with multiple facets. Analytical validation such motion is not possible, and we are therefore restricted to visual inspection of the trajectories and energy variations of the numerical simulations. We consider first the situation where the ball is released with a certain velocity above the inclined part of the gutter, resulting in the trajectory visible in Figure 8.13a. The initial conditions and parameters applied in this simulation are shown in Table 8.12. We observe the ball bouncing on the inclined surface and quickly transitioning into rolling motion, where gravity draws it onto the flat section of the gutter. There, the pod exhibits an oscillatory motion as its combined velocity and rotation alternatively make it roll and bounce on both sides of the gutter. The ball eventually comes to a stop after the aggregate of collisions and rolling resistance has removed all of its energy; the time history of the ball's energy exchange can be seen in Figure 8.14a.

A second trajectory is shown in Figure 8.13b, where the ball is released directly above the gutter, and displays the expected multi-contact motion as it rolls along the gutter, in contact with both sides. It eventually comes to a full stop while still touching two facets. The time history of the energy of this trajectory is also shown in Figure 8.14b. Again, the ball displays the expected motion, where we also observe that the transfer of the ball between neighbouring facets is handled correctly during multi-contact motion. It is noted that the pod had no initial rotation in either of the two simulations.

8.4.3 Pit World

Another investigation of multi-contact motion is performed on what we call the *pit* world, as shown in Figure 8.15a. The coloring of the facets is again representative of their vertical slope. This world features a center pit surrounded by tall peaks which force the ball to move into the pit, and allows us to verify that the ball correctly dissipates its energy and eventually comes to a stop at the bottom of the pit, in contact with three surface features.

Two trajectories on this world are presented, the first is shown in Figure 8.15a and is seen to bounce around the pit before coming to a stop at its bottom. The second trajectory, shown in Figure 8.15b is released more directly towards the center of the pit, and displays an oscillatory motion where it hops back and forth between two sets of facets. This trajectory,

Table 8.12: Initial conditions for gutter world simulations.

Parameter	Gutter 1	Gutter 2
x_0	-2.22 m	0.001 m
y_0	7.8 m	5.356 m
z_0	4.07 m	1.892 m
$\dot{x}_0$	-0.01 m/s	0 m/s
$\dot{y}_0$	0 m/s	0 m/s
$\dot{z}_0$	-10^{-6} m/s	-10^{-6} m/s
g	-10^{-4} m/s^2	-10^{-4} m/s^2
e	0.55	0.55
f	0.85	0.85
C_{rr}	0.045	0.045
r	0.05 m	0.05 m

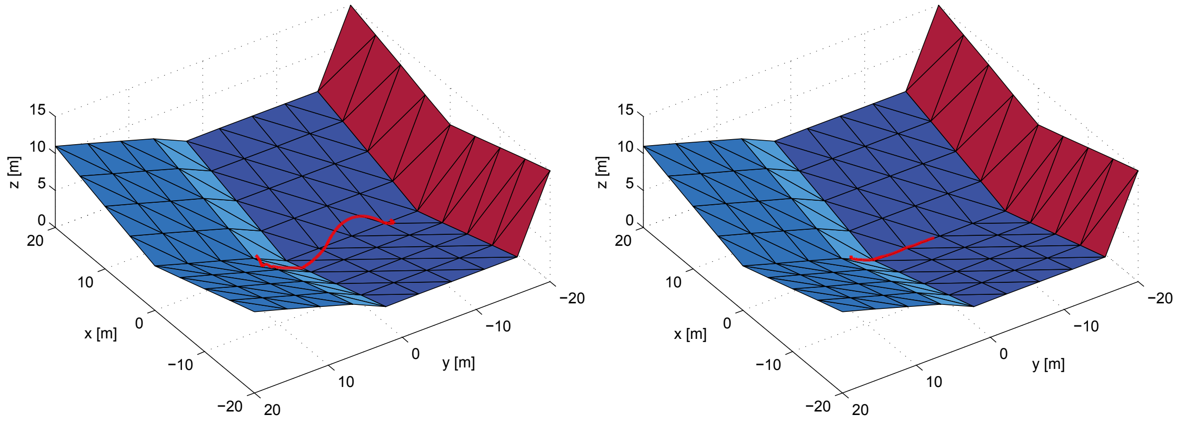

(a) Simulation 1. **(b)** Simulation 2.

Figure 8.13: Trajectories of gutter world simulations.

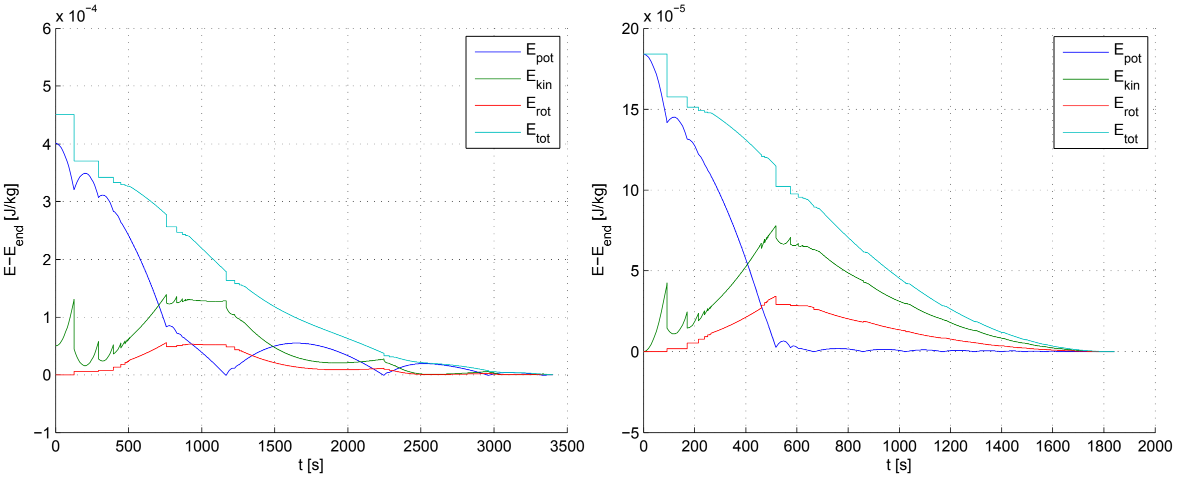

(a) Simulation 1. **(b)** Simulation 2.

Figure 8.14: Energy comparison of gutter world simulations.

too, eventually stops in the bottom of the pit. The energy exchanges of both simulations are shown in Figures 8.16a and 8.16b, respectively. The initial conditions and parameters applied in the simulations are included in Table 8.12.

8.4.4 Spike World

The final test for the contact motion module consists of simulations on the *spike* world, which is shown in Figure 8.18. This world is based on the flat world discussed in Section 8.1, but has random variations imposed on the z-coordinate of all but the outer points. This results in the highly irregular surface shown, and is an appreciable substitute for the types of topography encountered on an asteroid. A total of four simulated trajectories are shown, in Figures 8.18 through 8.20. The initial conditions and parameters for these simulations are included in

Table 8.12. All four simulations display the expected behavior, where the ball bounces and rolls around the world in a very random fashion, eventually coming to a stop in some lower region of the spike world. Not only do these simulations prove that the contact module works correctly and is capable of handling complex, multi-contact situations, but it also allows us to draw an important conclusion on the motion of a pod on irregular (asteroid) surfaces. Indeed, although all four trajectories occur on the same surface, they cover distinctly different distances over the spike world; as is especially visible when comparing Figures **??** and 8.20. This property of pod motion on irregular surface will be strongly reflected in trajectories simulated over a global asteroid model in the subsequent chapters. For now, it is concluded that the contact motion module has been fully verified and validated.

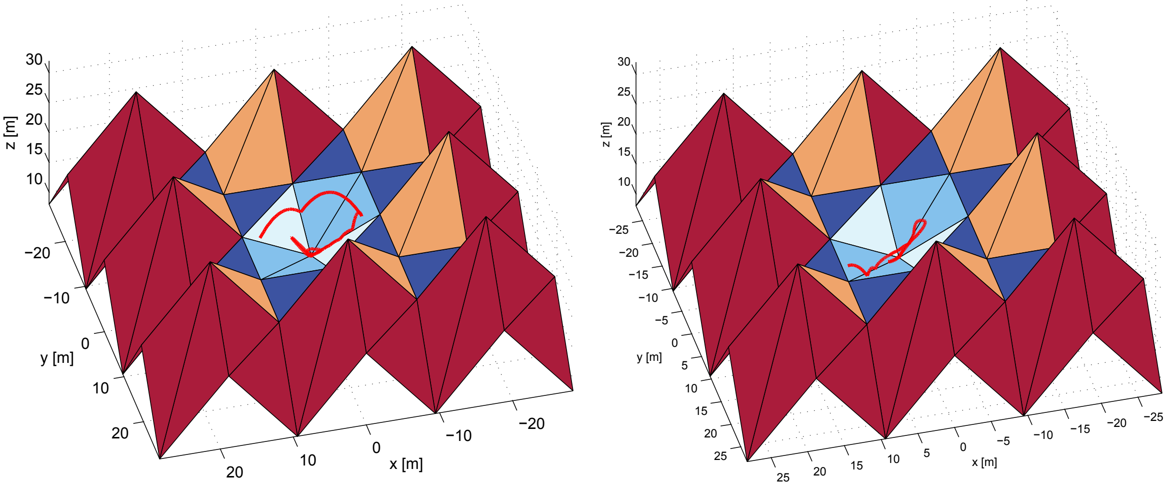

(a) Simulation 1. **(b)** Simulation 2.

Figure 8.15: Trajectories of pit world simulations.

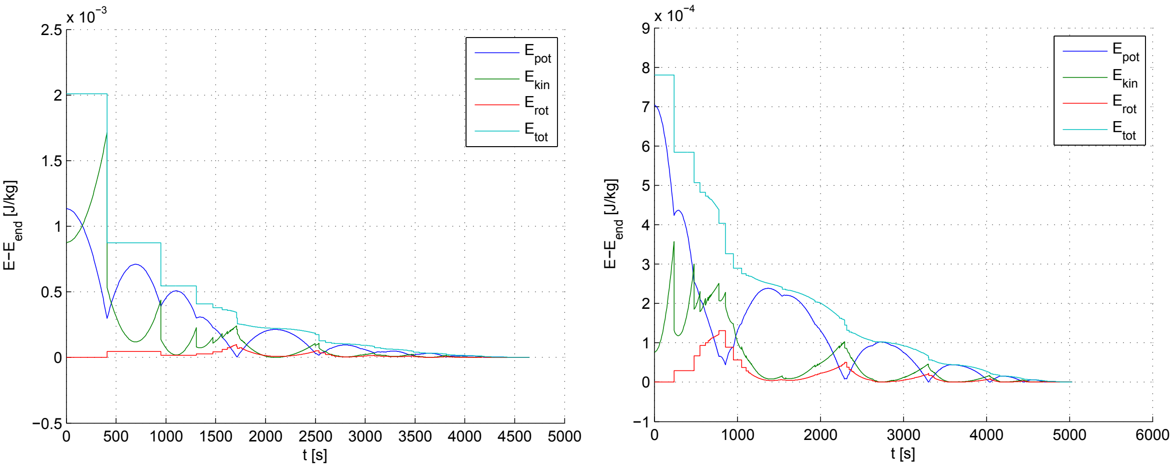

(a) Simulation 1. **(b)** Simulation 2.

Figure 8.16: Energy comparison of pit world simulations.

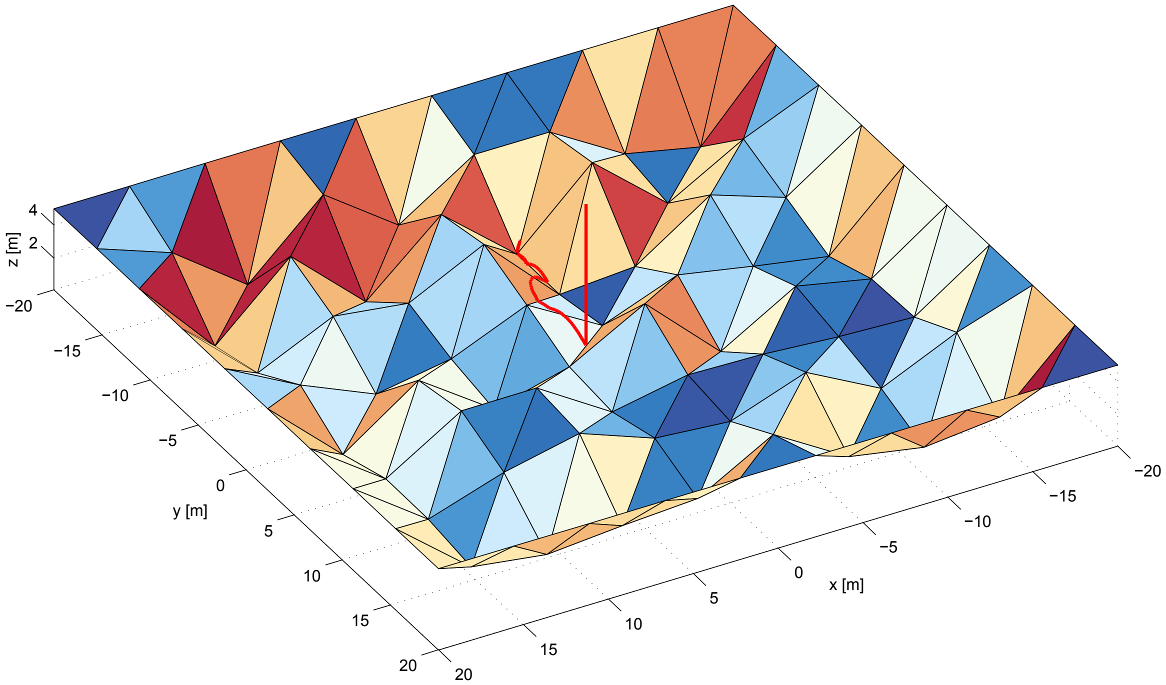

Figure 8.17: Simulated trajectory 1 on spike world.

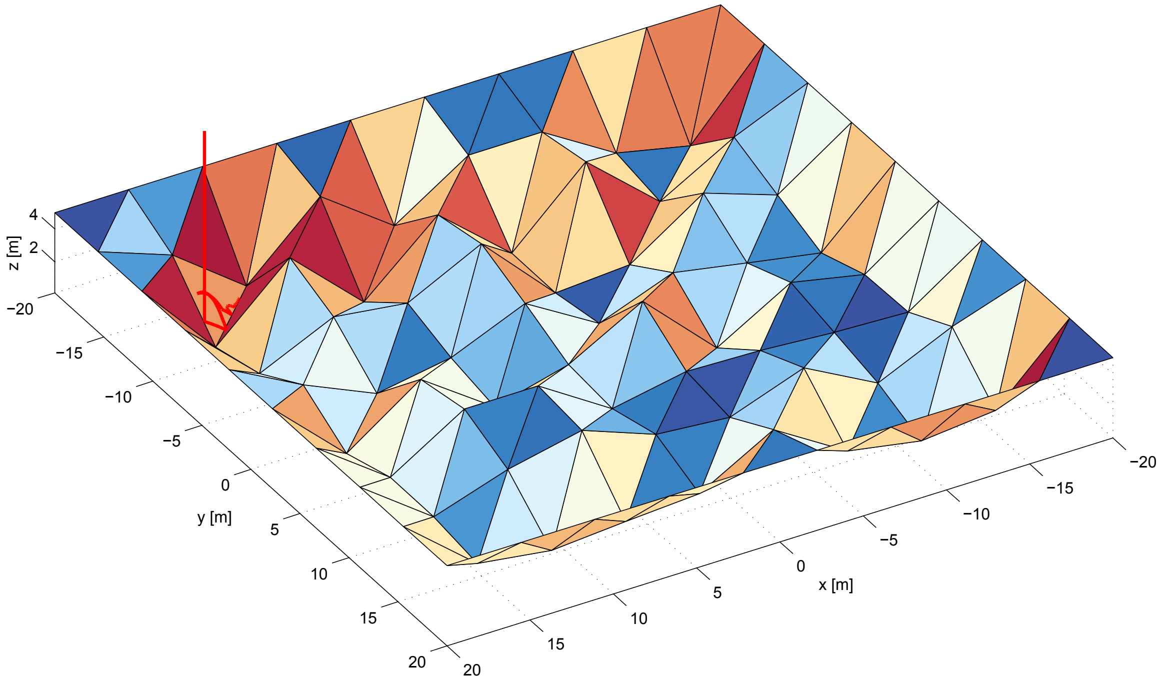

Figure 8.18: Simulated trajectory 2 on spike world.

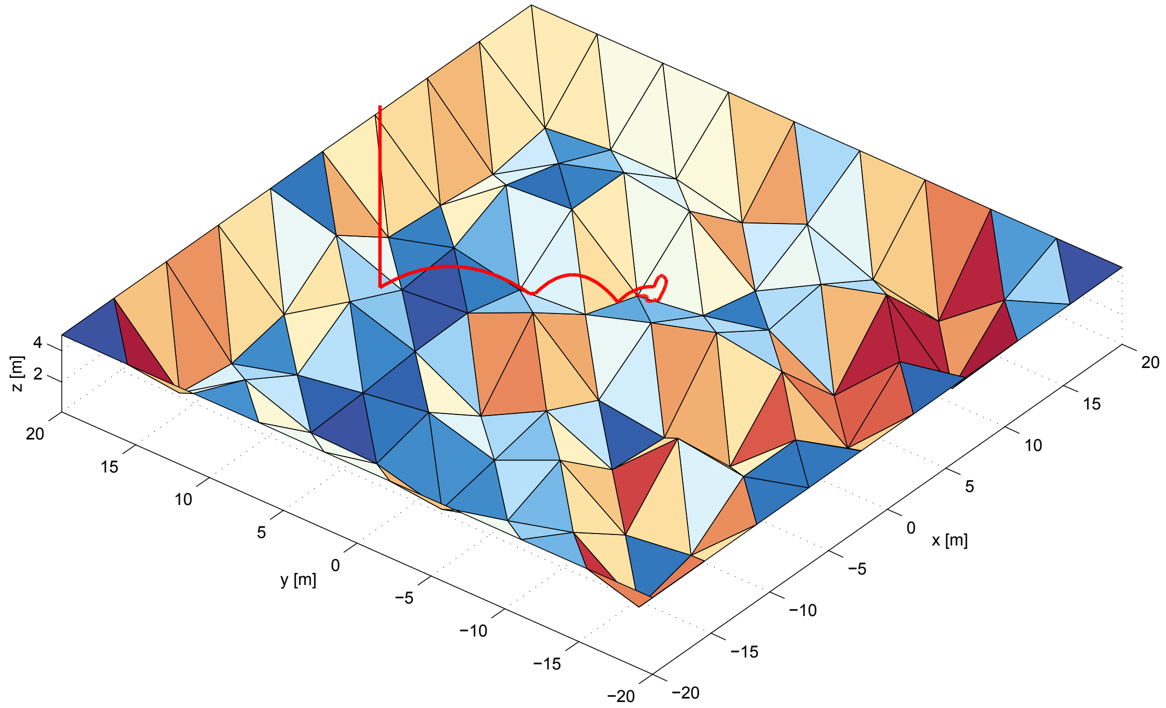

Figure 8.19: Simulated trajectory 3 on spike world.

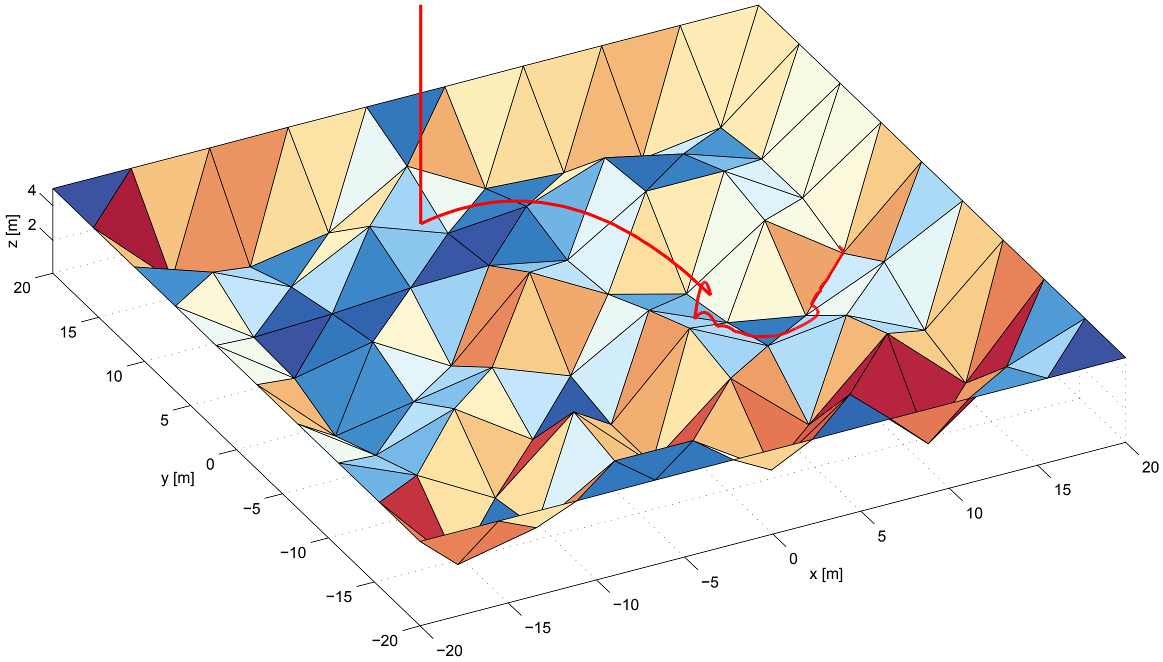

Figure 8.20: Simulated trajectory 4 on spike world.

Part IV

Simulation and Results

Chapter 9

Unitary Systems

WITH THE SIMULATION software that was developed and discussed in the preceding chapters, we are now able to generate high numbers of asteroid lander trajectories. This allows us to produce the results necessary to achieve the thesis goals set in Chapter 3. For now, we restrict ourselves to landing on a unitary asteroid body; deployment to binary systems will be treated in the subsequent chapter. Section 9.1 discusses the selected unitary target and the strategy applied to deploy our landers; special attention is also given to the fictitious mission scenario and hardware that is simulated. Section 9.2 presents our results for nominal deployment, which provides a general assessment of the employed landing strategy. As shown in the previous chapters, deployment is sensitive to a number of parameters; we also investigate the effect of varying these parameters on the lander trajectories. Section 9.3 analyzes the effect of rocks and boulders on the asteroid surface, Section 9.4 discusses variations in the surface interaction coefficients, and Section 9.5 finally studies the effects of the mothership GNC accuracies.

9.1 Mission Scenario

The polyhedron shape models applied in our simulations are available online for a number of asteroids [45]. Most models have been constructed using ground-based observations and are of low-to-medium resolution. Only those asteroids visited by spacecraft have high-resolution shape models available. As it is unlikely for any of these bodies to be visited *again*, it is tempting to investigate deployment to one of the former asteroids. However, any results produced for such cases would be of questionable scientific accuracy due to the inherent errors present in the gravitational and contact interactions with such (relatively) low resolution models. As discussed in Section 2.1.2, asteroid 25143 Itokawa was visited by the Japanese Hayabusa spacecraft in 2007; a mission that resulted in Itokawa's 200,000-facet polyhedron model being the highest resolution currently available for any asteroid. We have therefore selected this body as the target for our simulations of deployment to a unitary system.

Target

The general shape of 25143 Itokawa has frequently been described as resembling that of a sea otter [20]. The asteroid consists of two main parts; the smaller is referred to as the *head*, the larger is called the *body*. Both parts are connected to each other through the *neck*; an overview of this geometry is shown in Figure 9.1. The major axes of the asteroid have lengths of respectively 535 ± 1 m, 194 ± 1 m and 209 ± 1 m. The mass and mean volumetric density of Itokawa are respectively $3.51 \pm 0.105 \times 10^{10}$ kg and 1.90 ± 0.13 g/cm^3. The asteroid is in uniform rotation with a period of 12.1324 ± 0.0001 hr; other relevant parameters may also be found in [20]. In our simulations, we will make use of Itokawa's full-resolution polyhedron model for contact interactions, but apply the simplified 320-facet model for gravity modelling, as discussed in Section 7.3.

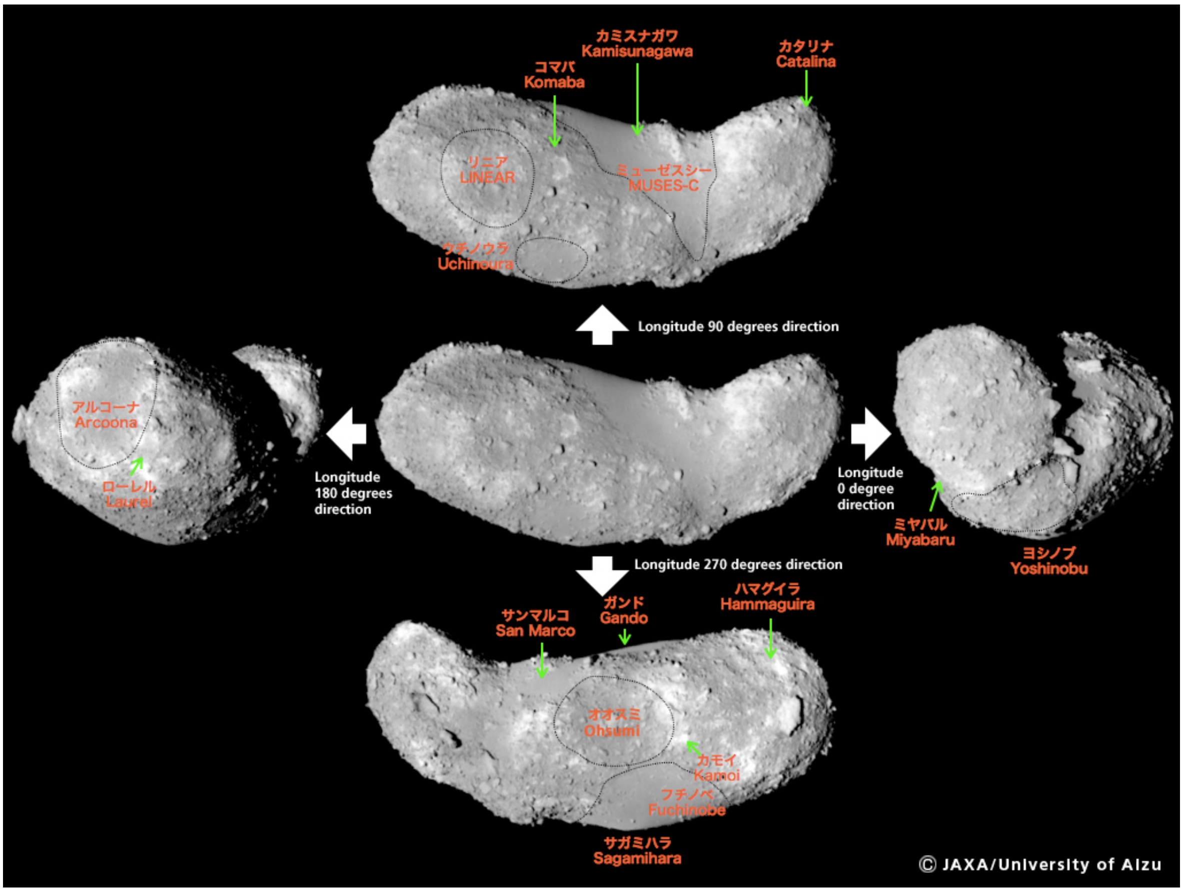
カミスナガワ
Kamisunagawa
カタリナ
Catalina
コマバ
Komaba
リニア
LINEAR
ミューゼスシー
MUSES-C
ウチノウラ
Uchinoura
Longitude 90 degrees direction
アルコーナ
Arcoona
ローレル
Laurel
Longitude 180 degrees direction
Longitude 0 degree direction
ミヤバル
Miyabaru
ヨシノブ
Yoshinobu
Longitude 270 degrees direction
ハマグイラ
Hammaguira
ガンド
Gando
サンマルコ
San Marco
オオスミ
Ohsumi
カモイ
Kamoi
フチノベ
Fuchinobe
サガミハラ
Sagamihara
© JAXA/University of Aizu

Figure 9.1: Asteroid 25143 Itokawa [46].

Deployment Strategy

The strategy we apply to release and deploy landers to Itokawa (or any given unitary body) is taken from [16] and is based on the structure of the asteroid's amended potential field. We have shown this field together with its four equilibrium points in Section 7.1. More specifically, the strategy makes use of the energy characteristics of this potential field. It is easy to see that we wish to release landers from their mothership with the lowest specific energy possible, as this implies there is less energy to be damped before the lander comes to a full stop on the asteroid surface. Following this principle, it is desirable to release the landers as close to the asteroid as possible, with the lowest possible relative velocity with respect to the surface. However, this contradicts the preference from mission designers to stray from close approaches with the asteroid surface. This is because, when moving very close to the surface, any component failures or large GNC inaccuracies could potentially result in a 'crash'.

The strategy discussed in [16] uses an optimum between these two contradictory requirements, and deploys landers from the neighbourhood of the lowest energy (saddle) equilibrium point of the amended potential field. In this strategy, the mothership is set on a hyperbolic[1] escape trajectory that passes by the equilibrium. By 'ejecting' the lander in the vicinity of this point with a specific velocity, it will be set on a trajectory along the unstable manifold of the equilibrium point, assuming that the lander's total initial velocity is low. This manifold then guides the lander toward the asteroid surface, after which the first and subsequent impacts dissipate energy until the lander has come to a complete stop. Meanwhile, the mothership's trajectory safely guides it away from the asteroid surface.

This strategy can be modified to mission designers' wishes: when moving the point of release further away from the asteroid surface (along the axis of the lowest-energy equilibrium point), the mothership safety will increase but the probability of successful lander deployment will diminish. Analogously, when we move the release point closer to the surface, the chances of successful landing will increase at the cost of decreasing the safety of the mothership. The particular effects of moving the release point will be analyzed in Section 9.5; for nominal deployment we release the lander exactly from the lowest-energy equilibrium point - for Itokawa this is the saddle point at $[520, -5]$ m in the RB1F.

Lander Hardware and Surface Parameters

The lander hardware parameters used in our simulations mimic those of the BASiX mission discussed in Section 2.2.4, simply because it is the only (proposed) mission to indeed apply passive, spherical lander packages. These landers have a radius of $R = 0.125$ m and a mass of

---

[1] Although the geometric shape of the mothership orbit is not exactly a hyperbola, we use the term here to refer to an orbit that will escape the asteroid's neighbourhood.

$m = 10$ kg[2]. Related to this choice of lander hardware are also the parameters that govern the interactions between the pod and the asteroid surface, which are properties of the material and structure of the lander.

The magnitude of the coefficient of restitution e, which governs collisions, is dependent on the elasticity of the impacting objects. Using telemetry data from Hayabusa's touchdown, [5] was able to estimate the value of e of the spacecraft bouncing on the surface of Itokawa as $e \approx 0.84$ for an impact speed of 6.7 cm/s. This value is considerably larger than that measured for microgravity impacts in dust with velocities of 1-100 cm/s, where the value of $e \approx 0.01$ was obtained [47]. A third relevant measure is provided by [48], where the coefficient of restitution of ∼10-meter sized boulders rebounding at ∼5 m/s on the surface of Eros was estimated at $e \approx 0.10$. Furthermore, [15] and [34] used values of respectively $e = 0.50$ and $e = 0.65$ in simulations of landers on the surface of an asteroid. We select the average value of $e = 0.65$ as nominal, and will investigate the effect of changing this coefficient in Section 9.4.

The coefficient of friction f, which determines the magnitude of the Coulomb friction force and torque, remains to date unknown for the motion of an object on the regolith surface of an asteroid. In [15], a value of $f = 0.5$ was used. [34] applied a friction coefficient of $f = 1.0$ but stated that the particular value of f does not affect the surface motion of a spherical pod on an asteroid, as long as it is not too low ($f < 0.2$). We select the average of the two values encountered in literature, $f = 0.75$, as nominal value and study the effect of changing the parameter in Section 9.4.

The coefficient of rolling resistance C_{rr} of a spherical object rolling on a granular surface surface remained unknown until recent experimental internship work by the author of the current thesis. In this (unpublished) work, we have measured C_{rr} of a ball with radius $R \approx 0.11$ m to be 0.035 [49]. As the experiments performed in this work were aimed particularly at producing results that can be used in asteroid pod simulations, this value is selected as nominal. We will again vary the magnitude of the coefficient in Section 9.4.

Mothership GNC

Finally, we also require some parameters that that describe the mothership GNC capabilities. The inaccuracies present in this systems will affect the release position and velocity of the landers and, as discussed before, influence the maximum allowable distance from the asteroid surface to ensure successful deployment. The two relevant parameters here are the 3σ-errors on the release position and velocity; we assume for simplicity that these errors are equal in all directions. In Section 2.2.2, the norm of the expected accuracies for the OSIRIS-REx spacecraft have been given as $3\sigma_{pos} = 3.25$ m and $3\sigma_{vel} = 0.20$ mm/s. On the other hand, [16] uses the values $3\sigma_{pos} = 60$ m and $3\sigma_{vel} = 30$ mm/s; more than an order of magnitude in difference, though they state that these are very conservative. For our nominal simulation parameters, we select intermediate values of $3\sigma_{pos} = 10$ m and $3\sigma_{vel} = 10$ mm/s. Finally, we also select a nominal release position and velocity. As discussed before, we will nominally release the landers from the lowest-energy saddle equilibrium point at $X_{rel} = [520, -5, 0]$ m; as nominal release velocity we select the velocity of $V_{rel} = 3$ cm/s that is used in [16]. This release velocity is directed along the negative x-axis of the RB1F. These parameters will be varied in Section 9.5 and their effects on the resulting lander deployment investigated. An overview of all parameter values mentioned in the above is shown in Table 9.1.

---

[2] The initial BASiX pod design states that the pod mass will be *less than 15 kg.*

Table 9.1: Nominal Deployment Parameters.

Parameter	Value
m	10 kg
R	0.125 m
e	0.65
f	0.75
C_{rr}	0.035
X_{rel}	[520,-5,0] m
$3\sigma_{pos}$	10 m
V_{rel}	3 cm/s
$3\sigma_{vel}$	1 cm/s

9.2 Results for Nominal Deployment

Using the parameters mentioned in Table 9.1, we have produced a batch of 100 lander deployment simulations on asteroid Itokawa. As an overview, the first 10 trajectories are shown in full in Figure 9.2a. Additionally, Figure 9.2b visualizes the initial, first impact, and final stop positions of all trajectories in the batch. Finally, Figures 9.2c and Figures 9.2d provide a histogram-overview of respectively the time-to-first-impact and time-to-full-stop. It is noted that the velocity uncertainty acts only on the magnitude, and not direction, of the simulations presented in Sections 9.2 through 9.4. The full, three-dimensional uncertainty will be applied in Section 9.5.

Reviewing these results, we can see that the applied deployment strategy is indeed successful; the lander pod reaches the asteroid surface in all of the 100 simulated cases. We observe from Figure 9.2b a high degree of consistency in the lander's point of first impact (indicated by a blue cross). This result was expected, since all simulations are initiated in the close

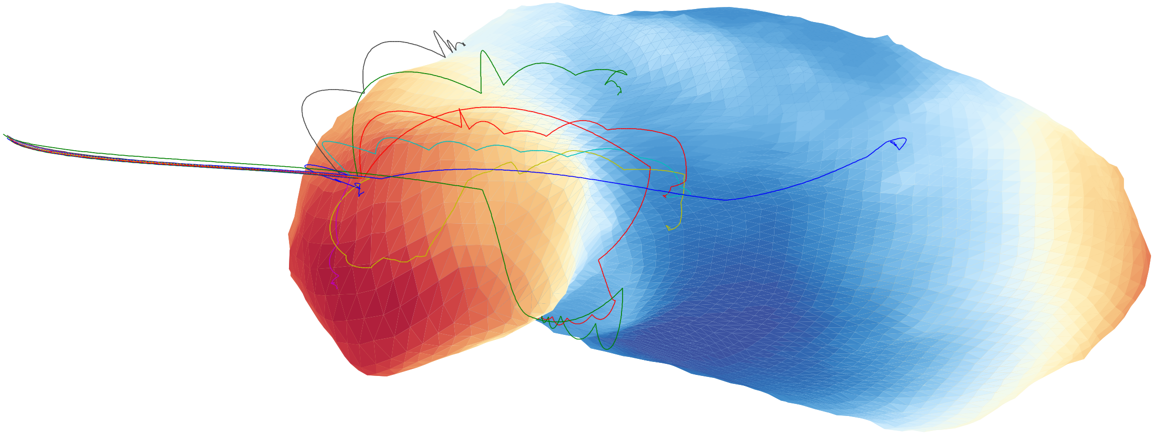

(a) Overview of 10 trajectories.

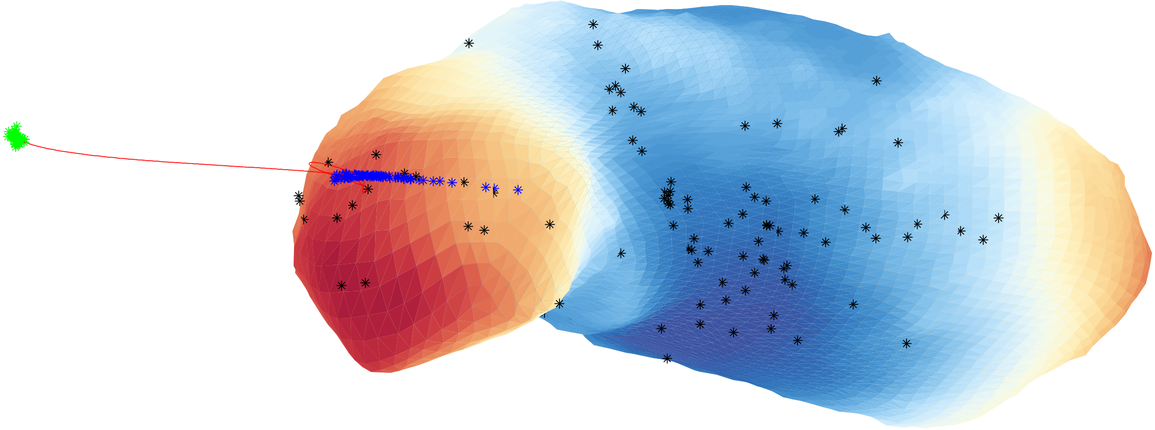

(b) Initial, first impact and final stop locations.

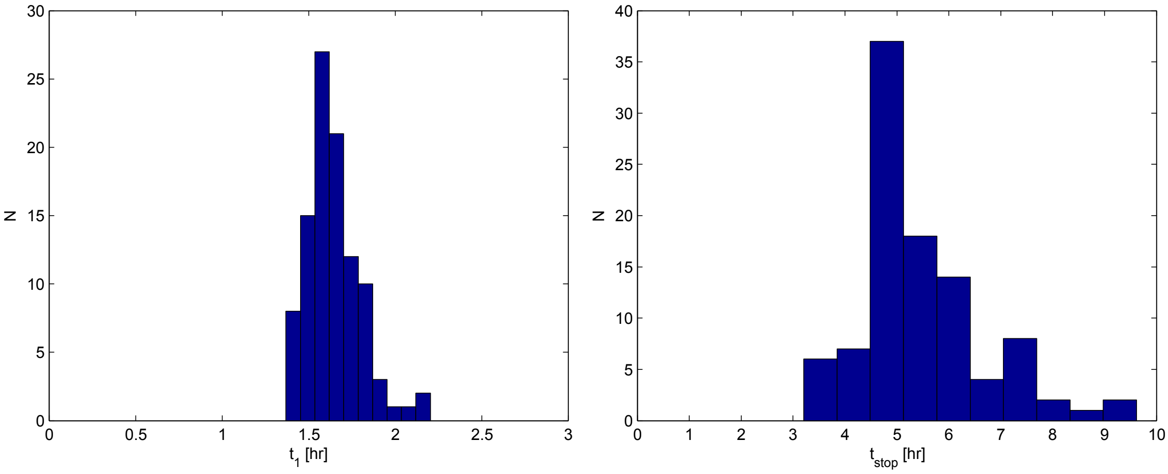

(c) Time to first impact.

(d) Time to full stop.

Figure 9.2: Results for nominal deployment to Itokawa.

neighbourhood of the equilibrium point. A similar consistency is seen in the time to first impact. Reviewing the location of final stop for all simulations, a much higher degree of randomness is observed. This randomness is due to both local variations in the slope of the asteroid and the effect of the rocks and boulders on the asteroid surface. As a result of these, two lander pods with very similar release conditions may be subjected to completely different impulses and end up at opposite ends of the asteroid. We do observe that most trajectories terminate in an area of low amended potential; consistent with the fact that a ball is more likely to come to rest at the bottom of a hill than on its top. Finally, we note that the mean time-to-full-stop $\mu_{t_{stop}} = 5.45$ hr with a standard deviation of $\sigma_{t_{stop}} = 1.19$ hr. These numbers are also repeated in Table 9.2. A clear conclusion with regard to mission design can be drawn from these statistics: any lander deployed to Itokawa using the strategy outlined above requires roughly 9 hours of battery life to guarantee 3σ certainty that the lander will not run out of power before settling on the surface. This minimum battery life is complementary to the power requirements for surface operations once this settling has occurred.

9.3 Effect of Rocks

The stochastic model used to 'populate' the asteroid surface with rocks and boulders was discussed in Section 4.6, where it was argued that this model captures the medium-sized surface features. We now investigate whether it is indeed important to include these rocks in our asteroid models, by excluding the model from our simulations and comparing the resulting trajectory characteristics with the nominal results obtained in the previous section. We recall from Section 4.6 that the rock model manifests itself through both a randomization of impacts, and through the occurrence of rolling collisions when the lander performs contact motion on the asteroid surface. We study both effects by alternately excluding them from our simulations.

Therefore, we have first produced a batch of 100 simulations where the effect of impact collisions is not taken into account. The randomization of these collisions is therefore removed, and the outgoing velocity is purely a result of the geometry of the facet a pod collides with. Again, we show the first 10 trajectories in Figure 9.3a and the interesting points for all trajectories in Figure 9.3b. The distribution of first impact and final stop times are shown in Figures 9.3c and 9.3d. Analogously, we have produced a batch of simulations where impact collisions are active, but rolling collisions are not included. The results from these simulations are shown in Figures 9.4a through 9.4d. It is noted that in both batches, the nominal deployment parameters shown in Table 9.1 were again used.

Reviewing these results with comparison to the nominal deployment discussed in Section 9.2, we can make some interesting observations. When excluding rocks during impact collisions,

Table 9.2: Statistics of time to full stop for all unitary simulation batches.

Setting	$\mu_{t_{stop}}$ [hr]	$\sigma_{t_{stop}}$ [hr]	$\frac{\lvert\mu-\mu_{nom}\rvert}{\sigma_{nom}}$ [%]	$\frac{\lvert\mu-\mu_{nom}\rvert}{\mu}$ [%]
Nominal	5.45	1.19		
No impact coll.	6.19	1.00	+62.80	+12.03
No rolling coll.	5.36	1.00	-7.82	-1.73
$e = 0.50$	4.68	1.10	-64.53	-16.35
$e = 0.80$	7.43	1.48	+167.08	+26.68
$f = 1.00$	5.37	1.03	-6.74	-1.49
$f = 0.50$	5.41	1.10	-3.30	-0.72
$C_{rr} = 0.045$	5.16	0.86	-24.40	-5.61
$C_{rr} = 0.025$	6.05	1.53	+50.85	+9.97

there is far less randomness in the resulting lander trajectories; their final positions are more clustered together. This result makes sense: when rocks are ignored during impact collisions, it is purely the shape of the polyhedron model that governs the lander-asteroid collisions. As local slope variations of the 'pristine' model are small compared to those of the model populated with rocks, the lander trajectories show a smaller degree of dispersion. Finally, we read from Table 9.2 that simulations *without* impact collisions last 0.63 standard deviations longer. This fact, too, can be explained through the shape of the 'pristine' asteroid model. Successive collisions of a lander with this model are unlikely to show large variations in the direction of the normal; otherwise stated, the lander's velocity will mostly be damped in a single direction by collisions, and a significant amount remains to be dissipated in contact motion. When rocks *are* included during impact collisions, these rocks will induce variations in the normal direction and damp velocity in all directions. As a result, there remains less energy to be damped during contact motion, and the lander will stop sooner. We conclude that it is important to take into the effect of rocks on the asteroid surface during collisions, both from a dispersion and a landing-duration point of view.

Switching our attention to the simulations without rolling collisions, we observe no notable effect on the lander dispersion over the asteroid surface, nor on the time to full stop. Indeed, the contribution of rolling collisions may be ignored without compromising the accuracy of our results. This fact can be explained as follows: most energy dissipation takes place during 'flying' collisions, by the time the lander starts contact motion its surface velocity will therefore be low. Although rolling collisions may significantly alter the direction of this velocity, the global effect on the trajectory is not discernible as the lander no longer has the capability of covering a substantial distance along the surface.

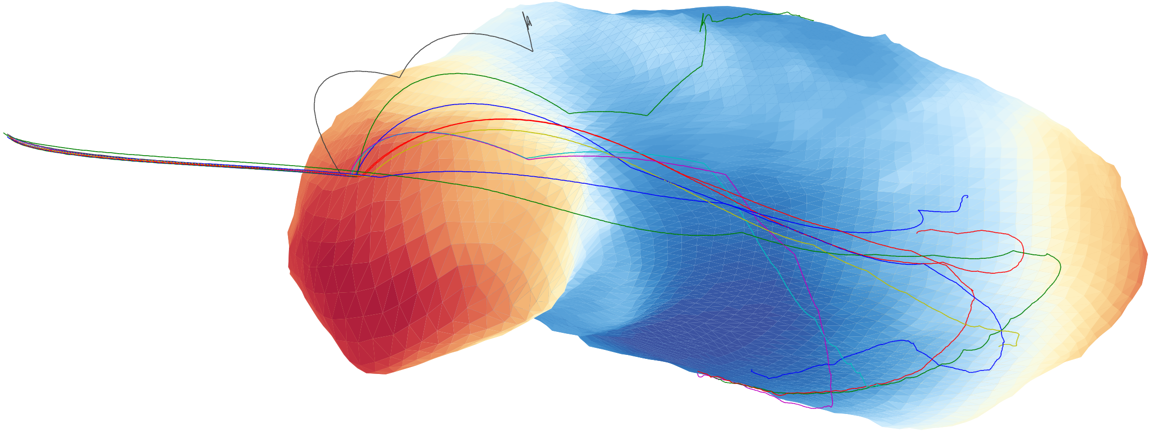

(a) Overview of 10 trajectories.

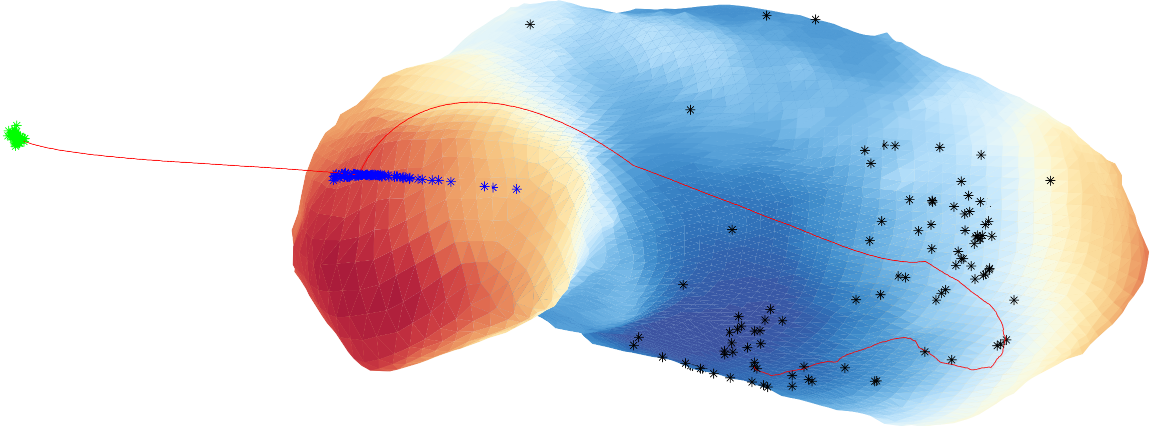

(b) Initial, first impact and final stop locations.

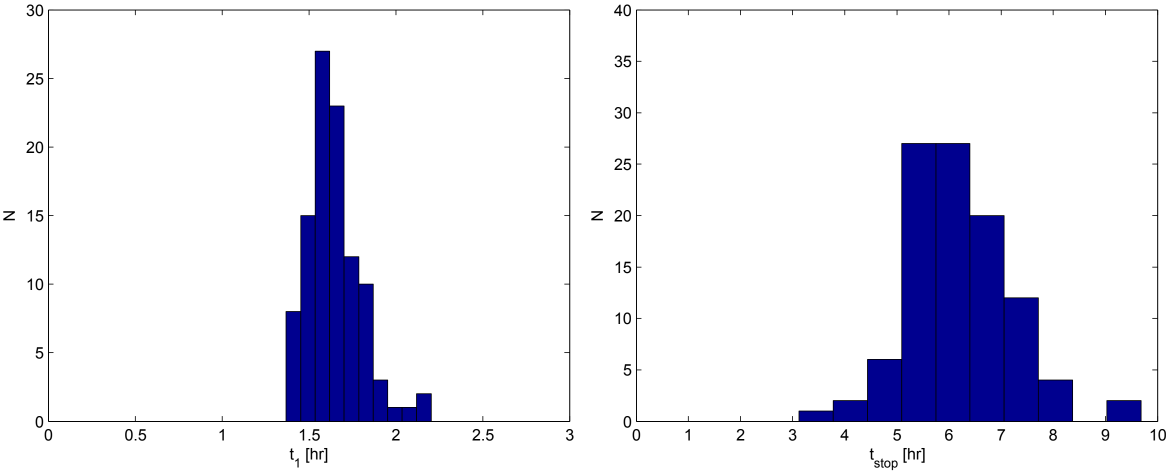

(c) Time to first impact.

(d) Time to full stop.

Figure 9.3: Results for deployment to Itokawa, no rocks during impact collisions.

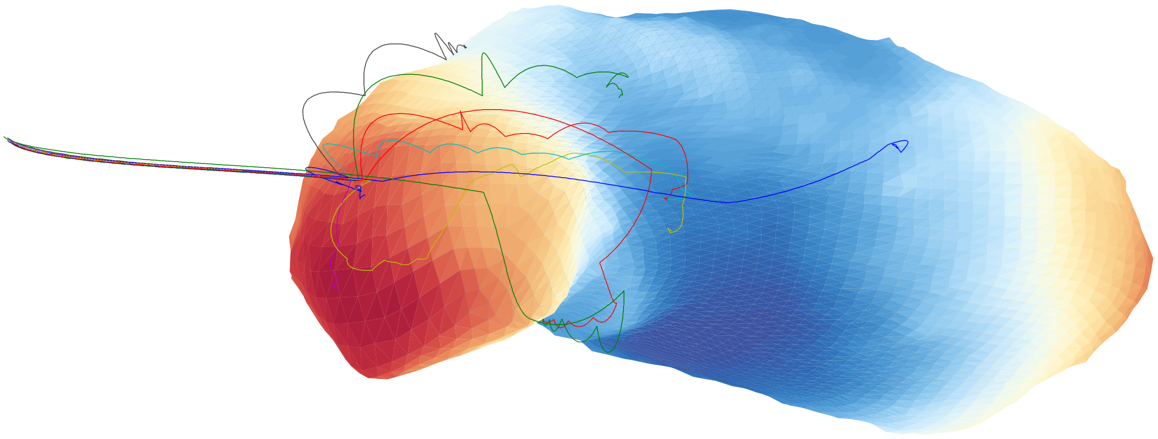

(a) Overview of 10 trajectories.

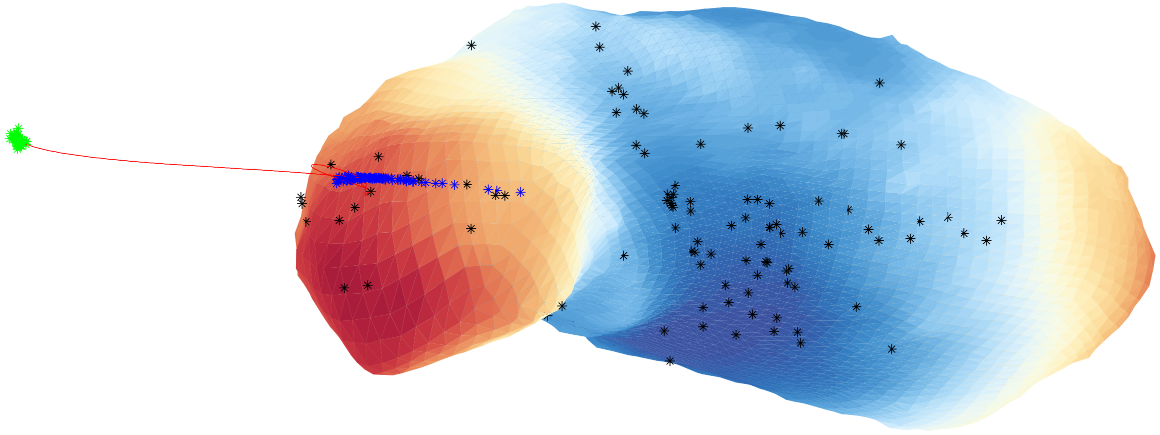

(b) Initial, first impact and final stop locations.

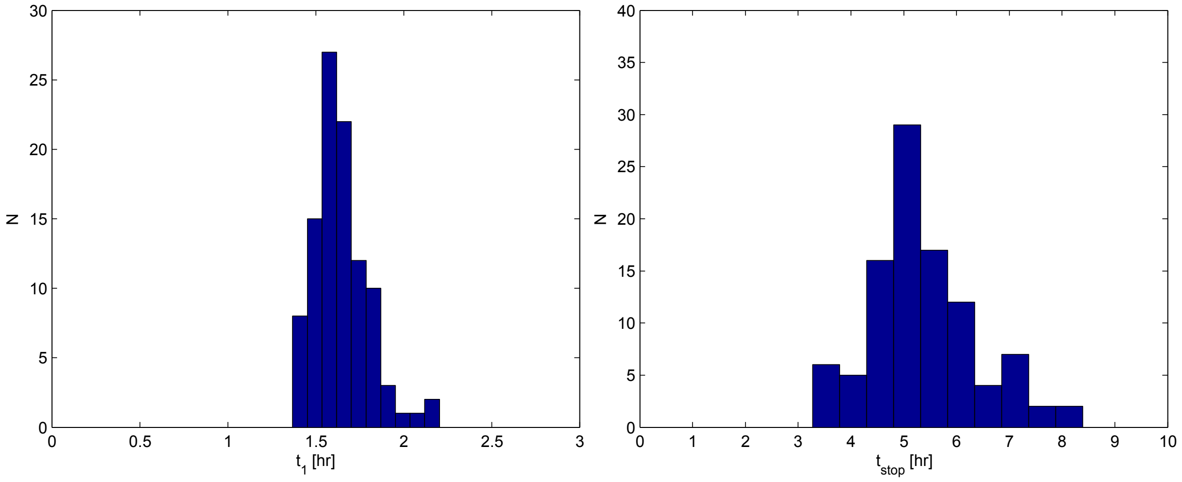

(c) Time to first impact. **(d)** Time to full stop.

Figure 9.4: Results for deployment to Itokawa, no rolling collisions.

9.4 Effect of Interaction Coefficients

In Section 9.1, we have selected nominal values for the three coefficients e, f and C_{rr} that govern the contact interactions between a lander and the asteroid surface. We now investigate the effect of varying the magnitude of these coefficients on the resulting lander trajectories. For each of the three coefficients, we have produced one batch of 100 simulations with a higher coefficient value, and one batch with a lower value; the exact numbers used are shown in Table 9.3. The considered coefficient is the only parameter varied during these batches; all other parameters are set to their nominal values as shown in Table 9.1.

Table 9.3: Overview of tested values in interaction coefficient variation.

	Low	Nominal	High
e	0.50	0.65	0.80
f	0.50	0.75	1.00
C_{rr}	0.025	0.035	0.045

Coefficient of Restitution

The results of the simulations with $e = 0.80$ are included in Table 9.2. Although we do not show figures of the deployment, when comparing the results with the nominal case where $e = 0.65$, we see a clear effect of e on the lander trajectories. The higher the coefficient of restitution, the larger the dispersion in trajectories across the surface. This result is intuitive: the higher e, the lower the energy dissipation per collision, the more collisions will take place before the lander comes to a full stop. As there are more collisions, there is more opportunity for rocks on the surface to disperse the lander trajectories. This is also reflected in the mean time-to-full-stop values shown in Table 9.2; the higher e, the longer it takes the pods to come to a full stop. We have further visualized this in Figure 9.5 which plots the time to final stop, with error bars, versus the coefficient of restitution. It is clear that the particular value of e has a *very* important effect on the trajectory of a lander.

Coefficient of Friction

In addition to the nominal case, we ran batches with a friction coefficient of $f = 1.00$ and $f = 0.50$; the results are again included in Table 9.2. When comparing the the statistics of the time-to-full-stop, we notice no notable difference. Indeed, it seems the particular value of the coefficient of friction does not impact the trajectories. This result shows that the synchronization between spin and rotation when contact motion starts happens so quickly that the particular value of f does not affect the motion of the lander. It is critical to include Coulomb friction in our simulations, but we can freely choose the value of f.

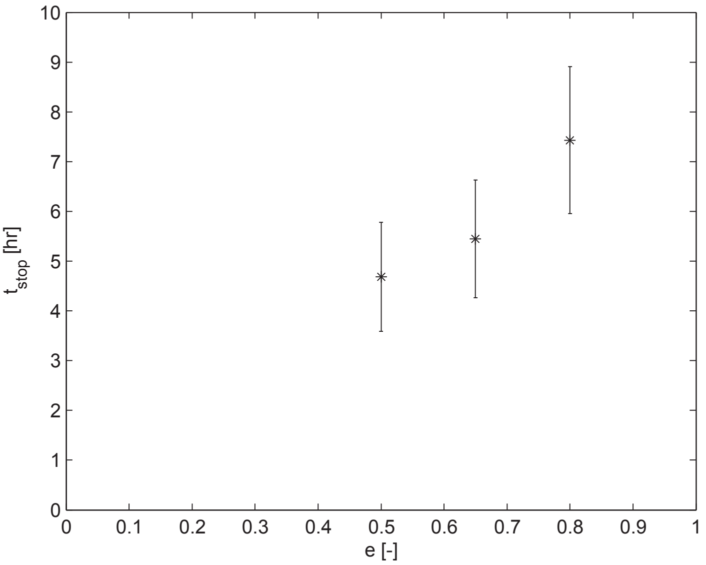

Figure 9.5: Time to final stop versus coefficient of restitution for landing on Itokawa.

Coefficient of Rolling Resistance

Finally, we have examined the effect of varying the value of the coefficient of rolling resistance C_{rr}. Upon reviewing the results in Table 9.2, we note a clear effect of C_{rr} on the trajectory and time to stop. Although not as strong an impact as the coefficient of restitution, it is clear that the higher C_{rr}, the shorter the trajectory. This agrees with the acting principles of the rolling resistance force and torque, as a higher C_{rr} implies faster dissipation of energy. We can see this effect when looking at the trajectory dispersion as well; when C_{rr} is lowered we observe a slightly higher degree of dispersion, as contact motion lasts longer and the landers have more chance to spread across the surface. Applying a realistic value of C_{rr} is thus relatively important, though definitely not as important as having the correct value for e.

The variation of interaction parameters presented in this section is useful in obtaining an estimate of the sensitivity of deployment to uncertainties in our knowledge of the 'true' interaction parameter values.

9.5 Effect of Deployment Parameters

We now switch our attention to the deployment parameters. As discussed in Section 9.1, the safety of the mothership and the success of deployment are contradictory requirements when selecting the particular deployment parameters for a mission. By investigating the individual effect of the release position, velocity, and the related uncertainties, it will be possible to establish GNC requirements and quantify the relation between safety and deployment success.

For the simulations in this section, we apply again the nominal deployment parameters shown in Table 9.1. The only difference is that the release velocity uncertainty no longer only acts along the direction of release, but rather in all three dimensions. Therefore we have first produced a new 100-simulation 'nominal' batch, with this new velocity uncertainty. The results from this updated nominal batch are shown in Figures 9.6a through 9.6d. We note how the spread of first impact locations is different than those observed in Figure 9.2b; this is due to the velocity uncertainty being applied in all three directions in the present case.

Effect of Position

As the equilibrium point from which landers are released lies very close to the x-axis of the applied reference system, we will investigate the effect of changing the lander release position simply by shifting the release point along the x-axis. An overview of the coordinates of the tested release points is shown in Table 9.4, together with the respective distance from the asteroid surface of these points. This table also shows the percentage of trajectories that successfully reached the surface within a time span of ~ 16 hours. Trajectories that do not reach the asteroid and/or come to a full stop within this time span are considered to be *failed* deployments, as the real landers are likely to be limited in power supply. We also show the locations of these release points relative to the asteroid in Figure 9.7; the nominal release position is marked in red.

Table 9.4: Statistics of release position variation at Itokawa.

	Towards surface			Nominal	Away from surface		
x [m]	445	470	495	520	545	570	595
y [m]	-5	-5	-5	-5	-5	-5	-5
z [m]	0	0	0	0	0	0	0
d [m]	155	180	205	230	255	280	305
Success [%]	100	100	100	100	100	37	51
$\mu_{t_{stop}}$ [hr]	4.62	4.81	5.35	5.54	5.85	8.78	14.25
$\sigma_{t_{stop}}$ [hr]	1.09	1.29	1.53	1.16	1.31	5.17	4.35
$\frac{\lvert\mu-\mu_{nom}\rvert}{\sigma_{nom}}$ [%]	-79.26	-62.53	-16.08		+27.00	+280.05	+752.59
$\frac{\lvert\mu-\mu_{nom}\rvert}{\mu}$ [%]	-16.56	-13.07	-3.36		+5.64	+58.53	+157.28

We can see from Table 9.4 that all landings are successful when launched from the equilibrium point or closer to the asteroid surface. Also all releases from $x = 545$ m, 25 m from the equilibrium point in the direction away from the asteroid surface, are successful. However, when moving any further from the asteroid, over half of landings fail, with the landers either not reaching the surface and flying off into orbit, or taking too long to come to a full stop (possibly after multiple orbits). An example of a simulation that failed to reach the surface

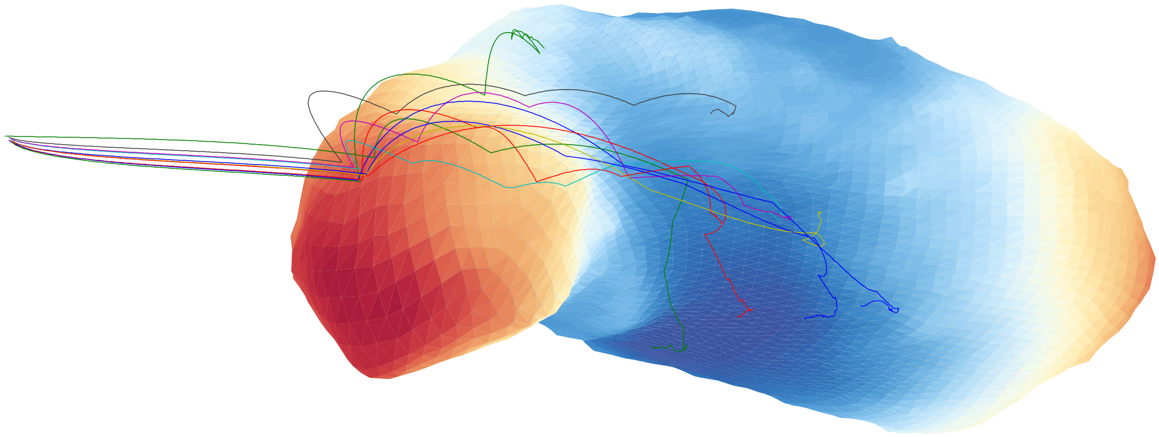

(a) Overview of 10 trajectories.

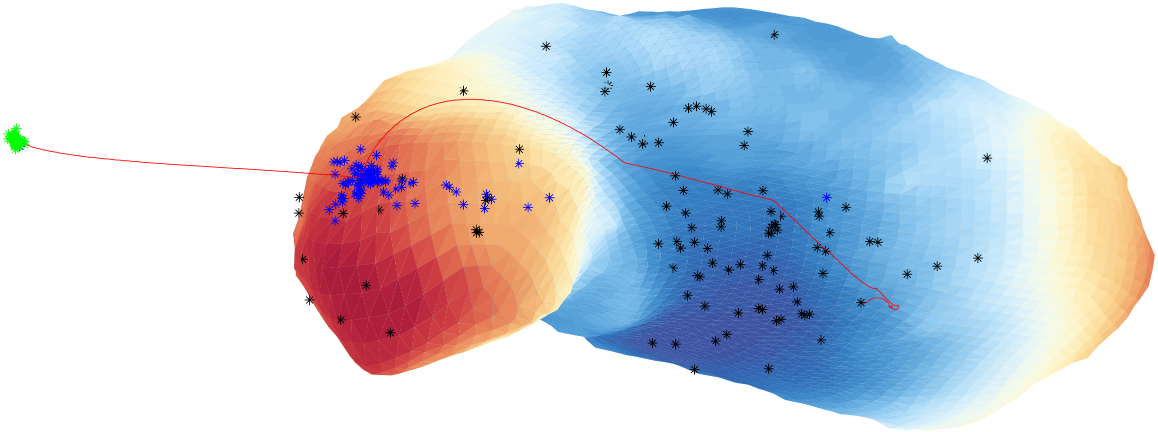

(b) Initial, first impact and final stop locations.

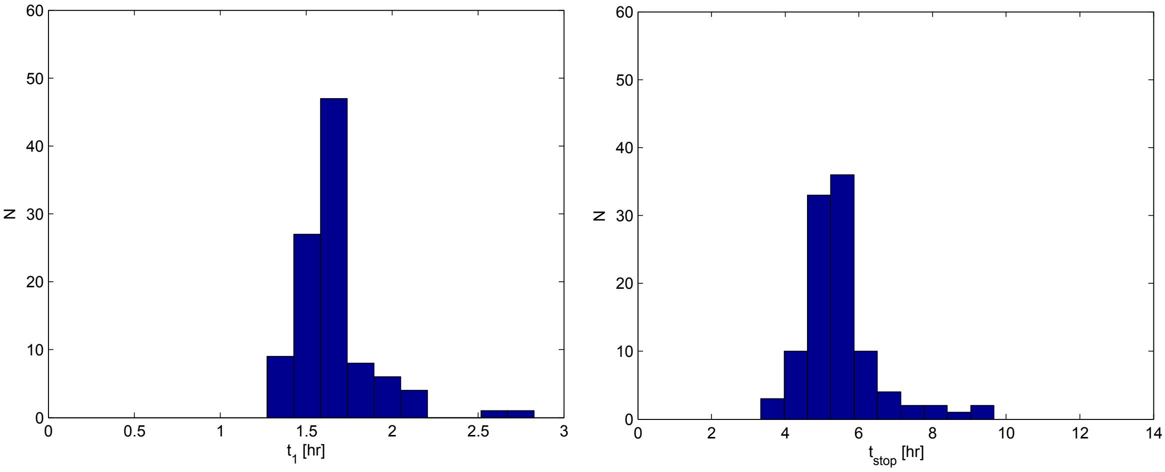

(c) Time to first impact.

(d) Time to full stop.

Figure 9.6: Results for nominal deployment to Itokawa with velocity uncertainty acting in all three directions.

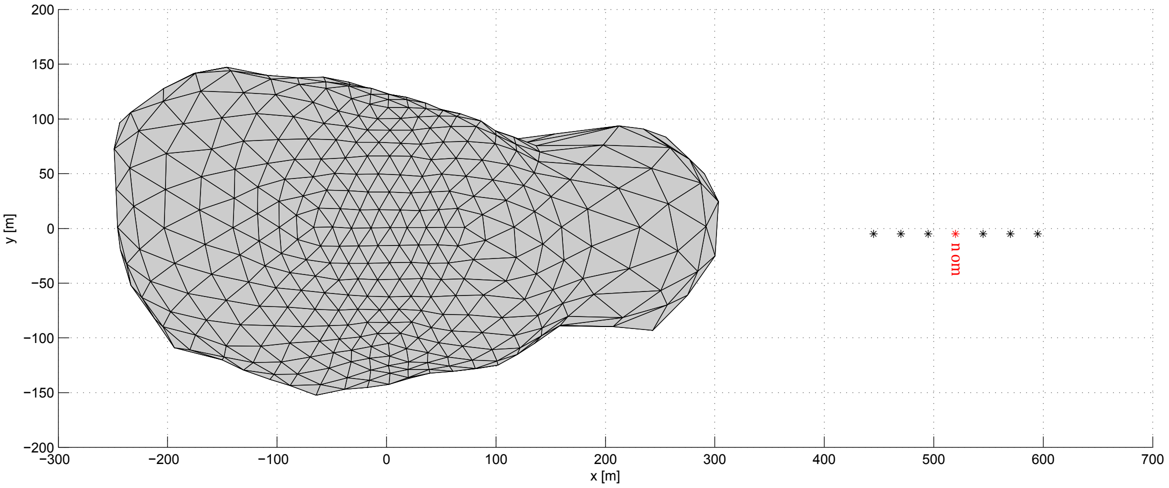

Figure 9.7: Overview of tested release points for deployment to Itokawa.

is shown in Figure 9.8. We conclude that it is inadvisable to move the release point more than 5% away from the equilibrium point, relative to its distance to the center of mass of the asteroid body. Furthermore, we can see a clear relation between the distance from the surface and the time to full stop; which is also visualized in Figure 9.9. The relative change in mean time-to-full-stop is about equal to the relative change in release position, relative to the location of the equilibrium point. Finally, we observe that the lander pods scatter less when released closer to Itokawa's surface - an intuitive result, since landers released from a higher altitude have more energy, and therefore more potential to move across the asteroid surface, both before and after the first impact. One final remark is that the earlier state 5%-limit relates not only to the selected release position, but also to the inaccuracy of the equilibrium point location. When moving the release point closer to the asteroid surface, we essentially account for errors in the applied gravity field modelling and ensure deployment remains successful.

Effect of Position Uncertainty

To investigate the effect of the uncertainty in the position of the mothership at the moment of release, we perform simulations with different values of $3\sigma_{pos}$. The values tested are shown in Table 9.5. Again, this table also includes the success rate of deployment and statistics of the time-to-full-stop. We can see that the mean time-to-full-stop does not notably change; this confirms our expectations as the mean position of release remains the same for all five cases tested, despite the different $3\sigma_{pos}$. Furthermore, we note that only the worst-case uncertainty leads to failed landings, and this only in one simulation. This is in agreement with the previous results where the release position was varied. There, we concluded that the release position should not be moved more than 5% behind the saddle equilibrium point, or 25

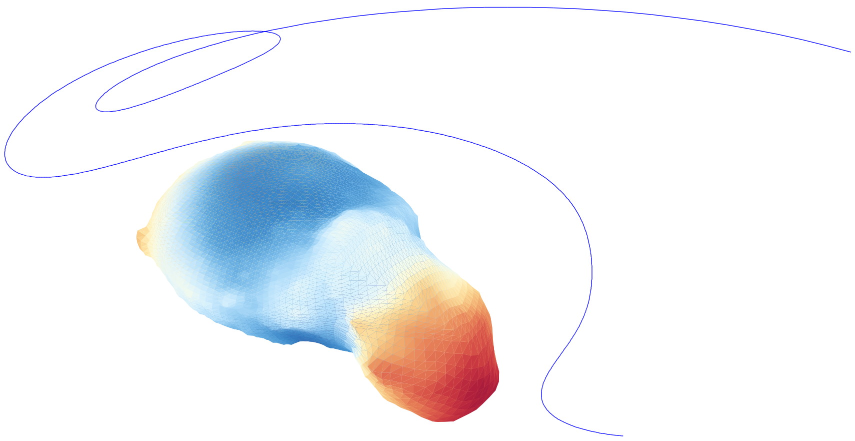

Figure 9.8: Example of a failed landing at Itokawa, release from x=595 m.

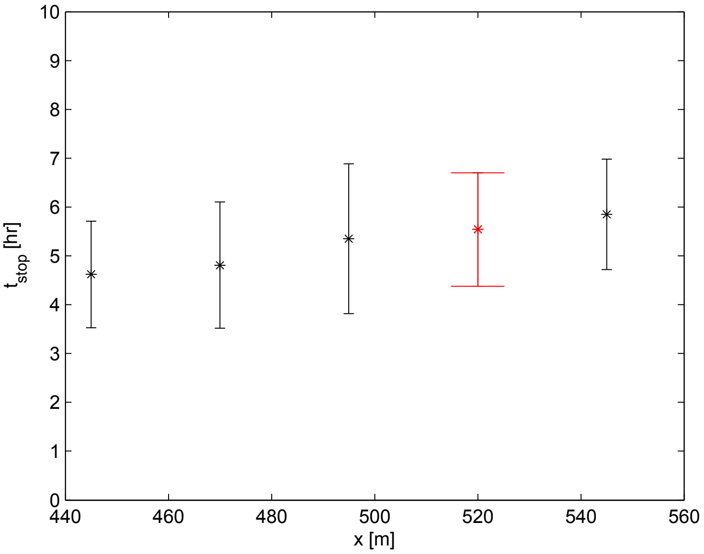

Figure 9.9: Time-to-full-stop versus release position for successful deployments at Itokawa.

meters in absolute distance. As all but the worst position uncertainty case have a $3\sigma_{pos}$ which guarantees the simulations are initiated within this limit, their deployments are successful. However, when deploying from the equilibrium point with a position uncertainty of $3\sigma_{pos} = 90$ m, the release point will in some cases be located outside of the 5% limit, leading to a risk of failed landings. We therefore extend the conclusion of the previous section and state that the release position *combined with its uncertainty* should guarantee that the lander is released within 5% from the lowest energy equilibrium point. Stated differently, if the release position is moved closer to the asteroid surface, the position required position accuracy can be relaxed - and vice versa.

Table 9.5: Uncertainties tested in variation of release position uncertainty.

	Better		Nominal	Worse	
$3\sigma_{pos}$ [m]	1.0	3.0	10.0	30.0	90.0
Success [%]	100	100	100	100	99
$\mu_{t_{stop}}$ [hr]	5.36	5.52	5.54	5.56	5.57
$\sigma_{t_{stop}}$ [hr]	1.00	1.03	1.16	1.18	1.57
$\frac{\lvert\mu-\mu_{nom}\rvert}{\sigma_{nom}}$ [%]	-15.31	-1.51		+2.23	+2.78
$\frac{\lvert\mu-\mu_{nom}\rvert}{\mu}$ [%]	-3.31	-0.32		+0.46	+0.58

Effect of Velocity

We now switch our attention to studying the effects of the lander release velocity, by again setting the nominal deployment parameters of Table 9.1 but varying the magnitude of the release velocity. We recall that the nominal release velocity is 3 cm/s, with an uncertainty of $3\sigma_{vel} = 1$ cm/s, applied in all directions. The magnitude is varied between 1 cm/s and 5 cm/s, noting that the circular orbital velocity[3] at the equilibrium point is equal to $V_c \approx 6.7$ cm/s. The success rate and time-to-full-stop statistics are shown in Table 9.6. Interestingly, only the lowest release velocity of $V_{rel} = 1$ cm/s leads to failed deployments - all other deployments are completely successful. We can also see from this table that the time-to-full-stop is reduced when the release velocity is increased, as visualized by Figure 9.10. This result is somewhat counter-intuitive, as a higher release velocity implies the lander has more energy that needs to be dissipated. This does imply the lander reaches first impact quicker than in the nominal release. We conclude that the energy dissipation during first impact is very determinant of the time-to-full-stop, and is large enough to negate the increase in energy resulting from a higher release velocity. Instead, the time-to-first-impact seems to strongly influence the time-to-full-stop, though the latter is only reduced by about 10% for the highest V_{rel} tested. It would be worthwhile for future research to investigate whether high-energy deployments with $V_{rel} > V_c$, or perhaps even $V_{rel} > V_{esc}$ where, for Itokawa, $V_{esc} = 9.5$ cm/s is the escape velocity[4] at the equilibrium point, can further reduce the time-to-full-stop, without compromising deployment success.

Effect of Velocity Error

Finally, we concern ourselves with the effects of varying the uncertainty on the release velocity. Recalling that the nominal uncertainty was $3\sigma_{vel} = 1.0$ cm/s, we vary the uncertainty between 0.1 cm/s and 5.0 cm/s. The familiar parameters are shown in Table 9.7. There, it can be seen that deployment is always successful for uncertainty lower than or equal to that of

---

[3] Defined as $V_c = \sqrt{\mu/r}$.

[4] Defined as $V_{esc} = \sqrt{2\mu/r}$.

Table 9.6: Values tested in variation of release velocity.

	Lower		Nominal	Higher	
V_{rel} [cm/s]	1.0	2.0	3.0	4.0	5.0
Success [%]	63	100	100	100	100
$\mu_{t_{stop}}$ [hr]	10.67	5.71	5.54	5.34	4.97
$\sigma_{t_{stop}}$ [hr]	2.84	1.19	1.16	1.27	1.44
$\frac{\lvert\mu-\mu_{nom}\rvert}{\sigma_{nom}}$ [%]	+443.71	+15.24		-17.45	-49.28
$\frac{\lvert\mu-\mu_{nom}\rvert}{\mu}$ [%]	+92.73	+3.19		-3.65	-10.30

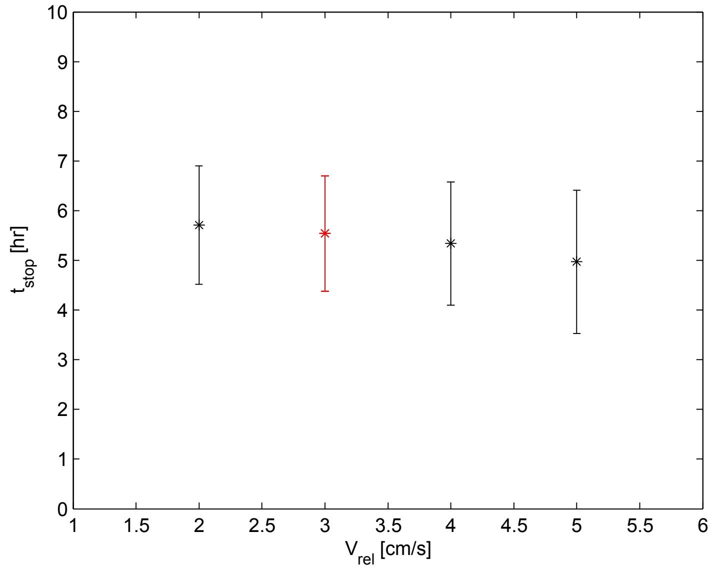

Figure 9.10: Time to full stop versus release velocity for successful deployments at Itokawa.

nominal deployment. However, when increasing the velocity uncertainty beyond the nominal case, we see some deployment failures occurring; an effect which grows worse as the uncertainty is increased. When recalling that the nominal release velocity for our deployments is $V_{rel} = 3$ cm/s, this result makes sense. For a lander to reach the surface of the asteroid, it is obviously necessary that its velocity at release be directed towards the asteroid surface. When the velocity uncertainty $3\sigma_{vel}$ is increased beyond the magnitude of the release velocity V_{rel}, it is no longer guaranteed that the velocity indeed has this direction, leading to deployments which fail to reach the surface. We therefore state, analogously to as was done for the release position and uncertainty, that the release velocity should be set such that, combined with its uncertainty, the velocity is guaranteed to be directed towards the asteroid surface. The particular magnitude selected will affect the time-to-full-stop.

This concludes our investigation of the effects of varying the deployment parameters, and of deployment to unitary asteroid systems. We will now extend our results through the analysis of lander deployment to binary systems.

Table 9.7: Uncertainties tested in variation of release velocity uncertainty.

	Better		Nominal	Worse	
$3\sigma_{vel}$ [cm/s]	0.1	0.3	1.0	3.0	5.0
Success [%]	100	100	100	92	86
$\mu_{t_{stop}}$ [hr]	5.51	5.43	5.54	6.22	5.85
$\sigma_{t_{stop}}$ [hr]	1.20	0.99	1.16	2.53	2.02
$\frac{\lvert\mu-\mu_{nom}\rvert}{\sigma_{nom}}$ [%]	-2.64	-9.03		+58.83	+27.24
$\frac{\lvert\mu-\mu_{nom}\rvert}{\mu}$ [%]	-0.55	-1.89		+12.29	+5.69

Chapter 10

Binary Systems

Binary asteroid systems present a dynamical environment that is quite different from that of a unitary body, due to the relative motion of the primary and secondary around their common center of mass; it is therefore important to study deployment to binary systems separately, as is the focus of the present chapter. We first discuss the target asteroid system selected for our simulations and the applied release strategy in Section 10.1. Next, we present the results for deployment to a secondary body in Section 10.2, and for deployment to a primary body in Section 10.3. As the effects of varying the interaction parameters and rock model have already been investigated in the preceding chapter, we will focus only on changes in the lander release conditions.

10.1 Mission Scenario

Both the AIDA and BASiX missions plan to visit a binary asteroid system to obtain scientific measurements, as presented in Section 2.2. Their respective targets are the 65803 Didymos and 1996 FG_3 systems. It is argued that an investigation of lander deployment to these systems would be highly interesting, as the results could be applied in the design and planning of these missions. Unfortunately, no high-resolution shape models are currently available for either system; any results produced with simulations are therefore of little scientific value. In fact, the only binary asteroid system to have been imaged at sufficiently high resolution is the 1999 KW_4 system, as illustrated earlier in Figure 4.4. Fortunately, this system is thought to be representative of the general binary asteroid population, with its tidally locked secondary body and near-spherical primary body with distinct equatorial ridge. We have therefore selected the 1999 KW_4 system as target for our investigation of lander deployment to a binary asteroid. The relevant parameters of this system are shown in Table 10.1.

Our nominal strategy for deployment to a unitary asteroid was to release landers from the

Table 10.1: Relevant parameters of the 1999 KW$_4$ binary asteroid system [50].

Parameter	Symbol	Value
Primary		
Largest axis	x_1	$1,532 \pm 3\%$ m
Intermediate axis	y_1	$1,495 \pm 3\%$ m
Shortest axis	z_1	$1,347 \pm 3\%$ m
Mass	m_1	$2.353 \pm 0.1 \times 10^{12}$ kg
Density	ρ_1	1.97 ± 0.24 g/cm^3
Rotation period	T_1	2.765 ± 0.0003 hr
Secondary		
Largest axis	x_2	$571 \pm 6\%$ m
Intermediate axis	y_2	$463 \pm 6\%$ m
Shortest axis	z_2	$349 \pm 6\%$ m
Mass	m_2	$0.135 \pm 0.024 \times 10^{12}$ kg
Density	ρ_2	2.81 ± 0.63 g/cm^3
Rotation period	T_2	17.4223 hr
Mutual orbit		
Semi-major axis	a	$2,548 \pm 15$ m
Mass fraction	m	0.0543
Period	T	17.42 ± 0.036 hr

neighbourhood of the lowest-energy saddle equilibrium point of the body's amended potential field. A similar strategy can be applied for landing on a binary system [12], however, in that case we must take into account the dynamics of the system as a whole, and not merely of the single target body. If we assume both primary and secondary to orbit their mutual center of mass in circular orbits, simplify the shape of the primary to a sphere and the shape of the secondary to an ellipsoid tidally locked to the primary, we successfully reduce the complex dynamical environment to that of the well-studied Circular Restricted Three-Body Problem (CR3BP) [51]. This system can be shown to have a total of five equilibrium points where the acceleration on a third particle, when expressed in a reference frame fixed to both bodies and centered at the mutual center of mass, is zero. The locations of these points, more frequently known as Lagrange libration points [51], are visualized for the 1999 KW$_4$ system in Figure 10.1. Their locations are listed in Table 10.2, with respect to the center of mass of the system, of Alpha, and of Beta.

The CR3BP has been widely treated in literature; it can be shown that the three collinear equilibrium points L_1, L_2 and L_3 are unstable, while the equilateral L_4 and L_5 points are stable [51]. Indeed, when releasing a lander in the neighbourhood of one of the former points, it will move away from the respective equilibrium following its unstable manifold [12]. We recognize the similarity between this release and that discussed for a unitary body in Section 9.1. The characteristics of trajectories emanating from the unstable equilibrium points at a binary system were investigated by [12], where the orbit periapses were projected to verify whether impacts with the asteroid bodies indeed take place - a clear necessary condition for successful deployment. It was shown that, due to the typical shape of most binary systems, deployment to the secondary body is always possible from L_1 and very often from L_2. However, due to the structure of the CR3BP and typical size of the primary, it is generally impossible to reach the primary from L_3 and only rarely from L_1 [12]. These deployment failures are a result of the size and rotation rate of most primaries, as their equators rotate at near-orbital velocities. Indeed, using the values of Table 10.1 we compute the 'circular' orbital velocity at the equator as $V_c = \sqrt{\mu/R} = 0.464$ m/s, while at that location the surface rotates at a velocity of $V_s = \omega R = 0.460$ m/s. We will test deployment from all three collinear Lagrange points for the 1999 KW_4 system using our simulation software and verify the above statements about deployment success and failure.

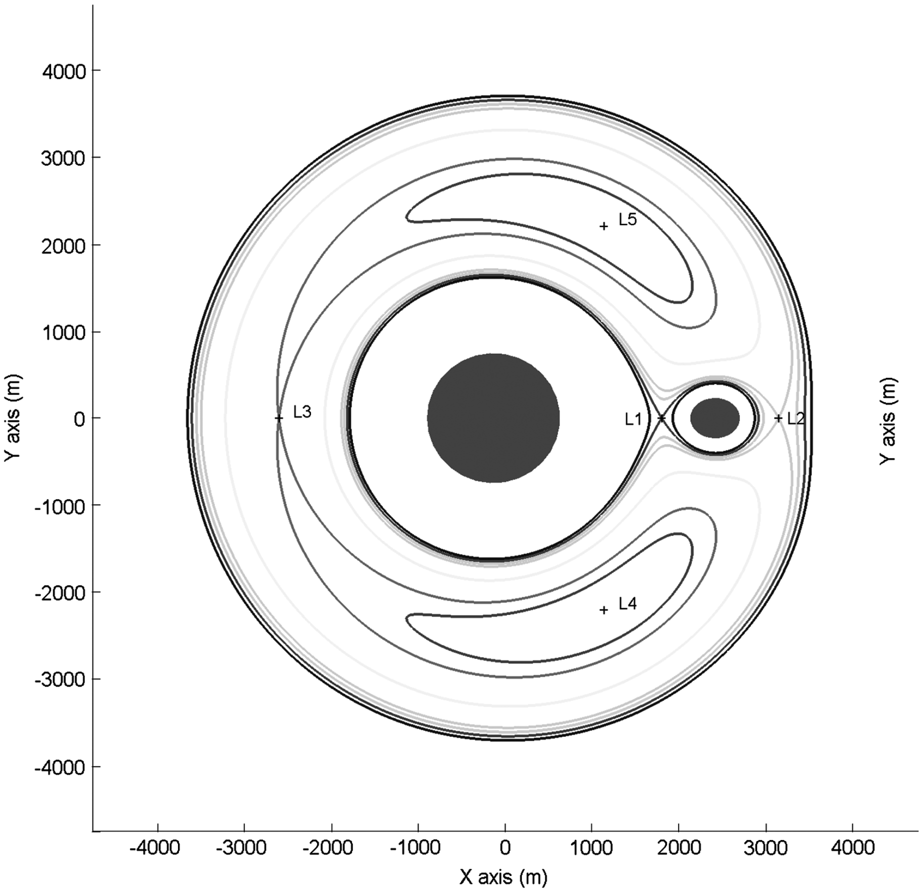

Figure 10.1: Zero-velocity curves and equilibrium points of the 1999 KW_4 system [12].

Table 10.2: Equilibrium point locations of the 1999 KW_4 system [15].

	x_{com} [m]	y [m]	Stable?	x_α [m]	x_β [m]
L_1	1,777	0	No	1,915	-633
L_2	3,140	0	No	3,278	730
L_3	-2,594	0	No	-2,456	-5,004
L_4	1,132	-2,195	Yes	1,270	-1,278
L_5	1,132	2,195	Yes	1,270	-1,278

10.2 Deployment to Beta

During our discussion of deployment to unitary systems, we have investigated the effects of the stochastic rock model and of variations of the interaction parameters on the resulting lander trajectories. We therefore refrain from repeating this in our simulations of binary systems, and instead focus solely on the effects of varying the lander release conditions. We stress that all interaction parameters and mission hardware are kept at their nominal values throughout all subsequent simulations; the reader is again referred to Table 9.1 for an overview of the particular values. We now focus first on deployment to *Beta*, the secondary of 1999 KW_4, as we expect this to be more successful than deployment to the primary.

10.2.1 Deployment from L_1

We have produced batches of 100 simulations for a number of release positions. The nominal deployment is initiated from the L_1 equilibrium point, for all other batches we have shifted the release position either towards or away from the asteroid surface. The exact coordinates of these points, as well as their respective distance from the asteroid surface, are included in Table 10.3. These points are also visualized in Figure 10.3.

The typical results for the nominal deployment case are shown in Figures 10.2a through 10.2d. We can see that, nominally, deployment to Beta from L_1 is always successful. When moving the release position closer to Beta's surface, we see the expected decrease in time-to-full-stop while all simulations are again successful. Furthermore, when moving the release point away from the surface 25 m, deployment is still successful. However, when moving beyond this position, deployments start to fail. The result here is the same as that for unitary systems; the release position should not be moved farther than 5% from the equilibrium point in the direction away from the surface. We also again observe that mission designers are offered a clear trade-off between the time-to-full-stop and the distance to which the mothership has to approach the asteroid surface to release the lander. We confirm the statement made previously that deployment from the L_1 equilibrium point to Beta is indeed possible. However, we must make an important remark: the L_1 point is located *between* the primary and the secondary.

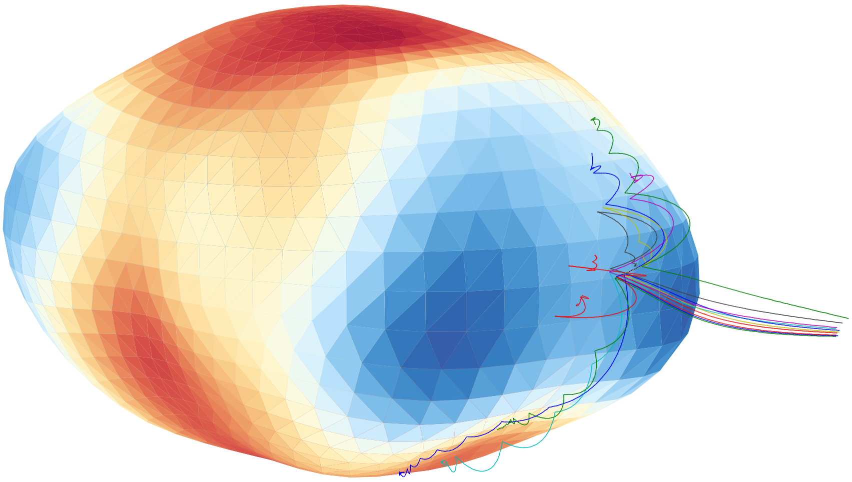

(a) Overview of 10 trajectories.

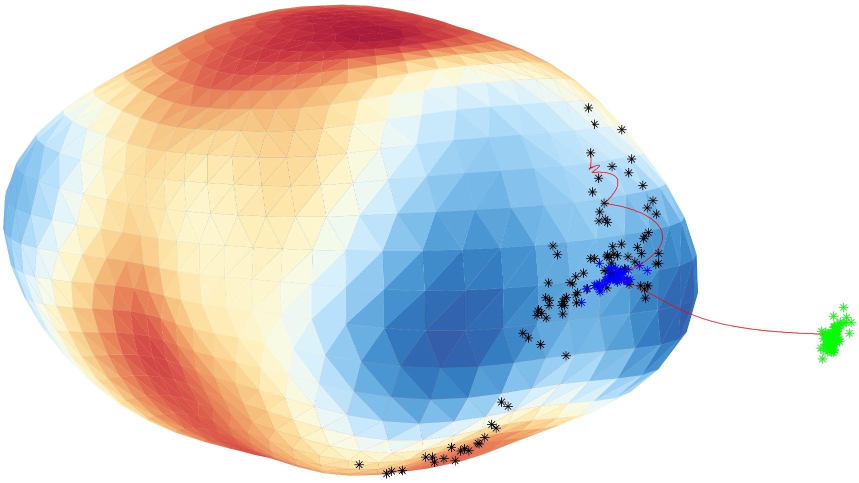

(b) Initial, first impact and final stop locations.

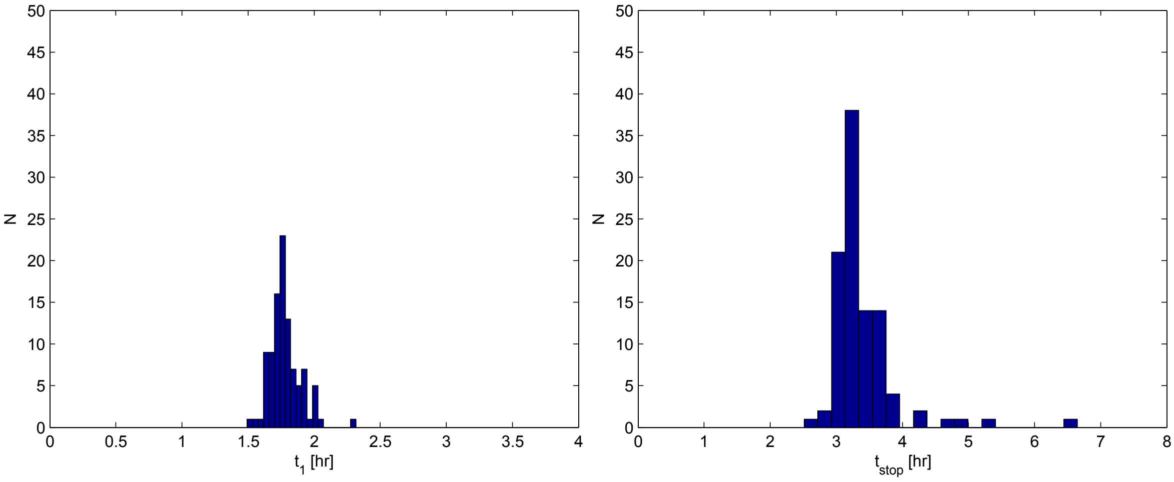

(c) Time to first impact. **(d)** Time to full stop.

Figure 10.2: Results for nominal deployment to 1999 KW_4 Beta from L_1.

This makes it naturally unattractive, from a safety point of view, as the mothership has to make the relatively dangerous manoeuvre of entering between the two bodies.

Table 10.3: Statistics of release position variation at 1999 KW$_4$, deployment from L$_1$.

	Away from surface			Nominal	Towards surface		
x [m]	-705	-680	-655	-630	-605	-580	-555
y [m]	0	0	0	0	0	0	0
z [m]	0	0	0	0	0	0	0
d [m]	470	445	420	395	370	345	320
Success [%]	0	85	100	100	100	100	100
$\mu_{t_{stop}}$ [hr]	16.15	5.32	3.91	3.39	3.07	2.97	2.66
$\sigma_{t_{stop}}$ [hr]	3.74	2.19	0.55	0.52	0.46	0.43	0.50
$\frac{\lvert\mu-\mu_{nom}\rvert}{\sigma_{nom}}$ [%]	+2,461.77	+372.40	+100.85		-63.00	-82.35	-140.79
$\frac{\lvert\mu-\mu_{nom}\rvert}{\mu}$ [%]	+376.06	+56.89	+15.41		-9.62	-12.58	-21.51

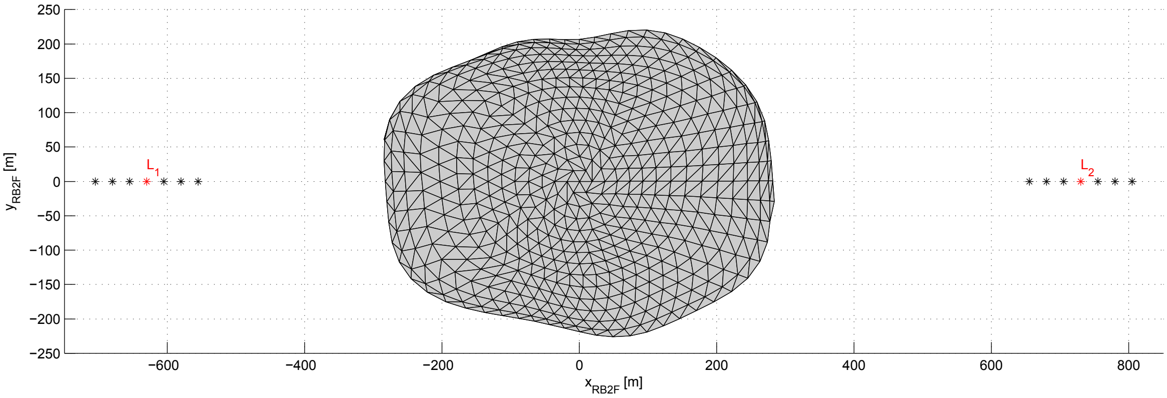

Figure 10.3: Release points tested for deployment to 1999 KW$_4$ Beta.

10.2.2 Deployment from L$_2$

Deployment to Beta from L$_2$ is investigated in the same way, where we use the parameters listed in Table 9.1 and produce batches of 100 simulations where we vary the release position. The tested points are listed in Table 10.4, and also shown visually in Figure 10.3. The results for nominal deployment are included in Figures 10.4a through 10.4d.

We observe that deployment from L$_2$ are highly similar to deployment from L$_1$. Nominal deployment is entirely successful, as is release from any point closer to the surface of Beta. A clear relationship between the distance from the surface and the mean time-to-full-stop is again present. We remark that nominal deployment from L$_2$ takes about 45 minutes longer

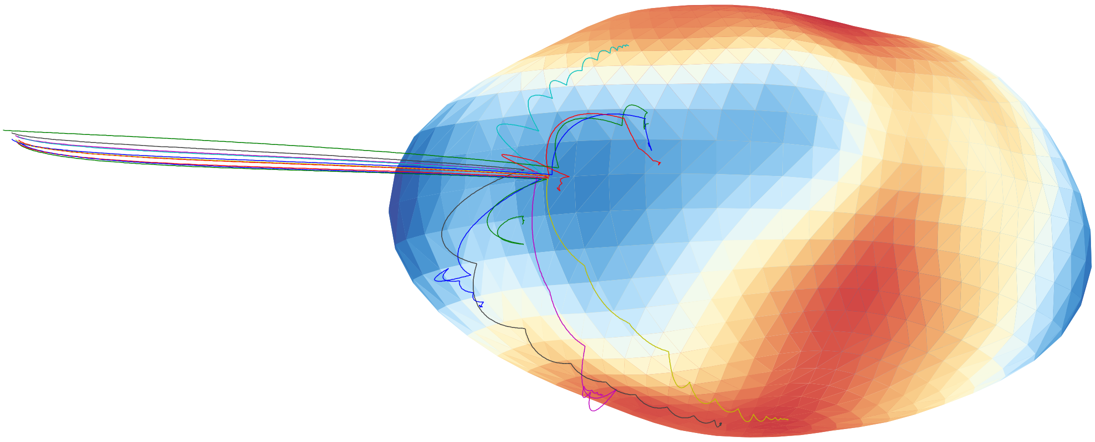

(a) Overview of 10 trajectories.

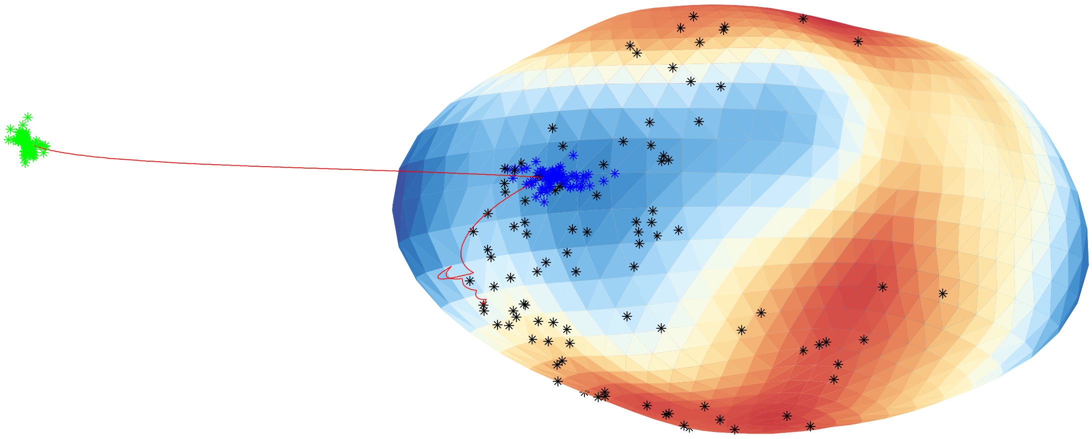

(b) Initial, first impact and final stop locations.

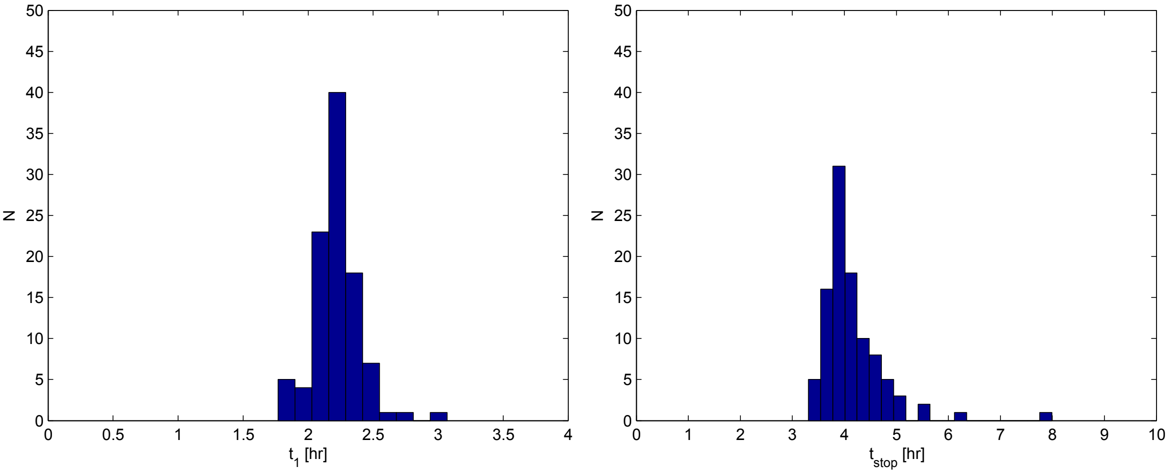

(c) Time to first impact. **(d)** Time to full stop.

Figure 10.4: Results for nominal deployment to 1999 KW$_4$ Beta from L$_2$.

than deployment from L_1, but is still well within acceptable bounds from a power perspective. We do note that, when deploying from L_2, it is possible to move farther away from the asteroid surface and still have successful deployments, compared to deployment from L_1. This fact, combined with the knowledge that L_2 lies outside of the binary system, makes the latter far more attractive for lander deployments than L_1, despite the fact that deployment takes slightly longer. We conclude that deployment to Beta is indeed possible from both L_1 and L_2, though because of mothership safety considerations it is more attractive to deploy from L_2.

Table 10.4: Statistics of release position variation at 1999 KW_4, deployment from L_2.

	Away from surface				Nominal	Towards surface		
x [m]	830	805	780	755	730	705	680	655
y [m]	0	0	0	0	0	0	0	0
z [m]	0	0	0	0	0	0	0	0
d [m]	550	525	500	475	450	425	400	375
Success [%]	82	98	100	100	100	100	100	100
$\mu_{t_{stop}}$ [hr]	7.07	5.71	5.08	4.52	4.15	3.80	3.57	3.46
$\sigma_{t_{stop}}$ [hr]	1.35	0.78	0.68	0.59	0.61	0.55	0.57	0.45
$\frac{\lvert\mu-\mu_{nom}\rvert}{\sigma_{nom}}$ [%]	+216.53	+201.43	+137.07	+61.82		-64.64	-101.79	-153.67
$\frac{\lvert\mu-\mu_{nom}\rvert}{\mu}$ [%]	+41.31	+27.34	+18.36	+8.06		-9.35	-16.39	-19.81

10.3 Deployment to Alpha

Finally, we investigate the deployment of landers to *Alpha*, the primary body of the 1999 KW_4 binary asteroid system. We apply once more the nominal release parameters shown in Table 9.1 and first investigate deployment to Alpha from L_3.

Deployment from L_3

After initiating simulations with landers beings released using nominal conditions from L_3, it immediately became clear that this deployment is problematic. For reference, we show a single trajectory as an example in Figure 10.5. We can see that the lander continues to orbit the asteroid, and does not even closely approach the surface. This is consistent with the analysis of [12], who predicted that ballistic landing on Alpha from either equilibrium points as impossible. Indeed, we see that the unstable manifold departing from L_3 is very weak and fails to deliver the lander to the asteroid surface. It is clear that deployment along the manifold is not possible for deployment to Alpha from L_3. As an alternative strategy, we perform simulations where the lander is still released from the L_3 equilibrium point, but instead with a much higher release velocity. In this case, the lander will no longer follow the unstable manifold, which is a solution of the linearized system, and only manifests itself when the initial velocity at the equilibrium point is low, but instead fly a more 'direct' ballistic arc.

A resulting trajectory is shown in Figure 10.6, where an initial velocity of $V_{rel} = 10$ m/s was used. As can be seen from this figure, this trajectory does indeed reach the surface of Alpha. However, the velocity of the lander is still very high after impacting the surface, it therefore fails to remain bound to the surface and instead escapes the asteroid. We argue that the magnitude of this rebound velocity is a result of the coefficient of restitution e, and that lowering its magnitude might result in successful capture. After testing a number of initial conditions, it was found that a release velocity of at least ~ 5 m/s for the lander to reach the surface, which in turn requires a coefficient of restitution as low as $e = 0.1$ to ensure capture. Recalling the discussion made in Section 9.1 about feasible values of e, we realize that $e = 0.1$ is unrealistic. Indeed, any value lower than $e \sim 0.4$ is highly unlikely.

We conclude that ballistic delivery of a passive device from L_3 to Alpha is not possible. However, is is possible to release a lander with propulsive capabilities on a fast, ballistic trajectory from the equilibrium point to deliver it to the surface. The lander may then fire its thrusters or use some form of attachment device[1] to kill its remaining velocity.

Deployment from L_1

Finally, when investigating deployment to Alpha from L_1, we see the same results as for deployment from L_3; the unstable manifold proves to be too weak to deliver the landers to the surface when released with nominal conditions. Ballistic deployment to Alpha is impossible from either equilibrium point; this is consistent with the analysis made in [12].

---

[1] For example, consider the harpoons which Rosetta's Philae lander will use at comet 67P/CG, as discussed in Section 2.1.

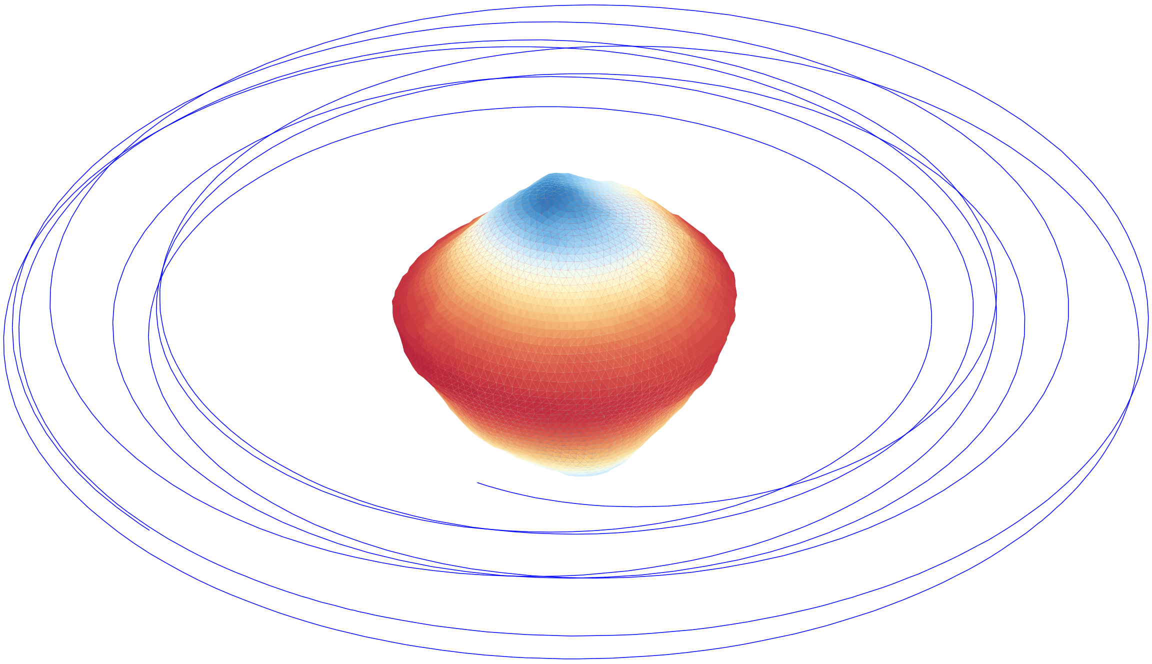

Figure 10.5: Example of failed deployment to 1999 KW_4 Alpha after release from L_3.

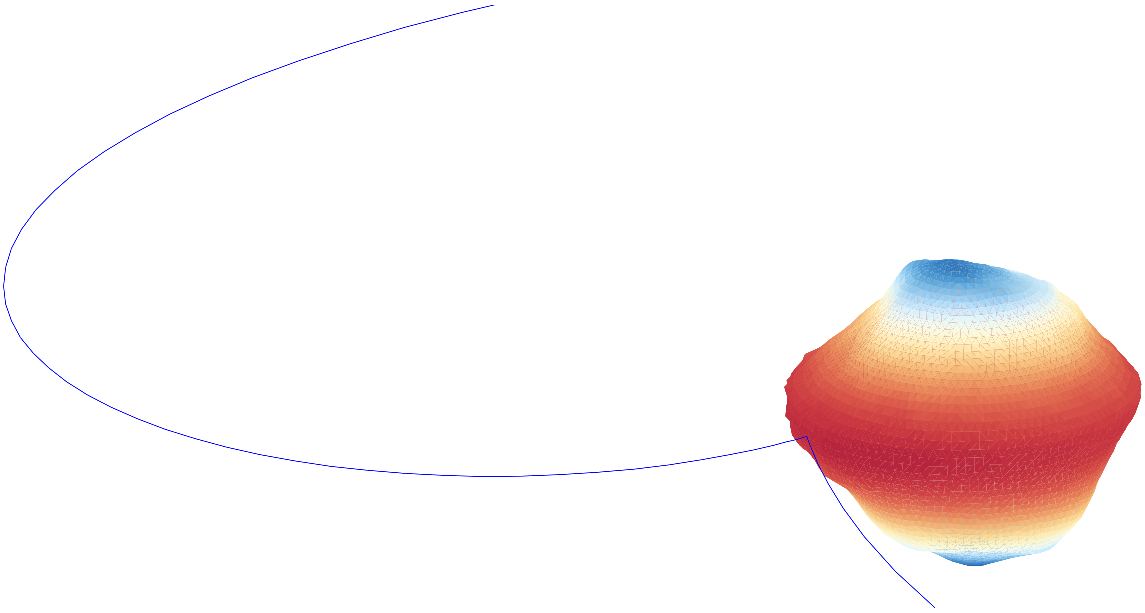

Figure 10.6: Example of failed deployment to 1999 KW_4 Alpha after 'fast' release from L_3.

Part V

Conclusions and Recommendations

Chapter 11

Conclusions

We have investigated the ballistic deployment of passive, spherical landers to unitary and binary asteroids as a means of establishing scientific instruments on the surfaces of these bodies. A software package was developed to numerically simulate the motion of such landers in the asteroid environment. The complex gravity fields of the irregular asteroid bodies were modelled using constant-density polyhedra, which represents the shape of an asteroid with triangular facets. Additionally, surface interactions between landers and the asteroid surface were implemented through an inclusion of the normal, Coulomb friction and rolling resistance forces and torques. The presence of rocks on the surface was accounted for using a stochastic model which mimics the topography observed on asteroid Itokawa by the Hayabusa spacecraft. This rock model affects lander motion both during impacts with the surface, and during contact motion on the surface. By including all of the above elements, our software captures all interactions present between a lander and an arbitrary asteroid body. Extensive verification and validation was performed to ensure the correct workings of all software modules. A large number of trajectories for both unitary and binary systems were simulated, and we have subsequently investigated the sensitivity of deployment to a number of relevant mission parameters. In these simulations, we have used lander hardware from the proposed BASiX mission, for which a prototype passive spherical lander has already been designed.

The deployment of landers to a unitary system was investigated using asteroid *25143 Itokawa* as target body. A nominal deployment scenario was constructed from literature, in which landers are released from their mothership in the neighborhood of the lowest-energy saddle equilibrium point of an asteroid's amended potential field. At Itokawa, this point is located roughly 230 meters above the surface. Following a low-velocity release from such a point, a lander will follow the unstable manifold emanating from the equilibrium and reach the asteroid surface. Through the simulation of a large number of trajectories, this strategy was proven to be successful in delivering landers to Itokawa's surface, where the mean time-to-full-stop was roughly 5.5 hrs with a standard deviation of 1.2 hrs. The dispersion of landers across the surface is very wide and mostly unpredictable, though they are generally seen to settle in zones of low amended geopotential. An investigation of the effects of rocks on Itokawa's surface revealed that their inclusion is important during impacts with the asteroid model, but may be ignored without loss of accuracy during contact motion. Additional simulations revealed the influence of the three parameters which govern the interactions between a lander and the asteroid surface. It was shown that the coefficient of restitution e is by far the most governing of all three, and strongly affects both the lander dispersion and time-to-full-stop. Secondly, varying the coefficient of friction f has no discernible effect on lander motion. Finally, the coefficient of rolling resistance C_{rr} plays a role in determining the time-to-full-stop, though its effect is only a third of that of the coefficient of restitution.

Additionally, we have performed simulations to investigate the effects of the release position, velocity, and their respective uncertainties. It was shown that landers should be released no further than 5% away from the equilibrium point, in the direction away from the asteroid surface, to guarantee successful deployment. In this one must take into account the uncertainty on the position, as well as errors in the modelled gravity field. When moving the release position closer to the asteroid surface, the relative decrease in time-to-full-stop is about equal to the relative decrease in distance to the asteroid. Furthermore, it was shown that the release velocity and associated uncertainty should be such that the initial velocity of the lander is guaranteed to be directed towards the asteroid surface. The time-to-full-stop was seen to decrease with an increasing release velocity, though we considered only values lower than the local circular orbital velocity.

For *binary* systems, we have investigated deployment to the 1999 KW_4 system. The system's rotating reference frame has a total of five equilibrium points, of which the three collinear points are unstable and provide excellent positions for the ballistic release of landers. Deployment to Beta, the system's secondary body, was shown to be feasible from both the L_1 and L_2 equilibria, with deployment again fully successful up to a relative distance of 5% behind the equilibria. The mean time-to-full-stop was obtained as 3.40 hrs for deployment from L_1 and 4.15 hrs for deployment from L_2. However, due to the L_1 equilibrium being located between the primary and secondary, this point is less attractive for release as it requires the mothership to perform the relatively dangerous manoeuvre of moving between the two asteroid bodies. In contrast, ballistic deployment to Alpha was shown to be impossible from both L_1 and L_3. The unstable manifolds emanating from these equilibria proved to be too weak to deliver landers to the surface. While the landers can be released with a higher velocity to ensure impact with the surface, they then fail to remain bound to the asteroid body after the first rebound. The near-orbital velocity at which Alpha's surface rotates prevents successful deployment.

It is concluded that passive, spherical landers provide a low-risk, low-cost way of deploying scientific instruments to the surface of an asteroid, following ballistic release from the neighborhood of the lowest-energy saddle equilibrium point of an asteroid's dynamical system. This strategy poses little to no risk to the mothership spacecraft and allows mission designers to trade off the lander release altitude with the time it takes the landers to come to a full stop. Missions which require successful asteroid lander deployment, such as for example BASiX, are thus proven to be fully feasible.

Chapter 12

Recommendations for Future Work

HAVING CONCLUDED THE results of this thesis, we finally state a number of recommendations for future work regarding our research, as listed below. These points will be treated by the author during a PhD following the completion of the current work.

- As discussed in Section 7.3, we have sacrificed some accuracy during gravity field in favour of computation speed by using simplified, 320-facet polyhedra to model asteroid gravity fields. Although this works well for our purposes, the inherent error reaches a maximum of about 7%, which is considerably higher than the magnitudes we have accepted in other modelling sections. The overall accuracy of simulations can be increased by sufficiently reducing this gravity modelling error. One possible solution is to pre-compute the gravity field,if this proves to be feasible from a memory-allocation perspective. Otherwise, a reduction in computation time elsewhere might justify switching to a higher-resolution gravity field.
- The rocks and boulders on asteroid surfaces are implemented in our work using a stochastic model, as presented in Section 4.6, due to its simplicity and computation speed. However, this model does not allow for easy variations in the density and sizes of rocks encountered, and is restricted to observations made at asteroid Itokawa. Furthermore, two separate simulations will encounter rocks in different locations, and it is not possible for a lander to impact the same rock twice during a simulation. By replacing the stochastic model with one that populates the polyhedron model with rocks and stores them in memory, we remove these limitations. It will then be possible to compare the stochastic model with the 'full' model; if both models produce the same results it may be desirable to continue using the stochastic model due to its computation speed.
- The current software models landers as spheres. Although directly applicable to the BASiX mission, many others envisage non-spherically shaped landers. By modifying the software to handle arbitrary lander shapes, we will be able to investigate deployment

of such landers on asteroid bodies. One obvious way of modelling these lander shapes would be to also use polyhedra.

- The interaction parameters e, f and C_{rr} are currently constant across the entire asteroid surface. However, we can imagine certain local areas on an asteroid to be of slightly different composition with, for example, a lower coefficient of restitution. Such a dichotomy is clearly visible on asteroid Itokawa, which has two zones of very low grain size and without boulders. Instead of setting these parameters as constant, they should be set as a function of the location on the asteroid, possibly through a modifier that is imposed on the nominally set value.
- Our simulations have shown that the time-to-full-stop of a lander deployed to an asteroid decreases as the release velocity is increased. However, during our sensitivity analysis we have restricted ourselves to velocities below the local circular orbital velocity. It may be worthwhile to investigate high-energy deployments where landers are released with much higher velocities, as this could lead to shorter deployment times.

Bibliography

[1] di Martino, M. *The Asteroid Hazard: Evaluating and avoiding the threat of asteroid impacts.* European Space Agency, 2009.

[2] de Pater, I. and Lissauer, J. *Planetary Sciences.* Cambridge University Press, 2010.

[3] Jet Propulsion Laboratory. DAWN Mission Website. Last accessed February 25, 2014. Available at http://dawn.jpl.nasa.gov/mission/.

[4] Veverka, J., Farquhar, B., Robinson, M., et Al. The landing of the NEAR-Shoemaker spacecraft on asteroid 433 Eros. *Nature*, 413:390–393, 2001.

[5] Yano, H., Miyamoto, H., Okada, T., Scheeres, D.J. Touchdown of the Hayabusa Spacecraft at the Muses Sea on Itokawa. *Science*, 312:1350–1353, 2006.

[6] Anderson, R.C., Scheeres, D., and Chesley, S. Binary asteroid in-situ explorer (basix): A mission concept to explore a binary near earth asteroid system. In *45th Lunar and Planetary Science Conference*, 2014.

[7] National Aerospace & Space Administration. NASA Strategic Knowledge Gaps Website. Last accessed February 25, 2014, 11 2012. Available at http://www.nasa.gov/exploration/library/skg.html.

[8] Ostro, S. and Sagan, C. Cosmic collisions and the longevity of non-spacefaring galactic civilizations. 1998.

[9] Lauretta, D.S. and The OSIRIS-REx Team. An overview of the OSIRIS-REx asteroid sample return mission. In *43rd Lunar and Planetary Science Conference*, 2012.

[10] Kawaguchi, J., Fujiwara, A., Uesugi, T. Hayabusa: Its technology and science accomplishment summary and Hayabusa-2. *Acta Astronautica*, 62:639–647, 2008.

[11] Jet Propulsion Laboratory. JPL Solar System Dynamics Website. Last accessed February 25, 2014. Available at http://ssd.jpl.nasa.gov/.

[12] Tardivel, S. and Scheeres, D.J. Ballistic Deployment of Science Packages on Binary Asteroids. *Journal of Guidance, Control and Dynamics*, 36:700–709, 2013.

[13] Tardivel, S., Michel, P., Scheeres, D.J. Deployment of a lander on the binary asteroid (175706) 1196 FG3, oitebtuak target of the european MarcoPolo-R sample return mission. *Acta Astro*, 89:60–70, 2013.

[14] Tardivel, S., Scheeres, D.J., Michel. High altitude deployment of landers to asteroid surfaces using natural manifolds. In *24th Space Flight Mechanics Meeting*, 2014.

[15] Bellerose, J.E. *The restricted full three body problem: Applications to binary asteroid exploration*. PhD thesis, University of Michigan, 2008. Available at http://tinyurl.com/kso3ydj (redirects).

[16] Tardivel, S. *The Deployment of Scientific Packages to Asteroid Surfaces*. PhD thesis, University of Colorado, 2014.

[17] National Aerospace & Space Administration. Near Earth Rendevous Mission Website. Last accessed February 25, 2014. Available at http://near.jhuapl.edu/.

[18] Miller, J.K., Konopliv, A.S., Antreasian, P.G., et Al. Determination of Shape, Gravity and Rotational State of Asteroid 433 Eros. *Icarus*, 155:3–17, 2002.

[19] Thomas, P.C., Veverka, J., Robinson, M.S., et Al. Shoemaker crater as the source of most ejecta blocks on the asteroid 433 Eros. *Nature*, 413:394–396, 2001.

[20] Fujiwara, A., Kawaguchi, J., Yeomans, D., et Al. The Rubble-Pile Asteroid Itokawa as Observed by Hayabusa. *Science*, 312:1330–1334, 2006.

[21] Yoshimitsu, T., Kawaguchi, J., Hashimoto, P., et Al. Hayabusa-final autonomous descent and landing based on target marker tracking. *Acta Astronautica*, 65:657–665, 2009.

[22] Hashimoto, T., Kubota, T., Sawai, et Al. Final Autonomous Descent Based on Target Marker Tracking. In *AIAA/AAS Astrodynamics Specialist Conference and Exhibit*, 2006.

[23] Sawai, S., Kawaguchi, J., Scheeres, D.J., et Al. Development of a Target Marker for Landing on Asteroids. *Journal of Spacecraft and Rockets*, 38:601–608, 2001.

[24] N. Murdoch, P. Abell, and et Al. Carnelli, I. Asteroid Impact and Deflection Assessment (AIDA) Mission. Technical report, European Space Agency, 2012.

[25] Bauer, M. Rosetta arrives at comet destination. Last accessed August 6, 2014, August 2014. Available at http://tinyurl.com/q3wsth3 (redirects).

[26] Biele, J. and Ulamec, S. Capabilities of Philae, the Rosetta Lander. *Space Science Review*, 138:275–289, 2008.

[27] European Space Agency. Esa science & technology: Rosetta. Last accessed October 26, 2014, 10 2014. Available at http://sci.esa.int/rosetta/.

[28] Tsuda, Y., Yoshikawa, M., Abe, M., et Al. System design of the Hayabusa 2 Asteroid sample return mission to 1999 JU3. *Acta Astronautica*, 91:356–362, 2013.

[29] Lange, C., Dietze, C., Ho, T.M., et Al. Baseline design of a mobile asteroid surface scout (MASCOT) for the Hayabusa-2 Mission. In *61st International Astronautical Congress*, 2010.

[30] Yoshimitsu, T., Kubota, T., Nakatani, I., et Al. Hopping rover "Minerva" for asteroid exploration. In *5th International Symposium on Artificial Intelligence, Robotics and Automation in Space*, 1999.

[31] Berry, K., Sutter, B., May, A., et Al. OSIRIS-REx Touch-and-Go (TAG) Mission Design and Analysis. In *36th Annual AAS Guidance and Control Conference*, 2013.

[32] Galvez, A. Asteroid impact & deflection assessment (aida) study. Last accessed July 5, 2014, December 2012. Available at http://tinyurl.com/bkqmeaw (redirects).

[33] Roark, S. and Cottingham, C. and Dissly, R., et Al. Explosive Surface Pods for Cratering Experiments on Small Bodies. In *41st Lunar and Planetary Sciecne Conference*, 2010.

[34] Tardivel, S. and Scheeres, D.J. and Michel, P., Van wal, S., et Al. Contact Motion on Surface of Asteroid. *Journal of Spacecraft and Rockets*, pages 1–15, 2014.

[35] Scheeres, D.J. *Orbital motion in strongly perturbed environments.* Springer, 2011.

[36] O'Rourke, J. *Computational Geometry in C.* Cambridge University Press, 1997.

[37] Schwartz, S.R., Richardson, D.C., Mich, P. An implementation of the soft-sphere discrete element method in a high-performance parallel gravity tree code. *Granular Matter*, 14:363–380, 2012.

[38] Richardson, D.C. and Walsh, K.J. and Murdoch, N., et Al. Numerical simulations of granular dynamics: I. Hard-sphere discrete element method and tests. *Icarus*, 212:427–437, 2010.

[39] Michikami, T., Nakamura, A.M., Hirata, N. Size-frequency statistics of boulders on global surfaces of asteroid 25143 Itokawa. *Earth Planets Space*, 60:13–20, 2008.

[40] Geitz, B. Vector Geometry for Computer Graphics. Last accessed July 5, 2014, 2007. Available at http://tinyurl.com/ptpb7tk (redirects).

[41] Montenbruck, O. and Gill, E. *Satellite Orbits: Models, Methods and Applications.* Springer, 2001.

[42] MathWorks. Solve nonstiff differential equations; medium order method. Last accessed March 8, 2014. Available at http://tinyurl.com/prwf87a (redirects).

[43] Dormand, J.R. and Prince, P.J. A family of embedded Runge-Kutta formulae. *Journal of Computational and Applied Mathematics*, 6:19–26, 1980.

[44] Scheeres, D.J. and Gaskell, R. and Abe, S., et Al. The Actual Dynamical Environment About Itokawa. *AIAA*, 6661:1–22, 2006.

[45] Small Bodies Data Ferret. Last accessed February 28, 2014. Available at http://sbn.psi.edu/ferret/.

[46] Japanese Aerospace Exploration Agency. Hayabusa project science data archive. Last accessed July 18, 2014, July 2014. Available at http://www.isas.jaxa.jp/e/enterp/missions/hayabusa/.

[47] Colwell, J.E. Low velocity impacts into dust: results from the collide-2 microgrvity experiment. *Icarus*, 164:188–196, 2003.

[48] Durda, D.D., Chapman,C.R., Merline, W.J., Enke, B.L. Detecting crater ejecta-blanket boundaries and constraining source crater regions for boulder tracks and elongated secondary craters on Eros. *Meteoritics & Planetary Science*, 47:1087–1097, 2012.

[49] Van wal, S., Tardivel, S., Sanchez, P., et Al. Rolling Resistance of a Spherical Pod on a Granular Bed. Submitted for publication to Physical Review Letters.

[50] Ostro, S. and Margot, J. and Benner, L., et Al. Radar Imaging of Binary Near-Earth Asteroid (66391) 1999 KW4. *Science*, 314:1276–1280, 2006.

[51] Wakker, K.F. *Astrodynamics I Course Reader*. Delft University of Technology, 2010.